Dissertation
submitted to the
Combined Faculty of Mathematics, Engineering and Natural Sciences
of Heidelberg University, Germany
for the degree of
Doctor of Natural Sciences

Put forward by
M.Sc. Jennifer Josephine Hardt
Born in: Böblingen (Germany)
Oral examination: July 23rd 2025

Range Guided Carbon Ion Therapy Using Mixed Carbon-Helium Beams – Dose Calculation and Treatment Planning

Referees: Prof. Dr. Joao Seco
Prof. Dr. Christian Karger

Zusammenfassung

Gemischte Kohlenstoff-Helium-Strahlen wurden vor kurzem für die Reichweitenverifikation in der Kohlenstoffionentherapie vorgeschlagen. Helium- und Kohlenstoffionen besitzen ein annähernd gleiches Masse-zu-Ladung-Verhältnis und können daher gemeinsam auf dieselbe Geschwindigkeit (Energie pro Nukleon) beschleunigt werden. In dieser Methode, wird eine geringe Anzahl Heliumionen dem therapeutischen Kohlenstoffstrahl hinzugefügt, wodurch eine gleichzeitige Behandlung mit Kohlenstoffionen und Bildgebung mit Heliumionen ermöglicht wird, da Heliumionen eine dreifache Reichweite im Vergleich zu Kohlenstoffionen besitzen und somit distal aus dem Patienten austreten können.

Diese Arbeit untersucht die Implikationen für die Therapieplanung, wenn solche Helium-Radiografien verfügbar wären. Zu diesem Zweck wurde ein Software-Framework zur Dosisberechnung und -optimierung von gemischten Kohlenstoff-Helium Bestrahlungsplänen sowie Simulation der entsprechenden Helium-Radiografien entwickelt. Dafür wurde das Open-Source-Therapieplanung-Toolkit matRad erweitert. Das Software-Framework wurde auf Patienten im Bauch- und Lungenbereich angewendet, um die Heliumreichweite zu untersuchen. In den meisten untersuchten Patientenfällen wies mindestens eine Energie des Bestrahlungsplanes eine unzureichende Heliumreichweite auf. Um eine ausreichende Heliumreichweite sicherzustellen, die zudem innerhalb des empfindlichen Bereichs des Detektionssystems liegt, wurden verschiedene Planungsstrategien untersucht und in das Therapieplanungs-Framework integriert. Alle untersuchten Planungsstrategien stellten erfolgreich eine ausreichend hohe Heliumreichweite sicher, während gleichzeitig eine niedrige Heliumdosis und eine zufriedenstellende gemischte Kohlenstoff-Helium-Dosis beibehalten wurde. Der Einsatz von Reichweitenmodulatoren erhöhte zudem die Anzahl der detektierbaren Helium-Spots. Potenzielle Anwendungsfälle der gemischten Kohlenstoff-Helium strahlen wurden durch die Verifikation der Patientenposition während der Behandlung eines Prostatapatienten sowie der Atemphase eines Lungenpatienten untersucht.

Gemischte Kohlenstoff-Helium Strahlen zeigen großes Potenzial für die Echtzeitüberwachung der Behandlung und ermöglicht eine Visualisierung der Anatomie des behandelten Patienten. Das entwickelte Framework unterstützt weitere experimentelle Validierungen und eine klinische Implementierung und stellt somit einen vielversprechenden Fortschritt für die reichweitengestützte Strahlentherapie dar.

Summary

Mixed carbon-helium beams have recently been proposed for range verification in carbon ion therapy. Helium and carbon ions have approximately the same mass-to-charge ratio, and thus they can be accelerated together to the same velocity (energy per nucleon). In this method, a small helium fluence is added to the therapeutic carbon beam, enabling simultaneous carbon treatment and helium imaging as the helium ions have three times the range of the carbon ions and thus can exit the patient distally.

This thesis investigates the implications for treatment planning if such online helium radiographs were available. For this purpose, a software framework for dose calculation and optimization of mixed beam treatment plans along with simulation of the corresponding helium radiographs was developed. Therefore, the open-source treatment planning toolkit matRad was extended. The framework was applied to abdominal and lung patients, investigating the viability of the helium range. In most investigated patient cases, at least one treatment energy had insufficient helium range. To ensure adequate helium range that is also within the sensitive range of the detection system, different planning strategies were explored and incorporated in the treatment planning framework. All investigated planning strategies successfully ensured a high enough helium range while maintaining a low helium dose and a satisfactory mixed carbon-helium dose. The use of range snifters also increased the amount of detectable helium spots. Potential use cases of the mixed beam method were investigated by verifying the patient position during treatment for a prostate patient and verifying the breathing phase in a lung patient.

The mixed beam approach shows potential for real-time treatment monitoring, allowing visualization of the treated patient's anatomy. The developed framework supports further experimental validation and clinical adaptation, offering a promising advancement for range-guided radiotherapy.

Contents

Acronyms

BEV beams eye view 36, 64

CBCT cone beam computed tomography 46

CSDA continuous slowing down approximation 5

CT computed tomography . . . . . 11, 13, 18–21, 30, 35–40, 42 ff., 46, 66, 78, 83–86, II

CTV clinical target volume 19

DRR digital reconstructed radiograph . . . . . 43, 55, 64, 66, 68, 74, 80, 83, 85 f.

DVH dose volume histogram 18, 52, 61, 63, 65, 69

FEHeRad full energy helium radiograph 41, 55, 64, 66, 70, 74, 82

HeRad helium radiograph . . . . . 26, 42 f., 45, 74, 80

HIT Heidelberg ion therapy facility 9, 25, 27, 73, 79, 87

HLUT housfield look-up table 43, 55, 80

HU housfield unit . . . . . 11, 19, 26, 37, 42, 74, 80, 82 f., II

IES iso-energy slice . . . . . 9, 32, 45 f., 59 f., 68 ff., 74, 84 f.

IMPT intensity modulated particle therapy 14

LEM local effect model 29

LET linear energy transfer 7, 27, 29, 51, 79

LQ linear quadratic 29

MC monte carlo . . . . . 2, 15 f., 20, 23, 26, 35 ff., 39 f., 42, 50 f., 54 ff., 79 f.

MCS multiple coulomb scattering 6, 13, 15

MLP maximum likelihood path . . . . . 12 f., 24, 42

MRI magnetic resonance imaging 21, 82

MSE mean squared error . . . . . 43, 64 f., 83

OAR organ at risk . . . . . 13, 17 f., 81

PET positron emission tomography 20, 82

PIB plane-of-interest binning 13

PMT photo multiplier tubes 23

PTV planning target volume 19, 47, 61

RBE relative biological effectiveness . . . . . 7, 27 ff., 39, 78 f.

ROI region of interest 26

RS range shifter . . . . . 32–35, 37–40, 42, 46, 55 f., 59–63, 66, 77, 79 ff., 84

RSP relative stopping power . . . . . 5, 11, 13 f., 19, 21, 25, 42, 74, 80, 82 f., II

SEHeRad single energy helium radiograph . . . . . 41 f., 66, 68 f., 74, 82–85

SSIM structural similarity index measure 43, 64, 83

TOF time of flight . . . . . 76 f.

TOPAS tool for particle simulation . . . . . 16, 23, 27, 35–38, 42 f., 55, 75, 80, 87

VOI volume of interest . . . . . 17 f., 29, 36

WEPL water equivalent path length . . . . . 14, 31 f., 41 f., 45, 69 ff., 84

WET water equivalent thickness 11, 13, 24 ff., 32, 40, 44 ff., 49 f., 55, 63, 66, 68–71, 73, 75 ff., 82–85

Preface

Contributions: During the dissertation I contributed to other works. Mainly experimental work collecting proton and helium imaging data. Hereby I was not the primary investigator however I did contribute to both data collection and analysis. Part of the experimental data is shown in this thesis (section 4.1).

Publications: Part of this thesis was published before hand in (Hardt et al., 2024) another paper is currently under review and available as preprint on arXiv (Hardt et al., 2025). A complete list of publications and conference contributions can be found in the appendix A.5.

Artificial Intelligence Tools: Part of this thesis and it's underlying code was generated with the assistance of GitHub Copilot (GitHub, 2025) and ChatGPT (OpenAI, 2025) and edited by the author.

1 Introduction

After cardiovascular diseases, cancer was in 2023 the second leading cause of death in Germany, accounting for 22 % of the deaths (Destatis, 2024). Radiation Therapy utilizes ionizing radiation to destroy cancerous cells. Although conventionally photons are used for radiation therapy, particle therapy is gaining traction. The Particle Therapy Co-Operative group (PTCOG) reports that until 2022 more than 300 000 patients world wide have received proton therapy, around 50 000 carbon ion therapy and a hand full of patients helium ion therapy (PTCOG, 2025b).

The dose in photon therapy decreases exponentially after an initial buildup. Particle therapy however has a characteristically peaked dose distribution. As particles pass through matter they loose energy and slow down, this energy loss increases with decreasing velocity of the particle. Therefore particles exhibit a high dose peak at the end of their range – the Bragg peak (Jäkel, 2020). By varying the initial energy the range in the patient changes allowing for precise irradiation of the tumor. However, the highly localized dose deposition at the Bragg-peak causes particle therapy to be sensitive to uncertainties in the particle's range which can cause under dosage of the tumor or overdoseage of healthy tissue (Paganetti, 2012).

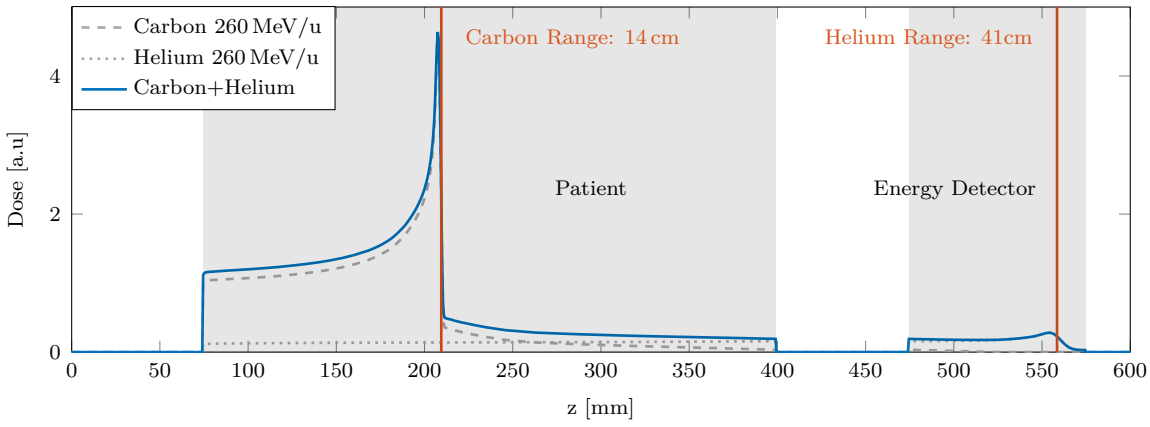

Figure 1.1.: Schematic set up of a mixed carbon-helium beam irradiation, using the same carbon and helium fluence. While the carbon ions stop in the patient and are used to irradiate the tumor, helium ions with approximately three times the range can exit the patient distally so that their residual energy can be measured by a detector, serving as an online range probe for the carbon beam.

Recently a new method for range verification was proposed using mixed carbon-helium beams (Graeff et al., 2018; Mazzucconi et al., 2018). This method utilizes the approximately same mass to charge ratio of fully ionized carbon ($^{12}C^{6+}$) and helium ($^{4}He^{2+}$) ions to accelerate them together in a synchrotron to the same velocity (same energy per nucleon). Here, helium ions have approximately three times the range of carbon ions, as seen in fig. 1.1. By adding a small fraction of helium ions to the primary carbon beam, the helium ions can now be used as an online range probe for carbon ion therapy. With an appropriate detector this could allow for simultaneous treatment with carbon ions and real-time imaging with helium ions.

Initial experimental investigations (Mazzucconi et al., 2018; Volz et al., 2020) suggest a carbon to helium ratio of 10/1, allowing for the detection of the helium ions over the carbon fragment background while still delivering a low helium dose. These studies were carried out with sequential irradiation of carbon and protons using a plastic scinitlator with a CCD camera and carbon and helium using a range telescope made out of thin plastic scintillation sheets (Kellerer et al., 2020). The first production of a mixed carbon-helium beam was reported by Graeff et al. (2024) on a research beamline followed by Kausel et al. (2025) on a clinical accelerator.

This thesis investigates the implications for treatment planning, if such online helium radiographs were available. To this end, a module for dose calculation and optimization of mixed beam treatment plans along with monte carlo (MC) simulations of the corresponding helium ion radiographs was developed. This module was used to investigate potential use cases of a mixed carbon-helium irradiation, outlining the desired performance and developing treatment planning strategies. Therefore, the residual helium range distal of the patient was analyzed for abdominal and lung cases. Additionally, strategies were developed to ensure a sufficient helium range in all patient cases while also allowing for the detection of more helium ions. Use cases for treatment verification were investigated, including the verification of the patient position for a prostate case and verification of the breathing motion in a lung case.

Part of the overarching project involved the adaption of a proton imaging detector for helium imaging, in which this thesis assisted.

2

Background

This chapter provides an overview of the main quantities and key concepts underlying the scientific work presented in this thesis. This includes the physical principles of ion therapy in section 2.1, followed by an overview of current methods for the acceleration of a mixed carbon–helium beams in section 2.2. Section 2.3 presents an overview of ion imaging systems, and section 2.4 describes the treatment planning workflow. Finally, section 2.5 concludes this chapter with a discussion of uncertainties in particle therapy.

2.1. Physics of Ion Therapy

Radiation therapy uses ionizing radiation to kill malignant cells by damaging the DNA of these cells leading to cellular death. Radiation dose d is quantified by the deposited energy $\mathrm{d}E$ in matter of mass $\mathrm{d}m$ as (Seltzer et al., 2011)

$$d = \frac{\mathrm{d}E}{\mathrm{d}m} = \frac{1}{\rho}\frac{\mathrm{d}E}{\mathrm{d}V}\,. \tag{2.1}$$

The mass density of the material is ρ, the respective infinitesimal volume element $\mathrm{d}V$.

In order to perform radiation therapy the delivered dose has to be calculated, therefore the characteristics of how ionizing radiation deposits energy and interacts with matter has to be known.

2.1.1. Physical Characteristics of Ion Irradiation

Energy Loss

Charged ions are an directly ionizing form of radiation. As they pass through matter they are slowed down and loose energy until they come to a halt. Contrary to photons they have a finite range in matter (Schlegel et al., 2018). Figure 2.1 shows the range in water for ions (proton, helium, carbon) used in particle therapy. The mean energy loss per unit path length in a material with density ρ is defined as the mass stopping power $(\mathcal{S}/\rho)$, which is a combination of the electronic mass stopping power $(\mathcal{S}_{el}/\rho)$, the nuclear mass stopping power $(\mathcal{S}_{nuc}/\rho)$ and the radiative mass stopping power $(\mathcal{S}_{rad}/\rho)$

$$\frac{1}{\rho}\mathcal{S} = \frac{1}{\rho}\mathcal{S}_{el} + \frac{1}{\rho}\mathcal{S}_{nuc} + \frac{1}{\rho}\mathcal{S}_{rad}\,. \tag{2.2}$$

The electronic mass stopping power describes inelastic interactions of the primary ion with atomic electrons of the target material and results in ionization or excitation of the target atom. The nuclear mass stopping power describes elastic scattering processes with the atomic nucleus of the target material. During these interactions a small recoil energy can be transfered to the target material. The radiative mass stopping power describes the loss of energy due to the emission of bremsstrahlung, which can be neglected in particle therapy (Seltzer et al., 2011; Newhauser et al., 2015). Figure 2.1 depicts the total, electronic and nuclear mass stopping power for ions used in particle therapy impinging on a homogeneous water target. As shown here, electronic interactions are the main contributor to the mass stopping power, while nuclear processes only become siginficant at low energies.

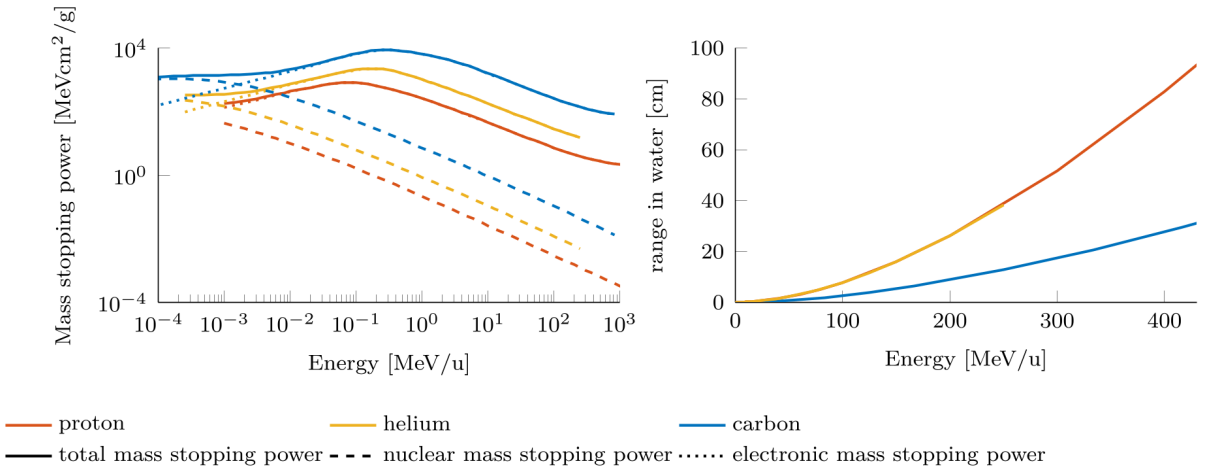

Figure 2.1.: Left: Total, electronic and nuclear mass stopping power for ions impinging on a homogeneous water target. Right: Ion range in water. Data from the ICRU report in Berger et al. (2009). The helium data only covered a energy range up to 250 MeV/u, while proton and carbon data was also available for higher energies.

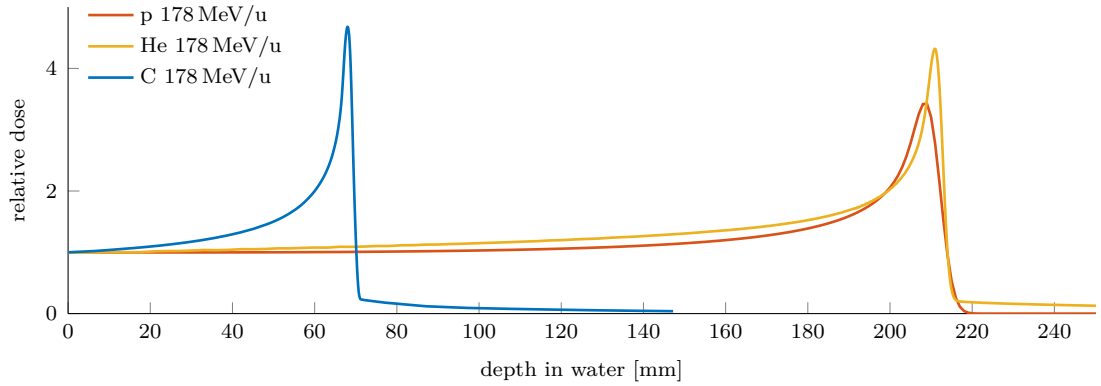

Figure 2.2.: Depth dose curves for proton, helium and carbon ions in water, with the same initial energy per nucleon, calculated using matRad (Abbani et al., 2024; Wieser et al., 2017)

The electronic stopping power, which is the expected energy loss for a particle passing through a target, can be described by the Bethe-Bloch formula (Bethe, 1930; Bloch, 1933):

$$-\left\langle \frac{\mathrm{d}E}{\mathrm{d}z} \right\rangle = \frac{4\pi n_e Z^2}{m_e c^2 \beta^2} \left(\frac{e^2}{4\pi\epsilon_0} \right)^2 \left[\ln\left(\frac{2m_e c^2 \beta^2}{I(1-\beta^2)} \right) - \beta^2 \right] . \tag{2.3}$$

Hereby the energy loss of the particle is $\mathrm{d}E$, the passed through length is $\mathrm{d}z$, the incoming particle charge is Z and the ratio of the particles velocity to the speed of light is $\beta = v/c$. Furthermore the electron mass is m_e, the vacuum permittivity is ϵ_0, the electron density of the material is n_e and the ionization potential of the target matter is I.

As seen in eq. (2.3) the loss of energy is proportional to β^{-2}, meaning that as a particle slows down it looses more and more energy until it comes to a halt, leading to a characteristic maximum in the depth dose curve of ions, the *Bragg peak*. This is depicted in fig. 2.2 for ions used in particle therapy.

Since water is often used as a reference material, the ratio of the stopping power in a material relative to that of water is defined as the relative stopping power (RSP),

$$\mathrm{RSP} = \frac{\left\langle \frac{\mathrm{d}E}{\mathrm{d}x} \right\rangle_{\text{material}}}{\left\langle \frac{\mathrm{d}E}{\mathrm{d}x} \right\rangle_{\text{water}}} . \tag{2.4}$$

Range

The distance traveled until the particle stops is the particles *range*. The particles range can be approximated with the continuous slowing down approximation (CSDA) by integrating the inverse stopping power from the initial particle kinetic energy E_0 to 0, (Schlegel et al., 2018)

$$R(E_0) = \int_{E_0}^{0} \frac{1}{-\left\langle \frac{\mathrm{d}E}{\mathrm{d}z} \right\rangle} \mathrm{d}E. \tag{2.5}$$

This approximation assumes that the particles are continuously decelerated, in spite of the stochastic nature of the interactions. Thus, not all particles with the same initial energy have the same range, this is called *range straggling*. Experimentally the range is measured as the position of the 80 % distal fall-off after the Bragg-peak. For monoenergetic protons this is the depth at which 50 % of the initial particles stop (Paganetti, 2012).

Comparing the range of an ion (R_{Ion}) to the range of a proton (R_p) one finds that the relation of the two is given by

$$\frac{R_{Ion}}{R_p} = \frac{A}{Z^2} , \tag{2.6}$$

if they have the same initial same energy per nucleon. Hereby the atomic number of the

ion is A and the charge is Z. Consequently, fully ionized helium ions ($^4He^{2+}$) have about the same range as protons and about three times the range of fully ionized carbon ions ($^{12}C^{6+}$), this can also be seen in fig. 2.2, depicting the depth dose curves for all mentioned ions, and in fig. 2.1 depicting the range.

Multiple Coulomb Scattering

While particles are traversing matter they can be elastically scattered of the nucleus, which leads to a lateral broadening of the beam. A single scattering event can be described well by Rutherford theory. However the description of multiple scattering events, also called multiple coulomb scattering (MCS) is more difficult. Molière's theory describes in first approximation the angular distribution of the scattered particles for small angles, with a gaussian function (Schlegel et al., 2018). This however is not accurate for large angle scattering. A more accurate model of MCS is the Fermi-Eyges approximation (Eyges, 1948). It describes the probability of finding a particle at a certain depth (u_i), with a certain lateral and angular displacement with the scattering moments A_n. These scattering moments can be calculated using the generalized Highland formula as described by Schulte et al. (2008),

$$A_n(u_j, u_i) = E_0^2 \left(1 + 0.038 \ln\left(\frac{u_i - u_j}{\chi_0}\right)\right)^2 \int_{u_j}^{u_i} \frac{(u_i - u)^n}{\beta^2(u)p^2(u)} \frac{\mathrm{d}u}{\chi_0} \,. \tag{2.7}$$

Hereby $E_0 = 13.6\,\mathrm{MeV}$ is a constant, β is the particle velocity with respect to the speed of light, p is the particle momentum and χ_0 is the materials radiation length, which is the mean length neede to reduce the energy of an electron by the factor $1/e$. The standard deviation of the lateral displacement is A_2, the standard deviation of the angular displacement A_0 and the correlation of lateral and angular displacement A_1.

MCS needs to be considered for both dose calculation and ion imaging, since it determines the lateral dose penumbra (Paganetti, 2012). As noted by Gehrke et al. (2018a), MCS limits the spatial resolution of ion imaging. A comparison between ion types shows that heavier ions, such as carbon and helium, offer theoretically higher spatial resolution compared to protons due to reduced scattering.

Nuclear Interaction and Fragmentation

Non-elastic nuclear interactions can occur when the particle interacts with the atomic nucleus, causing fragmentation. The fragmentation process can be described as a two step process *abrasion* and *ablation*. During the abrasion step the particle and target collide and exited pre-fragments are generated. During the ablation step the remaining nuclei and the pre-fragments de-exite emitting light particles and gamma rays (Durante et al., 2016). This causes the total amount of primary particles to be reduced, for example

only half of the carbon ions reach a bragg-peak depth of 12 cm (Schlegel et al., 2018). The produced fragments are lighter and according to section 2.1.1 have a higher residual range than the primary particle. This causes a characteristic dose-tail in the depth dose curve, seen as an increased dose after the Bragg peak for carbon ions and, albeit less pronounced, for helium ions. (fig. 2.2).

Relative Biological Effectiveness

Ions deliver a different microscopic dose distribution compared to conventional radiation therapy using photons. Consequently, ions can produce the same biological effect at lower absorbed doses. Since most clinical experience with dose prescriptions and tolerance levels in radiation therapy is based on photon treatments, it is important to compare ion doses to photon doses that produce the same biological effects. For this purpose the relative biological effectiveness (RBE) is used, which is defined as (Schlegel et al., 2018)

$$\mathrm{RBE} = \left.\frac{D_{\mathrm{photons}}}{D_{\mathrm{particles}}}\right|_{\text{iso-effect}} . \tag{2.8}$$

Linear Energy Transfer

Linear energy transfer (LET) is a measure for the local energy transferred ($\mathrm{d}E_\Delta$) to a medium through electronic interactions of an ionizing particle per unit length $\mathrm{d}l$.

$$\mathrm{LET}_\Delta = \frac{\mathrm{d}E_\Delta}{\mathrm{d}l} \underset{\Delta\to\infty}{=} \mathcal{S}_{el} \tag{2.9}$$

The energy carried away by secondary electrons with kinetic energy greater than Δ is not considered (Seltzer et al., 2011). LET is an important quantity, as the RBE depends on it, among other parameters (Jäkel, 2020).

2.1.2. Irradiation Techniques

Medical Accelerators

For proton therapy energies of around 30 MeV to 200 MeV are required while for carbon ion therapy energies of around 100 MeV/u to 400 MeV/u are required to reach the necessary depth in the patient (Schlegel et al., 2018). These energies are reached using *cyclotron* or *synchrotron* accelerators, whereby cyclotrons are so far only used in proton therapy. The first carbon cyclotron is currently under developement, with the first treatment expected in 2026 (Letellier et al., 2023). Figure 2.3 illustrates a schematic of both accelerator types. Each uses a magnetic field to keep the particles on a circular trajectory. The radius r of

a particle in a magnetic field B is given by

$$r = \frac{\gamma m v}{qB}, \tag{2.10}$$

whereby m is the particles mass, q its charge, v its velocity and γ the lorentz factor.

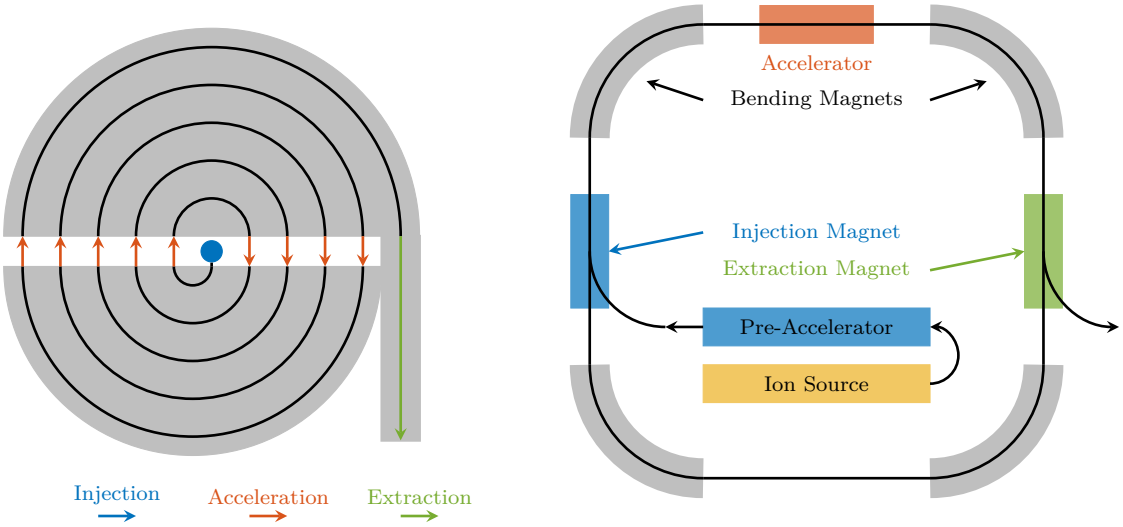

Figure 2.3.: Left: Schematic drawings of a cyclotron. Right: Schematic drawing of a synchrotron. Adapted from Schlegel et al. (2018)

In a classical Lawrence cyclotron protons are injected in the center of a constant magnetic field. An electrical field is applied between two half circles (Dee's) to accelerate the protons. Since the magnetic field stays constant the radius increases at each turn as the velocity increases and the particles move along a spiral path. At high energies the revolution frequency increases which can be compensated either by increasing the magnetic field with radius (isochronous cyclotron) or by decreasing the Dee frequency during acceleration (synchrocyclotron). The extracted beam has a fixed energy that must be degraded with range modulators or compensates to allow for treatment of different tumor depths (Schlegel et al., 2018; Owen et al., 2016).

In a synchrotron, particles are first pre-accelerated to several MeV before being injected into the main accelerato ring, where they are accelerated further via electric fields. Bending magnets are used to keep the particles on a circular path, whereby contrary to cyclotrons the magnetic field strength increases at each revolution in sync to the particle energy. The particles are extracted with a specific energy in a spill lasting several seconds (Schlegel et al., 2018; Owen et al., 2016).

Ion Beam Delivery

There are two main methods of how the particle beam is shaped to deliver the dose to the target volume. The passive beam delivery technique uses a broad beam that is then

confined to the outline of the tumor using personalized collimators. Passive scattering techniques have been mostly replaced by active pencil beam scanning (Durante et al., 2017). Active beam shaping utilizes the electric charge of the particles to deflect a highly focused pencil beam of a specific energy laterally by fast switching magnets, enabling precise scanning across the tumors cross-section this is called an iso-energy slice (IES). During treatment delivery the beams energy is changed to irradiate the tumor in depth (Jäkel, 2009).

While there are quite a few proton centers worldwide there are, as of February 2025, only 16 carbon ion therapy centers. All of these centers are equipped with at least one horizontal fixed beam line, often a vertical or an oblique is also used. Of the 16 carbon centers worldwide only three are equipped with carbon gantrys, one of them is located at the Heidelberg ion therapy facility (HIT). A gantry allows for the ion beam to be rotated around the patient to treat from a variety angles. While proton gantrys are quite common, carbon gantrys are rarer due to the more difficult construction. The higher magnetic rigidity of ions heavier than protons, requires the use of stronger magnets or a larger bending radius. The carbon gantry in Heidelberg has a large bending radius and weighs 570 t, the other carbon gantrys use superconducting magnets (Weinrich et al., 2008; PTCOG, 2025a).

2.2. Physics of Mixed Carbon-Helium Beams

Two ion species with the same mass to charge ratio (m/q) and velocity (β) have the same magnetic rigidity ($B\rho$).

$$B\rho = \frac{m}{q}\gamma\beta c \tag{2.11}$$

whereby γ is the lorentz factor. Thus they can theoretically be accelerated together in a synchrotron.

Fully ionized carbon and helium ions have nearly the same mass to charge ratio of two. However it is not exactly the same, as reported by Renner et al. (2024):

$$\chi = \frac{q_{He}}{m_{He}} / \frac{q_C}{m_C} = 0.99935\,. \tag{2.12}$$

In theory, other combinations of ions would be possible: Helium ions could be used as a primary irradiation in combination with deuterium, however clinical experience for particle therapy with helium ions is limited. Helium ions were just recently commissioned for clinical use at HIT after an initial trial in Berkeley in the 1970s (Tessonnier et al., 2023). Hence, in line with current research efforts, this thesis focuses on mixed beams with carbon ions as the primary ion and helium ions as the secondary.

Currently there are two methods under investigation to create a mixed carbon-helium beam that can be utilized for patient treatment. The first experimental results were

recently presented in 2024 by Graeff et al. (2024), Galonska et al. (2024), and Ondreka et al. (2024), who investigated the extraction of the mixed beam directly from the ion source at GSI in Darmstadt. The second method, investigated by Kausel et al. (2025) and Renner et al. (2024) at MedAutron in Vienna, considers sequential injection of carbon and helium in the synchrotron ring.

2.2.1. Extraction of a Mixed Beam from a Single Ion Source

In this method a methane ion source with helium as a support gas is used, and $^{4}He^{+}$ and $^{12}C^{3+}$ with a mass to charge ratio of four is extracted. In the experiments the ions were then simultaneously accelerated to an energy of 225 MeV/u. All ions were fully stripped in the nozzle. In this method the carbon to helium ratio can be adjusted very easily, by adding helium step wise to the methane ion source and simultaneously recording the optical emission spectrum. During the extraction of the mixed beam, the ratio of carbon to helium varied within ±30% throughout the spill, the ratio was stable and reproducible across multiple spills. One challenge with this method is that the ion source usually contains a small portion of oxygen, thus the beam also contains oxygen. Still, the experiments showed an oxygen contamination of less than 10 %. This oxygen contamination can be minimized by conditioning the ion source for several days before operation, however it could not be fully eliminated. Another challenge of the extraction of the mixed beam was that the position of the helium beam was slightly shifted horizontally compared to the carbon beam. In the iso-center this offset amounted to 1 mm to 2 mm (Graeff et al., 2024; Galonska et al., 2024; Ondreka et al., 2024).

2.2.2. Double Multi-Turn Injection for Generating Mixed Beams

This method for generation of a mixed beam is of special interest to centers that, like MedAustron, are equipped with a pre-accelerator optimized for a mass to charge ratio of three or less. This pre-accelerator makes extraction of a mixed carbon-helium beam from a single ion source, as done at GSI, not feasible.

In the double multi-turn injection method, helium is injected first into the synchrotron. Then the injector is reconfigured, during this helium is stored in the synchrotron ring at flat bottom, i.e it is not accelerated. Next, carbon is injected, during the carbon injection the majority of helium is lost. After both injections the ions are accelerated in the synchrotron.

The carbon-helium ratio can be changed by adjusting several parameters in the injection and extraction, for example the amplitude of the second injection bump. An injection bump, is a deviation of the orbit at the injection point, to align the trajectory of the stored beam better with the trajectory of the injected beam (Tecker, 2021). The optimal tuning

of these parameters to achieve and maintain the desired mixing ratio is under investigation. During experiments a mixed carbon-helium beam with an energy of 262.3 MeV/u was generated.

A challenge during extraction is the offset (eq. (2.12)) of the mass to charge ratio between both ion species. This slight offset causes the helium energy to be slightly higher, in the order of approximately one to three standard deviations of the energy distribution. It has to be noted that both ion species have different distribution in phasespace (Kausel et al., 2025; Renner et al., 2024).

2.3. Ion Imaging

Ion imaging has gained interest in the last years, due to the systematic uncertainties in relating the housfield unit (HU) values measured with a computed tomography (CT) to the RSP values and/or material information needed for dose calculation. This could be counteracted by using, for example, protons for volumetric imaging (proton CT), which would directly measure the RSP information (Parodi, 2014). Furthermore, particle radiography can be used to verify the patient position pretreatment or the water equivalent thickness (WET) of the patient. WET is the thickness of water that would result in the same energy loss as experienced by the particles when traversing a material of thickness L,

$$\mathrm{WET} = \int_0^L \mathrm{RSP}\,\mathrm{d}x = \int_{E_{init}}^{E_{final}} \frac{1}{-\left\langle \frac{\mathrm{d}E}{\mathrm{d}z} \right\rangle}\,\mathrm{d}E = R(E_{init}) - R(E_{final})\,. \tag{2.13}$$

2.3.1. Ion Imaging Systems

There are two main types of imaging systems: *integrating* and *tracking* or *single-event* imaging. Integrated mode devices integrate the signal of an undetermined number of incident ions, and don't resolve single ion events. Although this approach is generally more cost-effective, it sacrifices spatial resolution.

A schematic setup of a single-event imaging system is shown in fig. 2.4. Hereby tracker planes are used to infer the ions path which is then used to estimate the trajectory across the imaged object (Poludniowski et al., 2015). Varying set ups with varying number of tracker plans are possible. A set up with 4 planes can be used to measure position and angle before and after the patient, but simpler setups utilizing 2 planes to measure only the position before and after the patient or only 1 plane to measure the position after the patient are used. For the simpler, more compact set ups the missing direction or position information has to be approximated.

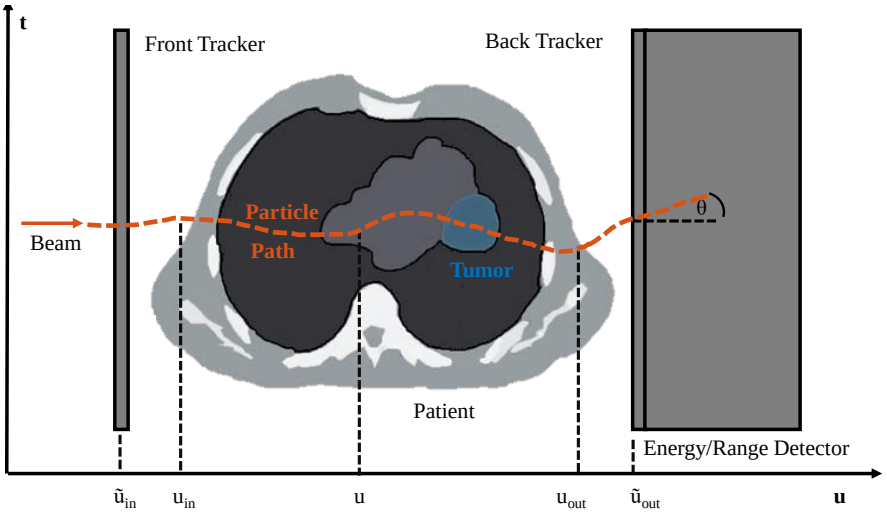

Figure 2.4.: Schematic setup of an ion imaging detector, featuring a front and back tracker as well as an energy detector. Highlighted is an example particle path and the variables used in image reconstruction.

2.3.2. Image Reconstruction for Single-Event Ion Imaging

The path of an ion across an object can be determined by the maximum likelihood path (MLP) formalism. To describe the MLP, the u axis defining the general direction of the beam and the t axis, which is orthogonal to the u axis and describes the lateral displacement of the particle, are introduced, as seen in fig. 2.4. The position and direction of an ion a depth u is described as $Y(u) = (t(u), \theta(u))^T$, with *theta* the direction angle (Schulte et al., 2008).

The joint likelihood of a particle passing through Y and exiting at Y_{out} giving it entered the patient at Y_{in}, is given as follows (Krah et al., 2018)

$$L(Y, Y_{out}|Y_{in}) \propto \exp\left[-\frac{1}{2}\Big((Y - R_0 Y_{in})^T \Sigma_1^{-1}(Y - R_0 Y_{in}) + (Y_{out} - R_1 Y)^T \Sigma_2^{-1}(Y_{out} - R_1 Y)\Big)\right]. \tag{2.14}$$

Hereby the matrices R_0,R_1 are translation matrices and defined as follows

$$R_0 = \begin{pmatrix} 1 & u - u_{in} \\ 0 & 1 \end{pmatrix}, \qquad R_2 = \begin{pmatrix} 1 & u_{out} - u \\ 0 & 1 \end{pmatrix}. \tag{2.15}$$

The matrices Σ_1 and Σ_2 are covariance matrices describing the amount of spatial and

angular spread due to MCS, and use the scattering moments defined in section 2.1.1

$$\Sigma_1 = \begin{pmatrix} A_2(u_{in}, u) & A_1(u_{in}, u) \\ A_1(u_{in}, u) & A_0(u_{in}, u) \end{pmatrix}, \qquad \Sigma_2 = \begin{pmatrix} A_2(u, u_{out}) & A_1(u, u_{out}) \\ A_1(u, u_{out}) & A_0(u, u_{out}) \end{pmatrix}. \tag{2.16}$$

With this the MLP is optimized by maximizing the likelihood in section 2.3.2 with respect to Y, which is given as (Schulte et al., 2008).

$$Y_{MLP} = \left(\Sigma_1^{-1} + R_1^T \Sigma_2^{-1} R_1\right)^{-1} \left(\Sigma_1^{-1} R_0 Y_{in} + R_1^T \Sigma_2^{-1} Y_{out}\right). \tag{2.17}$$

Recently Krah et al. (2018) extended this path formalism, adding additional co-variance matrices to describe uncertainity's of entrance and exit measurements.

After reconstruction of the particle path, several methods can be used to reconstruct the radiograph image. Plane-of-interest binning (PIB) bins the particles according to their lateral position at depth u, for example the isocenter position. The WET value of the image pixel is the mean WET of all traversing particles (Gehrke et al., 2018a; DeJongh et al., 2021).

2.4. Inverse Treatment Planning For Ion Treatments

The aim of radiation therapy is to apply adequate dose to the tumor, to enable a curative or palliative treatment. At the same time the dose delivered to the rest of the body, especially to an organ-at-risk (OAR) has to be minimized (Schlegel et al., 2018). The conventional workflow of treatment planning is summarized in fig. 2.5

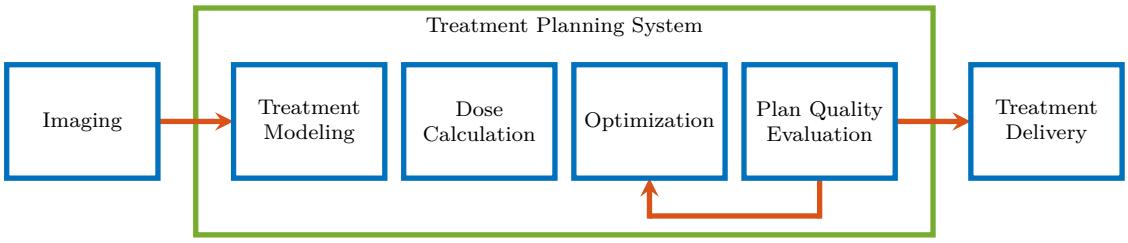

Figure 2.5.: Treatment planning workflow with particular emphasis one the tasks carried out within the treatment planning system

The first step is *Imaging*. The CT image has two purposes, firstly it is used to identify and segment the anatomical regions of interest in the patient. Secondly the CT also provides the photon attenuation value of each voxel (a 3D analog to pixels), which is converted to RSP or an approximate material decomposition for dose calculation.

In the next step the basic parameters of the treatment are defined, such as the angles of irradiation. Using this information the dose to be delivered is calculated and optimized based on goals defined by a clinician. Afterwards the optimized plan is evaluated by inspecting the dose distribution and plan quality metrics. If these metrics are satisfactory,

the treatment is delivered otherwise the optimization process is repeated with adjusted parameters until a satisfactory plan is achieved. To reduce negative side effects, the treatment is delivered over the course of several days or fractions. (Schlegel et al., 2018).

In particle therapy, commonly intensity modulated particle therapy (IMPT) is used. IMPT uses small pencil beams of different energy and lateral position, whose intensity can be adjusted to optimally irradiate the tumor (Lomax, 1999). Figure 2.6 is an illustration of the ray and spot concept used to define the pencil beam scanning grid within the treatment planning software matRad (Abbani et al., 2024; Wieser et al., 2017). From a virtual point source (●) rays (—) with equal lateral spacing are emitted. For each ray multiple energys are selected, such that the Bragg-peak of a specific ray with a specific energy is at approximately the spots (●) position, and within the target (—). One spot represents a focused pencil beam with the appropriate energy and lateral position.

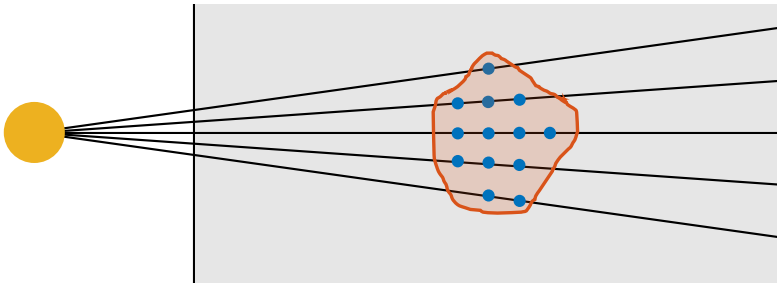

Figure 2.6.: Schematic visualization of the pencil-beam scanning grid. The virtual source is ● the rays are represented by —, the spots are represented by ● and — outlines the target volume within the patient. Adapted from the matRad documentation (matRad, 2025).

2.4.1. Dose Calculation

Analytical Dose Calculation

For fast analytical dose calculation the pencil beam method can be used. The dose contribution of pencil beamlet j to voxel i is calculated by separating the depth-dependent part Z from the lateral scattering component L, as described by Hong et al. (1996):

$$D_{ij} = L_{ij}\left(r_{ij}, z_{ij}, E_{0j}\right) Z_{ij}\left(z_{ij}, E_{0j}\right) . \tag{2.18}$$

The lateral component can be described by a radial Gaussian function in polar coordinates

$$L_{ij}\left(r_{ij}, z_{ij}, E_{0j}\right) = \frac{1}{2\pi\sigma_{\text{tot}}(z_{ij}, E_{0j})^2} \exp\left(-\frac{r_{ij}^2}{2\sigma_{\text{tot}}(z_{ij}, E_{0j})^2}\right) . \tag{2.19}$$

Hereby E_{0j} is the initial energy of pencil beam j, r_{ij} the radial distance of voxel i to the ray and z_{ij} is the water equivalent path length (WEPL) oft the voxel along the ray closest to voxel i. The WEPL is calculated by ray tracing (Siddon, 1985), hereby a line integral of the RSP of the patient from the beam source to the voxel of interest is calculated. The

single Gaussian function in eq. (2.19) is not sufficient to model the wider low dose bath from strongly scattered particles. Consequently, a weighted sum of multiple Gaussian functions is also used (Parodi et al., 2013; Tessonnier et al., 2017).

The beam broadening σ_{tot} is calculated from the initial beam width before the patient and the depth dependent kernel component (Schlegel et al., 2018),

$$\sigma_{\text{tot}}^2(z_{ij}, E_{0j}) = \sigma_{\text{init}}(E_{0j})^2 + \sigma^2(z_{ij}, E_{0j})\,. \tag{2.20}$$

In clinical applications often tabulated data is used, meaning that for each available energy a depth dose curve ($Z_{ij}\,(z_{ij}, E_{0j})$), similar to fig. 2.2, as well as the lateral components ($\sigma(z_{ij}, E_{0j})$) are stored. These look up tables are acquired from measurements or MC simulations (Parodi et al., 2012; Parodi et al., 2013; Tessonnier et al., 2023).

Monte Carlo Dose Calculation

Monte carlo (MC) methods use sampling to estimate numerical results. For the transport of radiation, this means solving the integro-differential radiative transport equation, and practically is implemented as follows: a random number is drawn to sample the current step length, that is, the distance between two interactions in the material. The distribution of step lengths depends on the density and the total interaction cross section. Another random number determines which interaction takes place at the end of the step length, hereby the probability of each interaction is given by the relative contribution of the interactions cross section to the total cross section. The energy and direction of the particle as well as possible secondary particles are calculated with different models depending on the interaction. This process is repeated iteratively until the primary particle and all possible secondary's are fully transported, this is called a histrory (Cirrone et al., 2023; Berger, 1963).

To reduce the computation load condensed history monte carlo is introduced, hereby numerous individual interactions are combined, condenssing, the effect of many smaller interactions into a single larger interaction. While the condensed history approach is computationally more efficient, it is less precise. Therefore a mixed procedure can be used, whereby events causing large energy losses are simulated separately. For the MC tool Geant4 (Agostinelli et al., 2003; Allison et al., 2016) electromagnetic interactions such as ionization and elastic scattering are implemented with the condensed history approach using the Bethe-Bloch formula and MCS models. Nuclear interactions are modeled individually, the used cross sections are either based on theoretical models or open source databases. (Cirrone et al., 2023; Berger, 1963).

MC dose calculation is considered the most accurate dose calculation method, especially in complex geometries with large lateral inhomogeneities. The computational accuracy depends on accurate knowledge of the simulated anatomy and material composition as

well as the considered physical processes the individual cross sections and the computation time (Schlegel et al., 2018; Paganetti, 2012).

Beam Parameters for MC simulations As mentioned by Parodi et al. (2012) and Parodi et al. (2013) modeling of the treatment beam can be useful to support start-up of a particle center and treatment planning. To model the beam two approaches can be used: either the full beam line including the components within the nozzle is simulated or the phase space after the nozzle is calculated. In the latter case, parameters such as mean energy, energy spread and beam optics must be inferred from measurements as they are used in MC tools like TOPAS (Perl et al., 2012; Faddegon et al., 2020) to model the beam.

Since the initial mean energy of the particles determines their range in tissue, and the initial energy spread contributes to the broadening of the Bragg peak, both parameters can be estimated from a measured depth dose curve. The initial mean energy is calculated from the known range using an established energy–range relationship (Berger et al., 2009), while the energy spread (σ_E^2) can be determined by (Bortfeld, 1997):

$$\sigma_E^2 = \frac{\sigma_{tot}^2 - \sigma_{mono}^2}{\left(\frac{\mathrm{d}R}{\mathrm{d}E}\right)^2}. \tag{2.21}$$

Whereby σ_{tot} is the measured width of the Bragg peak and σ_{mono} the width of a mono-energetic beam with no initial energy spread, estimated by a MC simulation of a mono-energetic beam. The term $\frac{\mathrm{d}R}{\mathrm{d}E}$ represents the derivative of the energy-range relation ship.

Beam optic parameters are determined by measuring the spot sizes in air at various distances from the nozzle. Using the Courant–Snyder formalism (Courant et al., 1958), the spot size in the x and y directions ($\sigma_{x,y}(z)$) at a given position z along the beam axis is related to the angular spread (beam divergence) ($\sigma_{\theta,\phi}(z)$) and their correlation ($\rho_{x\theta,y\phi}$) at the iso-center ($z = 0$) as follows:

$$\sigma_x^2(z) = \sigma_x^2(0) - 2\rho_{x\theta}(0)\sigma_x(0)z + \sigma_\theta^2(0)z^2\,, \tag{2.22}$$

$$\rho_{x\theta}(z) = \frac{\rho_{x\theta}(0)\sigma_x(0) - \sigma_\theta(0)z}{\sigma_x(z)}\,, \tag{2.23}$$

$$\sigma_\theta(z) = \sigma_\theta(0)\,. \tag{2.24}$$

Analogous expressions apply for the y axis. By fitting measured data to these formulas, the beam optics at the nozzle can be calculated (Huang et al., 2018).

2.4.2. Computational Treatment Plan Optimization

During treatment delivery each pencil-beam has a different particle fluence, which is represented through a fluence vector w. This allows for the calculation of the total dose d delivered to a voxel i by all pencil beams as

$$d_i = \sum_j D_{ij} w_j \,. \tag{2.25}$$

The matrix D is called the dose-influence matrix (Schlegel et al., 2018). For a given setup, the optimal fluence vector $w^\star$ can be found by solving the optimization problem

$$w^\star = \arg\min_w \mathcal{F}(d(w)) = \arg\min_w \sum_s p_s \mathcal{F}_s(d(w)) \quad \text{subject to } w \geq 0 \tag{2.26}$$

with the objective function $\mathcal{F}$. Here, the objective function is a weighted sum of multiple components describing different treatment goals to be traded against each other. Other multi-criteria optimization approaches can be used here but are out of scope for this thesis. In the weighted-sum formulation, the relative weighting of these prescriptions is p_s (Wieser et al., 2017). Based on a penalized least squares fit of the dose distribution d to the prescribed dose $d^\star$, the most fundamental objective function is

$$\mathcal{F}^{SD}(d) = \frac{1}{N_S} \sum_{i \in S} (d_i - d^\star)^2 \,, \tag{2.27}$$

given here for a volume of interest (VOI) S with N_S voxels. The objective and constraints are dependent on the optimization variable w through d. The computation of the gradient $\nabla_w \mathcal{F}$ separates according to the chain rule into

$$\nabla_w \mathcal{F} = \frac{\partial \mathcal{F}}{\partial w} = \left(\frac{\partial d}{\partial w}\right)^T \frac{\partial \mathcal{F}}{\partial d} \,. \tag{2.28}$$

For OAR it would be ideal if they received no dose at all, this is however unfeasible which is why doses above a certain tolerance value d^{max} are penalized. Similarly for targets it might be desirable to penalize under-dosage separately, as this might result in insufficient effectiveness of the treatment. This can be achieved by incorporating heavyside step-functions, with this eq. (2.27) becomes

$$\mathcal{F}^{OD}(d) = \frac{1}{N_S} \sum_{i \in S} \Theta(d_i - d^{max})(d_i - d^{max})^2 \,, \tag{2.29}$$

$$\mathcal{F}^{UD}(d) = \frac{1}{N_S} \sum_{i \in S} \Theta(d^{min} - d_i)(d_i - d^{min})^2 \,, \tag{2.30}$$

whereby Θ is the Heaviside step function. For solving the optimization problem Newtonian methods can be used.

2.4.3. Plan Quality Evaluation

Among other metrics, treatment plans are evaluated, by visual inspection of the dose distribution and dose volume histogram (DVH). The quality indicator D_x, describes the minimum dose received by $x\,\%$ of the VOI. A good indication of the maximum dose delivered to a VOI is the D_2 as it eliminates localized hot spots of the dose, similarly D_{98} is a good measure of the minimum delivered dose. For the target the D_{95} is especially relevant, as it is used to asses target coverage (Schlegel et al., 2018).

To compare two dose distributions in radiation therapy quality assurance, typically between a calculated and a measured dose the gamma pass index can be used. The quality index measure γ at each point (r_R) of the reference dose distribution (R) for the evaluated dose distribution (E) is given as (Low et al., 1998).

$$\gamma(r_R) = \min\left(\Gamma(r_E, r_R) | \forall r_E\right) \tag{2.31}$$

where

$$\Gamma(r_E, r_R) = \sqrt{\frac{|r_R - r_E|^2}{\Delta d_M^2} + \frac{(D_R(r_R) - D_E(r_E))^2}{\Delta D_M^2}}\,. \tag{2.32}$$

The parameter Δd_M represents the distance to agreement criteria, and the parameter ΔD_M the dose difference criteria. Typically ΔD_M is given in %, relative to a global normalization such as the prescribed dose per fraction or the maximum dose (Anetai et al., 2022). If $\gamma(r_R) \leq 1$ the point r_R passes the gamma index test, often the percentage of passed points is reported.

2.5. Uncertainty Management In Particle Therapy

A major advantage of particle therapy is the highly localized dose deposition at the end of the particles range. However this also means that the range needs to be precomputed as accurately as possible during treatment planning to match delivery and to avoid under-dosing of the tumor or over-dosing of OAR.

2.5.1. Sources of Uncertainty

Range uncertainties arise from organ motion, setup and anatomical variations as well as approximations in the dose calculation. Paganetti (2012) estimated the uncertainty in proton range to be 3.5 %, along with an additional fixed uncertainty of 1 mm.

Anatomical variations can occur between delivery of the dose and the acquisition of the CT used for treatment planning. This can be different filling of the rectum, weight loss or weight gain of the patient, tumor shrinkage or also daily positioning errors.

Approximations in the dose calculation include, that a planning system typically reports

dose-to-water not dose-to-material which can lead to a different range, specifically in bone. Uncertainty in the conversion of the CT HU values to RSP result in uncertainties in the ion range. Additional artifacts in the CT, specifically metal artifacts can affect the accuracy of the range prediction (Paganetti, 2009).

Range changes due to different cavity fillings, such as in the rectum, behave differently from uncertainties in the RSP conversion. Changes from cavity fillings are highly localized and vary from day to day. In contrast, RSP conversion uncertainties lead to more global range shifts that affect all treatment days and are proportional to the amount and type of tissue the beam traverses.

If the organ that is irradiated is affected by motion, as in lung therapy, there is an additional source of uncertainty. The target, in the lung, is moving on the same time scale as the scanning particle beam. This results in a time-dependent distortion of the planned dose called interplay effect (Kraus et al., 2011).

In intensity modulated photon therapy motion and setup uncertainties are typically accounted for by adding margins around the clinical target volume (CTV) creating the planning target volume (PTV). However this margin concept relies on the static dose cloud approximation, i.e changes in the patient's anatomy do not change the dose distribution in treatment room coordinates. This means than as long as the CTV stays within the PTV it receives the prescribed dose. This approximation is not correct for intensity modulated particle therapy, as range errors cause an inhomogeneous dose distribution within the CTV that PTV margins alone can not address (Unkelbach et al., 2018).

2.5.2. Mitigation of Range Uncertainties

For intensity modulated particle therapy, where the static dose cloud approximation is not valid, robust planning was developed. In robust planning dose distributions d^k for a set of error scenarios are calculated. Setup errors are modeled as rigid shifts of the patient with respect to the iso-center, range errors are modeled by scaling of the CT housfield units.

There are several approaches to include these scenarios in the optimization process, for example: The *stochastic programming approach* weights each error scenario with its associated importance weight and minimizes the expected value of the objective function, therefore a robust plan yields a good dose distribution for the most important error scenarios. The *worst-case approach* calculates the maximum of the objective function over the error scenarios, which is then minimized with respect to the particle fluence. This aims to find a treatment plan that is as good as possible for the worst error scenario (Unkelbach et al., 2018).

Cristoforetti et al. (2025) recently implemented an optimization algorithm, that does not rely on the scenario concept, instead an expected dose influence matrix and a total

variance matrix is calculated from the scenarios and used during optimization of the treatment plan. While the scenario doses are still calculated this scenario free concept during optimization saves memory.

2.5.3. Range Verification Methods

With these mentioned uncertaintys of the ion range, verifying that a treatment plan is delivered correctly is important. Some methods for range verification, are presented below.

Positron Emission Tomography Imaging

Nuclear reactions can cause exited nuclei, leading to subsequent radioactive decay. For positron emission tomography (PET) imaging β^+ channels are important as the emitted positron annihilates with an electron, leading to the creation of two 511 keV photons. These photons are measured in PET. Typical half-lives of isotopes produced in this method range from a few milliseconds (^{12}N) up to tens of minutes (^{11}C). Thus, the radiation induced activity can be detected during or after the irradiation, with acquisition time taking up to 30 min however. A major challenge in this method is the correlation of the activity signal with the delivered dose and range. For heavy ions, like carbon ions the peak of the activity signal is located shortly before the Bragg peak. A disadvantage of this method is the delay of the PET signal compared to beam delivery. For verification the measured images are compared to expected images calculated analytically, with MC or with a reference measurement from a previous treatment fraction (Parodi et al., 2018).

Prompt Gamma Imaging

During inelastic interactions of the incident ions with nuclei in the irradiated tissues, an exited nuclei can emit prompt gamma radiation that can be measured. These emissions occur within nanoseconds of the interaction. Since the prompt gammas emitted in these reaction have a higher energy (2 MeV - 10 MeV) compared to those used in diagnostic studies (<1 MeV), new detectors were developed for prompt gamma imaging (Parodi et al., 2018). The measured emission profile of prompt gammas correlates well with the depth dose profile, and has been used to measure range changes on a spot level. Hereby the measured prompt gamma profiles are compared to expected emission profiles, calculated using a pencil-beam algorithm, which is based on reference profiles calculated with MC. The emission profiles are then converted into expected detection profiles considering the geometry and the patient-specific attenuation with a CT (Xie et al., 2017).

Magnetic Resonance Imaging

With magnetic resonance imaging (MRI) the patients anatomy can be monitored during therapy, allowing for an estimate of the particle range. MRI offers high soft tissue contrast without ionizing radiation and thus additional dose. While already clinically applied in photon therapy (Ng et al., 2023), charged particle beams are directly affected by the magnetic field, rendering the implementation of online MR-guided particle therapy more challenging. As the magnetic fields of the MRI scanner distort, bend the particle dose and has to be taken into account. Furthermore, contrary to CT, MRI does not measure electron density information that can be correlated to RSP for dose calculation. One option is to generate a synthetic CT from the MRI data (Hoffmann et al., 2020).

2.5.4. Motion Management

To mitigate motion related issues, there are several approaches. Deep inspiration breath hold or gating is used to minimize the tumor motion due to breathing. In deep inspiration breath hold the patient uses the same reproducible, deep inspiration level during treatment planning and delivery (Hanley et al., 1999). Respiratory gating tracks the respiratory phase, and irradiation is only performed during specific phases. The motion can be tracked, for example, by surface imaging of the abdomen (Ohara et al., 1989; Mori et al., 2018).

The interplay effect describes the dose degradation caused by the interaction between patient motion and the scanning of the particle beam. To mitigate this effect, re-scanning techniques which were first introduced by Phillips et al. (1992) are used. Hereby the tumor is scanned multiple times to average out the changes in the dose distribution caused by motion.

3

Materials and Methods

This chapter starts with an introduction into the hardware framework (Imaging Detector) (section 3.1). Then the background of the developed module for mixed beam treatment planning is introduced as well as the investigated treatment planning strategies considering the residual helium range (section 3.2). Next the implantation of the developed module within the treatment planning software matRad and the MC tool TOPAS is discussed (section 3.3). Then the potential for treatment verification using the mixed beams is explored (section 3.4). Lastly, the used patient and phantom data (section 3.5).

3.1. The Helium Imaging Detector

Concurrently to this work, a detector for mixed carbon-helium beams is being developed. Therefore a radiography system provided by ProtonVDA (DeJongh et al., 2021), used original for proton imaging was adapted for helium imaging (Pryanichnikov et al., 2025b; Pryanichnikov et al., 2025a; Pryanichnikov et al., 2025d). The goal is to first adapt this detector for helium imaging before moving on to mixed beams. Pryanichnikov et al. (2025c) recently investigated the feasibility of using proton and helium radiographs for intrafractional motion management.

The ProtonVDA detector is a single-event imaging system, whereby trackers measure the position of individual particles up and downstream of the patient and a scintillating block measures the residual energy. The tracker planes consist of four layers of scintillating fibers, two for the x position measurement and two for the y position measurement. The sensitive area is 38.4×38.4cm. The entrance position can be determined by a 0.5 mm pitch. The energy detector is a $40 \times 40 \times 13$cm scintillator block (Eljen Technology, model EJ230) with 16, 76 mm diameter vacuum photo multiplier tubes (PMT) (Hamamatsu, model R6091) attached to it. The maximum event rate of the data acquisition system is 3 MHz.

3.1.1. Calibration of the Energy Detector

To measure the residual range of a proton or helium ions an electronic board combines the signals from the 16 PMT into four weighted sum signals E, U, V and C. Calibrations are

necessary to convert the E, U, V and C signals to residual ion range. During Calibration ions with known energy and residual range R are scanned over the sensitive field of the tracking detectors and the calibration data is binned intro a calibration grid with points for each x, y fiber position and R. From this data a covariance matrix $K(x, y, R)$ for each point is calculated. Due to technical difficulties, only the E, U and V channel were available. The calibration process remains the same except for an additional row and column describing the C data in the covariance matrix,

$$K_{EUV}(x, y, R) = \begin{pmatrix} \mathrm{Cov}(EE) & \mathrm{Cov}(EU) & \mathrm{Cov}(VE)) \\ \mathrm{Cov}(UE) & \mathrm{Cov}(UU) & \mathrm{Cov}(UV) \\ \mathrm{Cov}(VE) & \mathrm{Cov}(VU) & \mathrm{Cov}(VV) \end{pmatrix} . \tag{3.1}$$

Whereby $\mathrm{Cov}(AB)$ is the covariance of the two variables A and B for the point (x, y, R) in the calibration grid.

To determine the residual range of an ion with incident position (x,y), the minimum of $\chi^2(x, y, R)$ as a function of R is calculated. Since the initial energy is known from the accelerator the WET can be calculated as the difference from initial range and measured range (DeJongh et al., 2021).

$$\chi^2(x, y, R) = \begin{bmatrix} E - \bar{E}(x, y, R) \\ U - \bar{U}(x, y, R) \\ V - \bar{V}(x, y, R) \end{bmatrix}^T K_{EUV}(x, y, R)^{-1} \begin{bmatrix} E - \bar{E}(x, y, R) \\ U - \bar{U}(x, y, R) \\ V - \bar{V}(x, y, R) \end{bmatrix} \tag{3.2}$$

Whereby $\bar{E}(x, y, R)$ is the mean E signal for the calibration point (x, y, R)

Calibration of Helium Ions

Calibration for helium ions was performed with 22 energies ranging from 97.26 MeV/u to 125.40 MeV/u. During the calibration a PMMA block of 5.8 cm thickness was placed in front of the detector, to prevent saturation of the energy detector. Cuts were applied to the E signal to filter out helium fragments. These cuts were dependent on the incident helium energy, for the lowest helium energy a lower cut of 1400 and a upper cut of 3600 was applied, for the highest energy a lower cut of 10 000 and a upper of 16 000. Additionally a 2σ cut was applied in preprocessing stages of E,U and V data.

3.1.2. Reconstruction of the Imaging Data

Since the trackers measure only position and not direction the MLP algorithm, presented in section 2.3.2, was adapted by Penfold (2011). Hereby the entry direction is calculated from the measured upstream position and the known beam position at the nozzle, the exit direction is calculated from the measured downstream and upstream position. Additionally a hull projection algorithm is used to calculate the entry and exit position of the

patient from the measured position at the trackers (Ordoñez et al., 2019). If not stated otherwise, all data was acquired and reconstructed without the upstream tracker, hereby the position at a virtual upstream tracker is extrapolated from the known position and direction of the beam at the nozzle.

During image reconstruction the data is filtered, applying statistical cuts: a 3σ cut is applied to the lateral displacement between entry and exit positions, to filter out large angle scattering, and a 3σ cut was also applied to the WET of individual events to filter out unusually large energy loses.

3.1.3. Acquired Radiographs

For measurements of the helium radiographs, the experimental beamline at the Heidelberg ion therapy facility (HIT) was used. These measurements were performed without the upstream tracker using an experimental low intensity mode. During the measurements the feedback system controlling the intensity of the beam was turned off. The results of these measurements are presented in section 4.1.

WET Accuracy Measurements

To analyze the WET accuracy of the Helium imaging detector, a validation measurement with a Gammex Phantom was designed. This is a cylindrical PMMA phantom with cylindrical inserts made of tissue equivalent materials. The used inserts were Solid Water, CB2-30 %, CB2-50 %, Liver, Brain, Muscle, Inner Bone, Cortical Bone and B-200 Bone.

The stopping power is described by the Bethe-Bloch eq. (2.3), from which the RSP can be approximated by (Schneider et al., 1996):

$$\mathrm{RSP} \approx \rho_e^w \frac{\ln\left(\frac{2m_e c^2 \beta^2}{I_m(1-\beta^2)}\right) - \beta^2}{\ln\left(\frac{2m_e c^2 \beta^2}{I_w(1-\beta^2)}\right) - \beta^2} \,. \tag{3.3}$$

The electron density relative to water is ρ_e^w, the electron mass is m_e, the particles velocity relative to the speed of light c is β and the ionization potential of the material and water is I_m and I_w respectively.

The energy dependence of the RSP is small. For materials and energies relevant for therapy and imaging Arbor et al., 2015 showed a variation of below 0.7 % for protons. Thus, the ground truth WET was calculated with the length of the cylinder l as:

$$\mathrm{WET} \approx l \cdot \mathrm{RSP} = l \cdot \rho_e^w \frac{\ln\left(\frac{2m_e c^2 \beta^2}{I_m(1-\beta^2)}\right) - \beta^2}{\ln\left(\frac{2m_e c^2 \beta^2}{I_w(1-\beta^2)}\right) - \beta^2} \,. \tag{3.4}$$

The length of the inserts is 7 cm and the length of the PMMA phantom is 10 cm. For the calculation β was calculated from the used initial energy. The relative electron

density to water was provided by the manufacturer of the phantom, see appendix A.1. The ionization potential of the materials was taken from Hünemohr et al. (2013), for water an ionization potential of 78 eV was used.

A helium radiograph (HeRad) was acquired using the energies 100, 145, 160 MeV/u. For each energy the beam was scanned 6 times, 3 times from the upper left corner to the lower right corner, and 3 times the other way around. To average out intensity variations during the helium spill. The image was reconstructed using data from all acquisitions. The mean and standard deviation of the WET values of the image pixels for each tissue insert and for an region of interest (ROI) in the PMMA cylinder was recorded.

In addition to the measured radiographs, MC simulated radiographs were calculated for comparison, more detail on the simulation of the detector is given in section 3.3.4. The MC simulations were performed using the same energies as used in the measurements. Furthermore the geometry of the Gammex Phantom was modeled, with the elemental composition of the inserts taken from Hünemohr et al. (2013). The simulation was performed with $1 \cdot 10^7$ particles per energy.

Anthropomorphic Phantom Measurements

The Beathing Radiotherapy Visual monitoring, Imaging and Dosimetric Anthropomorphic Phantom (BRaVIDA) (Bakhtiari Moghaddam et al., 2024; Bakhtiari Moghaddam, 2022) was used to acquire anthropomorphic images. The organs of the phantom have HU values comparable to human tissues. An image of the phantom can be found in the appendix fig. A.2. HeRads of the abdominal region with energy of 190 MeV/u and 220 MeV/u were acquired. Again the beam was scanned multiple times to average out intensity variations of the spill.

3.2. Treatment Planning for Mixed Carbon-Helium Beams

3.2.1. Dose Calculation and Optimization

For treatment planning, dose calculation with the fast pencil-beam algorithm (section 2.4.1) is used. For mixed-beam dose calculation with the pencil-beam algorithm, compatible carbon and helium beam specifications and kernel datasets are created, as described in the following. These data sets will allow the calculation of the carbon dose and the mixed-in helium dose as well as the combined carbon-helium dose.

Creation of the Helium Kernel Data Set

The carbon kernel set used was an existing kernel set from HIT. In the modeling of the helium kernel set is was assumed that both ion species have the same phase space parameterization, i.e. the same energy spectrum and optical parameters. While first studies on experimental beams (Graeff et al., 2024; Kausel et al., 2025) show differences in the two ion species phase spaces depending on the acceleration method, assuming similar phase spaces serves as a good first-order approximation independent of the specific simultaneous acceleration method.

As the exact phase space parameterization for the primary carbon beam was not know, the beam parameters were estimated following the approach presented in section 2.4.1. The Courant-Synder formula (Courant et al., 1958) was used to calculate the beam optics given the provided spot sizes tables of the carbon kernel set. The energy spread was determined for five energies (89, 196, 274, 342, 430 MeV/u) within the carbon kernel set. An exponential decay function was fitted to the calculated energy spreads to enable interpolation for intermediate energies. The energy value specified in the kernel set was used as the mean energy.

A helium particle beam with the previously estimated parameters impinging on a cylindrical water phantom was simulated. Instead of using the recommended material G4_WATER (Geant4-Colloboration, 2024), a new water material was defined with identical density (1 g/cm^3), ionization potential (78 eV), and elemental composition. This substitution was made because certain versions of Geant4 (10.7) and TOPAS (3.8.p1, 3.9) have been reported to underestimate the helium range by several cm when G4_WATER is used [1]

A schematic set up of the simulation geometry can be seen in fig. 3.1. The distance from the beam source to the surface of the cylinder was the nozzle to isocenter distance of the carbon kernel set. Accordingly there is about 1 m of air between the source and the cylinder. In the cylinder the deposited energy was scored in depth and radially. The LET of the helium ions was also scored in depth. For this purpose a custom LET scorer extension for TOPAS was written. The extension calculates the LET of primary and secondary ions, including the energy deposited by associated secondary electrons. The LET can be weighted by either fluence or dose.

The LET curves were used to calculate the RBE weighted dose of the helium ions in the treatment plans. The scored deposited energy was fitted radially at each depth with a sum of three weighted Gaussian functions to extract the lateral dose profiles that where

[1] https://geant4-forum.web.cern.ch/t/helium-4-ions-ranges-in-water/8229,visited on 05/07/2025
https://groups.google.com/g/topas-mc-users/c/xfSssXZG9zg/m/bcyCboXiBAAJ,visited on 05/07/2025
https://groups.google.com/g/topas-mc-users/c/kOyFFmcpuHg/m/ZHSOk2aRAgAJ,visited on 05/07/2025

used to calculate the dose with a pencil-beam algorithm as described in section 2.4.1.

To save simulation time the length of the cylinder was always 1.5 times the expected range. The radius of the cylinder was constant for every energy at 40 cm. To further optimize between accuracy and simulation time different scoring bin widths were used for different regions. A coarser depth binning of 2 mm in depth was used in the plateau region. In a 2 cm region around the estimated Braag-peak a finer depth binning of 0.2 mm was used. In the center of the cylinder, up to a radius of 7 cm a finer radial scoring of 0.5 mm was used, in the outer region the radial bin width increased to 10 mm. The simulated helium kernel set is presented in section 4.2.

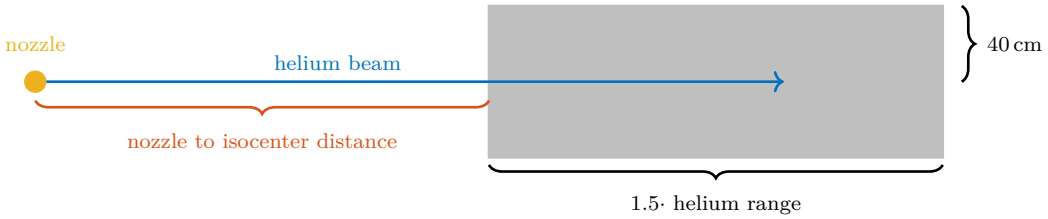

Figure 3.1.: Schematic geometrical setup of the monte carlo simulation for the creation of the helium kernel set.

Helium Energy Range Relationship

From the simulated depth dose curve of each energy, the range was extracted as the 80 % distal fall off point. The beam energies were subdivided into three energy intervals, [0 MeV/u, 169.17 MeV/u], (169.17 MeV/u, 297.79 MeV/u), [297.79 MeV/u, ∞]. In the second and third interval the function

$$R = \alpha E^p + c, \tag{3.5}$$

was fitted, with R the range and E the energy. In the first interval the parameter $c = 0$ was used, to ensure a zero crossing. The fitted helium energy range relation ship is presented in section 4.2.1.

Calculation and Optimization of the Carbon-Helium RBE Weighted Dose

It is expected that the helium contribution to the total dose is low. As seen in eq. (2.3) the stopping power scales with Z^2, therefore helium ions should deposit around $2^2/6^2 = 11.1\,\%$ of the carbon dose. Adding in the lower helium fluence (10 %), an additional absorbed dose of around 1 % is expected.

As mentioned in section 2.1.1 ions have an enhanced RBE compared to photons. This has to be taken into account during treatment planning. To compute the total combined biological effectiveness of a mixed beam the biological effect (ϵ) is used. In the linear

quadratic (LQ) model for cell kill ϵ is given by the negative logarithmic of the fraction of surviving cells (SF), when irradiated with dose d, as (Fowler, 1989)

$$\epsilon = -\log(\mathrm{SF}) = \alpha d + \beta d^2 \,. \tag{3.6}$$

Hereby α and β are the ion-specific radio sensitivity parameters calculated from RBE models. In this work the carbon RBE was calculated using the local effect model (LEM1) (Scholz et al., 1997), provided within the carbon kernels set.

The helium RBE was calculated using a data driven quadratic-exponential parametrization based on LET (Mairani et al., 2016). In this model the radio sensitivity parameter of helium α_{He} is calculated using the photon radio sensitivity parameters (α_γ, β_γ) as

$$\alpha_{He} = \alpha_\gamma \left(1 + \left(k_0 + \frac{\beta_\gamma}{\alpha_\gamma}\right)\left(k_1 \mathrm{LET}^2 \exp\left(-k_2 \mathrm{LET}\right)\right)\right) , \tag{3.7}$$

with $k_0 = 1.36938 \times 10^{-1}$, $k_1 = 9.73154 \times 10^{-3}$, $k_2 = 1.51998 \times 10^{-2}$. The radio sensitivity parameter is given by $\beta_{He} = 1$. The parameters α_γ and β_γ are defined for each VOI during treatment planning.

This helium RBE model allows for a more lightweight representation of the helium data, as no additional precomputed pencil-beam kernels or spectra are needed to model RBE, which is sufficient in light of the expected small helium contribution.

The total combined radio sensitivity parameters α and β are calculated from the dose averaged α and β values of the carbon (C) and helium (He) irradiation (Zaider et al., 1980). The combined α_i and β_i of voxel i for a helium fraction of r is given by (Wilkens et al., 2006)

$$\alpha_i = \frac{\sum_j \left(\alpha_{ij}^C D_{ij}^C + \alpha_{ij}^{He} D_{ij}^{He} r\right) w_j}{\sum_j \left(D_{ij}^C + D_{ij}^{He} r\right) w_j}, \quad \sqrt{\beta_i} = \frac{\sum_j \left(\sqrt{\beta_{ij}^C} D_{ij}^C + \sqrt{\beta_{ij}^{He}} D_{ij}^{He} r\right) w_j}{\sum_j \left(D_{ij}^C + D_{ij}^{He} r\right) w_j} , \tag{3.8}$$

where α_{ij}^C and β_{ij}^C the LQ model parameter contribution in voxel i from carbon pencil beam j, with analogous parameters for helium. The combined effect to voxel i is given by

$$\epsilon_i = \alpha_i \sum_j \left(D_{ij}^C + D_{ij}^{He} r\right) w_j + \beta_i \left(\sum_j \left(D_{ij}^C + D_{ij}^{He} r\right) w_j\right)^2 . \tag{3.9}$$

Substituting eq. (3.8) in eq. (3.9) and using $A_{ij}^C = \alpha_{ij}^C D_{ij}^C$, $B_{ij}^C = \sqrt{\beta_{ij}^C} D_{ij}^C$ with the equivalent for helium the previous equation becomes

$$\epsilon_i = \sum_j \left(A_{ij}^C + rA_{ij}^{He}\right) w_j + \left(\sum_j \left(B_{ij}^C + rB_{ij}^{He}\right) w_j\right)^2 . \tag{3.10}$$

The matrices A_{ij}^C, A_{ij}^{He}, B_{ij}^C and B_{ij}^{He} can be precomputed for a given setup. Computing the dose influence matrix for a mixed beam is expected to be memory-intensive, particularly due to the additional calculations required for the A and B influence matrices.

3.2.2. Investigation of the Helium Range

As seen in fig. 2.1 helium ions have approximately three times the range of carbon ions at the same energy per nucleon. Thus, the helium energy and correspondingly their range in a mixed carbon-helium beam is determined by the primary carbon energies used for treatment. Depending on the location of the tumor and the treatment angle it is thus possible that the helium range is not sufficient for the helium ions to exit the patient distally.

Investigated Patient Cases

The residual helium range is investigated for three different tumor sites and multiple patients and beam angles. For each treatment angle matRad's stf struct, i.e the necessary carbon-energies and spot positions, was calculated. Then, for these the residual helium range distal of the patient was approximated using ray tracing (Siddon, 1985) through the entire CT image. This investigation focuses on the patient: however, the CT image may also include the patient couch. When the couch is located distal to the patient, any material outside the patient was assigned as air. In contrast, when the couch is proximal to the patient, such as with a 180° beam angle, this adjustment was not made, as it would lead to a wrong residual helium range.

The investigated patient cases were as follows: A prostate patient (fig. 3.9, Craft et al., 2014) with beam angles of 45, 90, 270, 315° and a liver patient (fig. 3.8, Craft et al., 2014) with angles of 0, 270, 315°. Furthermore 15 lung cases (Hugo et al., 2016) were investigated. Depending if the tumor was in the right or left lung the investigated angles were 0, 45, 90, 135, 180° or 0, 315, 270, 225, 180°, respectively. This data set includes in total 20 patients however not all provided the planning CT. The used patient IDs were: 102, 103, 104, 105, 108, 109, 110, 111, 112, 114, 115, 116, 117, 118 and 119. A subset of patients in this data set provided weekly follow up CTs. The provided CTs were 4DCTs, however only the first of 10 phases was used for the residual helium range analysis to focus on different patient anatomy, tumor sizes and tumor locations instead of different breathing phases. Of the investigated lung patients, 11 patients had a tumor in the right lung lobe and 4 in the left. The tumor volume ranged from 7 mL for patient No.115, to 312 mL for patient No.109. A similar investigation is presented in Hardt et al. (2025).

3.2.3. Strategies to Optimize the Residual Helium Range

To allow for a broader application to more patient cases, several strategies were developed and investigated to address the issue of potentially insufficient helium range. The main goal of these strategies is to ensure sufficient helium range and target coverage, additional aims are detectability of the beam distal of the patient. For the latter, the sensitive detection range of the used imaging detector has to be considered, as helium ions with higher residual energy or range can not be detected. An overview of the strategies is shown in fig. 3.2. All strategies will be discussed in detail below and are also presented in Hardt et al. (2025).

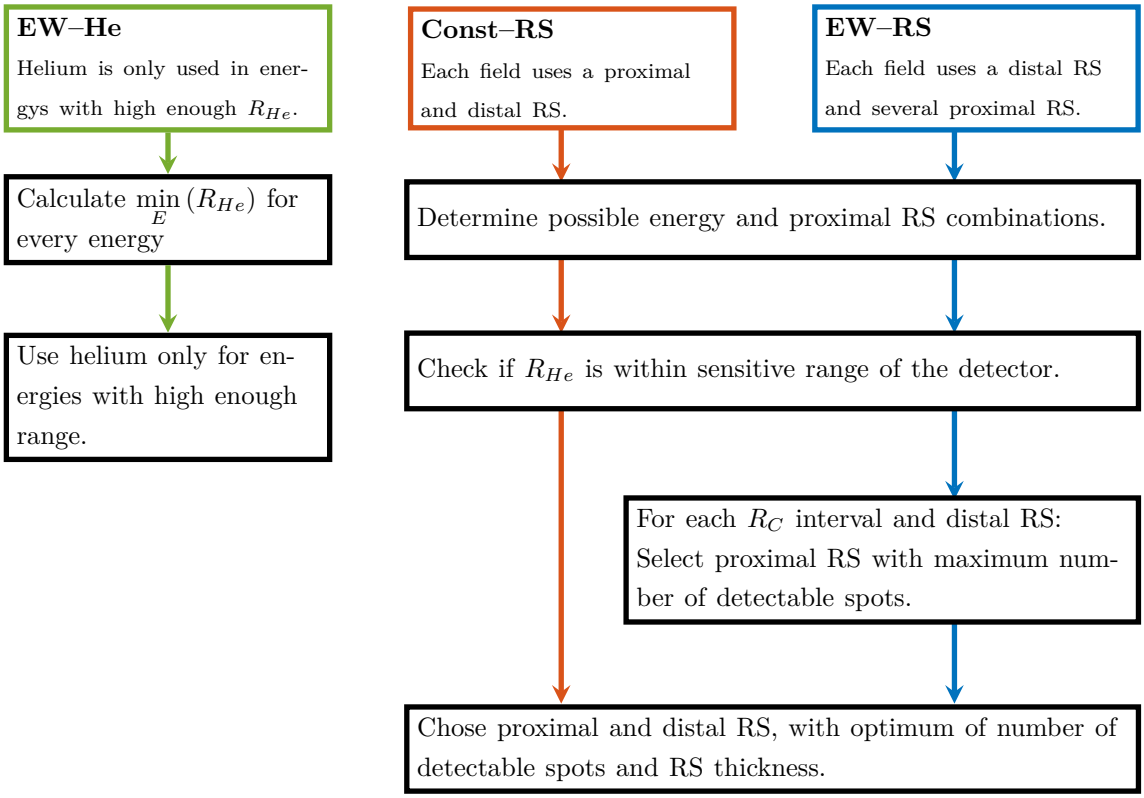

Figure 3.2.: Owerview of the developed helium range strategies aiming to address the issue of insufficient helium range. The strategies are EW–He, where helium is only added to the carbon beam in specific energys, Const–RS and EW–RS both utilize range shifters (RS) to increase the carbon and thus helium energy and range necessary for treatment.

Selection of Energies for Mixed Beam Irradiation (EW–He)

The EW–He strategy involves splitting up the irradiation into two parts, an irradiation with a mixed carbon-helium beam and an irradiation with a pure carbon beam. After determining the energies needed to irradiate the tumor. Ray tracing is performed to calculate the total WEPL of the patient (WEPL^{PO}). With the initial helium range for the initial energy (E_0) known the expected residual helium range after the patient can be calculated by subtracting this from the patient's WEPL: $R_{He}(E_0) - \text{WEPL}^{\text{PO}}$.

If the minimum expected helium range of an energy is below a threshold range ($R^{\min}$) the entire IES is marked to be irradiated with a pure carbon-beam.

Selection of Range Shifters (Const–RS, EW–RS)

The range of the carbon spot needs to be at least 1/3 of the minimum helium range required for the helium ions to distally exit the patient. To ensure that the all carbon spots in the target have a large enough WET, a proximal range shifter can be used to adjust the proximal material budget. A RS is a uniform slab of material that is already used in ion therapy to irradiate shallow tumors in order to degrade the beam (Gillin et al., 2010).

Since not every helium energy can be measured by the used imaging detector, a distal RS was considered. The distal RS is placed between patient and detector and it's purpose is to reduce the helium energy such that it complies with the sensitive range of the detector.

Several discrete options of the WET thickness of the proximal RS ($O_P = 0, 0.5, 1.5, 2.5, 3.5, 4.5\,\text{cm}$) and distal RS ($O_D = 0, 1, 2, 3, 4, 5, 6, 7, 8, 9, 10, 11, 12, 13, 14, 15\,\text{cm}$) were considered. The proximal range shifter thicknesses are chosen to be consistent with RS already used in clinics, Wang et al. (2023) uses range shifters with a thicknesses of up to 4.12 cm. For each energy (E) and spot position in the treatment plan it is calculated witch energy and proximal RS (x^P) combination is possible. A combination is possible if the carbon range (R_C) places the peak within the tumor and the helium range (R_{He}) is larger than the WET of the patient and the proximal RS. Accordingly it is calculated,

$$\mathcal{A}(x^P, E) = \begin{cases} 1, & \text{if } \mathrm{WEPL}^{\mathrm{TI}} \leq R_C(E) - x^P \leq \mathrm{WEPL}^{\mathrm{TO}} \\ & \quad \text{and } R_{He}(E) - \mathrm{WEPL}^{\mathrm{PO}} - x^P \geq R^{\min} \\ 0, & \text{otherwise}\,, \end{cases} \tag{3.11}$$

whereby $R^{\min}$ is the minimum allowed residual helium range, $\mathrm{WEPL}^{\mathrm{TI}}$ and $\mathrm{WEPL}^{\mathrm{TO}}$ is the passed through WEPL at the proximal and distal edge of the tumor.

For each energy, proximal RS and distal RS combination the expected range at the detector is calculated and if it lies within the sensitive energy/range interval $[R^{\mathrm{minD}}, R^{\mathrm{maxD}}]$ measurable by the detector used,

$$\mathcal{D}(x^P, x^D, E) = \begin{cases} 1, & \text{if } R^{\mathrm{minD}} \leq R_{He}(E) - \mathrm{WEPL}^{\mathrm{D}} - x^P - x^D \leq R^{\mathrm{maxD}} \\ 0, & \text{otherwise}\,. \end{cases} \tag{3.12}$$

$\mathrm{WEPL}^{\mathrm{D}}$ is the passed through WEPL at the entrance of the detector, this does not include the WEPL of the RS. Contrary to $\mathrm{WEPL}^{\mathrm{PO}}$, $\mathrm{WEPL}^{\mathrm{D}}$ includes the WEPL of the patient couch.

Two different types of RS strategies are investigated: Const–RS and EW–RS. Const–RS

uses one proximal RS and one distal RS during delivery of the treatment field. EW–RS allows for an additional degree of freedom, the proximal RS thickness. In this strategy several proximal RSs are used depending on the used energy. During irradiation, the RS could be coupled to the beam delivery nozzle and automatically changed during irradiation, whereby first all energys using a specific RS are irradiated. Next, the RS is changed and the next set of energys is irradiated. The distal RS thickness does not change during irradiation of the field. This represents an expected setup relying on manual placement of the distal RS, where it would be cumbersome to switch RSs multiple times during irradiation

Const–RS: When determining the optimal proximal and distal RS thickness for each treatment field, the aim is to maximize the number of detectable spots while minimizing the total thickness of the applied RS. Hence the weighted sum, describing the number of detectable spot and RS thickness, is optimized:

$$[x^{P\star}, x^{D\star}] = \underset{\substack{x^P \in O^P \\ x^D \in O^D}}{\operatorname{argmax}} \left(\frac{1}{n_1} \left(\sum_{s \in \mathcal{F}} \mathcal{D}(x^P, x^D, E_s) \right) - \frac{w}{n_2} \left(x^P + x^D \right) \right) . \tag{3.13}$$

The sum is performed over all spots s belonging to the treatment field $\mathcal{F}$. The optimal proximal thickness is $x^{P\star}$, the optimal distal $x^{D\star}$. The parameter w is an additional relative weighting of the number of detectable spots to the thickness of the used RS. The factors n_1 and n_2 normalize both parts of the expression to have equal magnitude

$$n_1 = \max_{\substack{x^P \in O^P \\ x^D \in O^D}} \left(\sum_{s \in \mathcal{F}} \mathcal{D}(x^P, x^D, E_s) \right) \tag{3.14}$$

$$n_2 = \max_{\substack{x^P \in O^P \\ x^D \in O^D}} \left(x^P + x^D \right) \tag{3.15}$$

EW–RS: The additional degree of freedom in the proximal RS thickness comes with an additional degree of complexity. Approximately the same depth in the patient can be reached with several combinations of energy and proximal RS. One can either use a high energy with a thick RS or a low energy with a thin RS to reach a certain depth. To ensure that every depth of the tumor is properly irradiated, all available energy and proximal RS options are grouped in intervals (I_i) of approximately the same depth in the patient ($R_C(E) - x^P$). The width of the interval is the chosen longitudinal spot spacing (l) of the treatment plan. The interval I_i is given as

$$I_i = [\min(R_C(E) - x^P) + il, \min(R_C(E) - x^P) + (i+1)l] \quad i = 0, 1, \ldots, N , \tag{3.16}$$

whereby the last interval I_N includes the most distal carbon range position

$(\max(R_C(E) - x^P))$. The selection of the proximal and distal RS is a two step process. First for each depth interval (I_i) and distal RS option, the proximal RS and energy option $([x_{iD}^{P\star}, E_{iD}^{\star}])$ which maximizes the number of detectable spots is chosen.

$$[x_{iD}^{P\star}, E_{iD}^{\star}] = \underset{x^P \in O^P}{\operatorname{argmax}} \left(\sum_{s \in I_i} \mathcal{D}(x_s^P, x^D, E_s) \right) . \tag{3.17}$$

The number of detectable spots for this range interval (I_i) with optimized settings, is $\mathcal{D}_{iD}$. This first step ensures that each depth intervall of the tumor is irradiated.

In a second step, to determine which distal RS with corresponding proximal RS's and beam energies should be used, the total number of all detectable spots and the total thickness of the used RS thickness is calculated, for each distal RS option and optimized similar as in eq. (3.13):

$$x^{D\star} = \underset{x^D \in O^D}{\operatorname{argmax}} \left(\frac{1}{n_1} \left(\sum_{i=0}^{N} \mathcal{D}_{iD} \right) - \frac{w}{n_2} \left(\sum_{i=0}^{N} x_{iD}^{P\star} + x^D \right) \right) , \tag{3.18}$$

whereby the normalization is given as

$$n_1 = \max_{x^D \in O^D} \left(\sum_{i=0}^{N} \mathcal{D}_{iD} \right) , \tag{3.19}$$

$$n_2 = \max_{x^D \in O^D} \left(\sum_{i=0}^{N} x_{iD}^{P\star} + x^D \right) . \tag{3.20}$$

Parameters: The minimum helium range was set to $R^{\text{min}} = 10\,\text{mm}$. The minimum detectable range in the detector was set to $R^{\text{minD}} = 7.5\,\text{mm}$. For the maximum detectable range two different settings were investigated a smaller one with $R^{\text{maxD}} = 110\,\text{mm}$, similar to the capability's of the ProtonVDA detector, and a larger one with $R^{\text{maxD}} = 160\,\text{mm}$. Furthermore the relative weighting w between number of detectable spots and RS thickness, see eq. (3.13), was set to $w = 0.5$, for lung cases. For the investigated abdominal cases, prostate and liver, this parameter was set to $w = 0.25$, favoring more number of detectable spots over thickness of the used RS. For the prostate case, the tumor is located approximately in the middle of the body and thus the residual helium range is expected to be higher requiring thicker distal RS.

Patient Study of the Residual Helium Range and the Developed Strategies

For the patient cases introduced in section 3.2.2 different residual helium range strategies were investigated, as well. The residual helium range strategies were applied for both detector settings. The number of detectable spots between all cases was compared to evaluate the benefit of each method.

Additionally treatment plans using all residual helium range strategies (EW–He, Const–

RS, EW–RS) were designed for an example patient. Comparisons were performed to a reference plan using no dedicated strategy to ensure adequate helium range. The example patient was chosen to be lung patient No.114. A beam angle of 90° was used. Further details on the treatment plan can be found in appendix A.2.

3.2.4. Analytical Dose Calculation with Range Shifters

The incorporation of RS, causes an additional widening of the beam. During analytical dose calculation this is taken into account by an additional component σ_{RS}, therefore eq. (2.20) becomes (Hong et al., 1996)

$$\sigma_{\mathrm{tot}}^2(z) = \sigma_{\mathrm{init}}^2 + \sigma_{\mathrm{RS}}^2 + \sigma^2(z)\,. \tag{3.21}$$

To obtain parameter σ_{RS}, MC simulations of a carbon and helium beam with energys of 88.83, 196.23, 272.77, 339.80, 427.44 MeV/u impinging on the RS were performed. The simulation set up followed the descriptions in section 3.2.1. RSs made of PMMA (Polymethylmethacrylat) with equivalent thicknesses of 5, 10, 15, 20, 25, 30, 35, 40, 45 mm where placed in front of the nozzle. The entrance dose was fitted with a Gaussian to extract the beam width. From the total beam width the initial beam width was subtracted to calculate the beam broadening due to the use of RS (σ_{RS}). A polynominal function was then fitted to estimate the beam broadening for intermediate energies. A similar investigation is presented in Hardt et al. (2025).

3.3. The Software Framework

3.3.1. Treatment Planning: matRad

In order to set up a treatment planning framework for mixed beam treatment planning and investigate possible use cases a consistent dose calculation and treatment planning system is needed. In this thesis the open source software matRad (Abbani et al., 2024; Wieser et al., 2017) was used. matRad is designed for research and educational purposes and provides algorithms for intensity-modulated photon, proton, heavy ion, and brachytherapy. Written in *MATLAB* (2024), it includes built-in algorithms for fast pencil beam dose calculation, 4D dose computation and interfaces with several MC codes: OmpMC[2] (Doerner et al., 2018), MCsquare (Souris et al., 2016; Souris et al., 2019), TOPAS (Perl et al., 2012; Faddegon et al., 2020) and on a research branch, Fred (Schiavi et al., 2017).

The most important variables in matRad are:

- `ct`: This structure contains the planning CT of the patient. Additional variables are the resolution and dimension.

[2] https://github.com/edoerner/ompMC,visited on 05/07/2025

- `cst`: This structure contains the segmentation of the VOI's of the planning CT as well as the objective function used in treatment plan optimization.
- `pln`: This structure contains meta information about the radiation treatment plan, such as the radiation mode and the irradiation angles. Parameters of the dose calculation and optimization can be set here.
- `stf`: This structure contains for each irradiation angle the steering information. That is the position and energy of each spot in the treatment plan.
- `dij`: This structure contains the dose influence matrix
- `resultGUI`: This structure contains the optimized fluence vector w as well as the optimized dose distributions.

matRad uses the LPS (Left, Posterior, Superior) coordinate system where the x-axis points towards the left patient-side, the y-axis towards the posterior direction and the z-axis towards the superior direction, additionally for ray tracing a beams eye view (BEV) coordinate system is used, whereby the y axis is directed along the beam.

3.3.2. Monte Carlo: TOPAS

The MC simulations within this thesis where performed with the MC tool: Tool for particle simulation (TOPAS) (Perl et al., 2012; Faddegon et al., 2020). TOPAS is a wrapper for the Geant4 simulation tool kit (Agostinelli et al., 2003; Allison et al., 2016) and recently turned open source with its OpenTOPAS branch, available on github[3]. Even though it is generally less computationally efficient than other MC tools, TOPAS is very flexible allowing for a high level of geometrical complexity and variety of particles. It also allows for the possibility to write customized scorers, physics list and geometry components which makes TOPAS especially useful as a general purpose MC code in radiation therapy research.

All MC simulations where performed with the following phyics lists: G4DecayPhysics, G4StoppingPhysics, G4EmExtraPhysics, G4EMStandardPhysics_option4, G4HadronElasticPhysics, g4h-phy_QGSP_BIC_HP and G4QMDReaction physics. To accurately model helium ions G4BinaryLightIonReaction was activated with the Tripathi cross section data (Tripathi et al., 1999) as modified by Horst et al. (2019). This thesis used TOPAS version 3.9.

3.3.3. The matRad-TOPAS Interface

The interface of matRad to TOPAS is very customizable, allowing the user to easily change parameters or add scorers and geometry components. Due to the speed of TOPAS it is

[3] https://github.com/OpenTOPAS/OpenTOPAS,visited on 05/07/2025

mainly meant to be used for forward dose calculation of treatment plans with an already optimized fluence. It is not meant to be used for calculation of a dose influence matrix.

The basic setup of the simulation is as follows: The simulation of a treatment field (`F`) iterates through the individual spots in the treatment plan. This is facilitated by the time feature system in TOPAS varying the beam source parameters throughout the simulation. These parameters for a simple beam model are the energy, energy spread, the mean position and mean direction along the ray, as well as the current. To calculate the current of each spot, the total number of histories is distributed among all spots in the treatment plan according to the weight given by the fluence vector. During this thesis the emittance parametrization of the beam was used, which also requires the position and angular divergence spread as well as their correlation. If these beam parameters are not already saved in the pencil-beam kernel set they are estimated, as presented in section 2.4.1. The simulation of each treatment field can be split up in multiple batches, or "runs" (`R`), with different initial seeds to estimate statistical uncertainty.

The input file of the simulation is split into several files for readability. For each irradiation field (`F`) and run (`R`):

- `beamSetup_fieldF.txt`: Contains field specific parameters, such as the basic geometry with source position and patient volume relative to the isocenter (gantry angle, couch angle rotation), the time sequence for simulation. For the latter, all source parameters and beam currents are provided for each time point.

- `matRad_plan_fieldF_runR.txt`: Stores all relevant configuration options for a single run for a field related to the desired output. As such, it contains scoring information and output file metadata, and imports the basic field parameter. This is the top-level parameter file passed to TOPAS to define a simulation.

- `matRad_cube.txt`: Parameterizes the Patient Volume and HU to Material / Density conversion.

- `matRad_cube.dat`: Contains the CT of the patient in HU.

- `MCparam.mat`: Is a MATLAB structure used for bookkeeping, such as the information necessary for a smooth read-in of the simulated data back into matRad.

The interface also allows for the addition of extra geometry components like range shifter's and range detectors to the simulation, as well as additional scorers. For this purpose, template files are used and loaded into the simulation when a specific geometry object or scorer is used.

To incorporate mixed beam planning, additional geometry components were added as template files to the MC simulation, which included the imaging detector, more on that later, and RS modeled as blocks of PMMA. At the beginning of the simulation all proximal

and distal RS that will be needed are created as geometrical objects. For the simulation of each treatment spot the position of the RS are updated so that only the one used during delivery of this spot is position in the beam path, while the other non used RS are positioned out of field.

During development a bug resulting in non-isotropic lateral scattering in TOPAS simulations of heavy ions was observed, seemingly one scattering direction was preferred[4]. This occurred when the ion beam was not directed along the z axis of the coordinate system used in TOPAS, as seen in fig. 3.3. This figure shows the longitudinally (along the beam axis) integrated dose of a TOPAS simulation of a proton (232.2 MeV/u), helium (232.2 MeV/u) and carbon (430.1 MeV/u) beam impinging on a water cylinder. Hereby the beam and cylinder were once oriented along the y axis and once along the z axis. This asymmetry was amplified when using RSs due to the increased scatter. To overcome this, the basic geometry of the TOPAS interface was updated. Initially the position of the patient was fixed and the particle beam was rotated around the patient, similar to the real world set up. This was updated, such that the beam is always directed along the z axis of the coordinate system and the patient is rotated into the correct angle of irradiation. This coordinate change also has the beneficial side effect that no coordinate transformation has to be performed between the simulation of the imaging detector and the reconstruction of the image data, as the same coordinate system is now used.

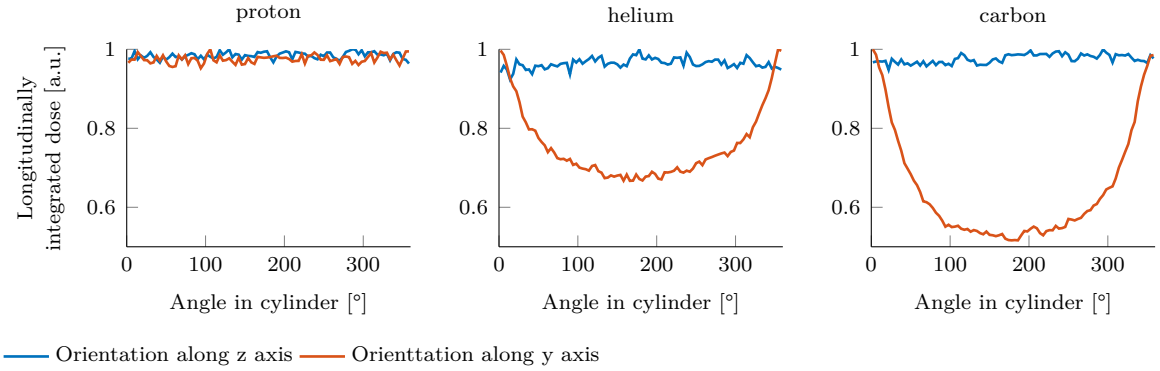

Figure 3.3.: Longitudinally integrated dose of a proton (232.2 MeV), helium (232.2 MeV/u) and carbon (430.1 MeV/u) beam for two orientations of the beam and the irradiated cylinder.

Moreover the matRad-TOPAS interface was updated to to facilitate direct 4D dose calculation within TOPAS, allowing for incorporation of intra fractional motion into the simulation. During the analytical 4D dose calculation, the CT phase of each spot is calculated. This calculation utilizes knowledge of the intensity of the beam to calculate the delivery time of one spot and the scanning speed to calculate the time needed for the beam to change positions from one spot to the next. Additionally the time needed for a synchrotron to accelerate the next spill and the total number of particles in a spill is used to calculate the irradiation time point of each spot. The used beam delivery parameters

[4] https://github.com/OpenTOPAS/OpenTOPAS/issues/99,visited on 05/07/2025

were as follows: A scanning speed of 6.8 m/s in x and y directions, a spill intensity of 8×10^7/s, a spill size of 4×10^8 carbon particles, a spill recharge time of 2 s and an energy switching time of 3 s are used(Ondreka et al., 2009). In the MC simulation the image cube representing the patient is changed in the simulation of every spot according to the current CT phase. Additionally, the dose scoring was revised to record the total dose delivered during each motion phase.

3.3.4. Implementation of the Mixed Carbon Helium Beam Framework

Dose Calculation and Treatment Planning

To ease the incorporation of the mixed beam treatment planning in matRad, mixed beam parameters were added to matRad `pln` struct. Figure 3.4 shows a code snippet illustrating the generation of the `pln` struct in matRad. In the top part, general parameters are defined, including the radiation mode, irradiation machine, beam angles, lateral spot spacing, iso-center position, the RBE model, selected scenarios, and the dose calculation resolution.

```
% Radiation Modality
plnCarbon.radiationMode          = 'carbon';
plnCarbon.machine                = 'HITfixedBL';
% Plan Parameters
plnCarbon.numOfFractions         = 30;
plnCarbon.propStf.gantryAngles   = [0];
plnCarbon.propStf.couchAngles    = [0];
plnCarbon.propStf.bixelWidth     = 5;
plnCarbon.propStf.numOfBeams     = numel(plnCarbon.propStf.gantryAngles);
plnCarbon.propStf.isoCenter      = ones(plnCarbon.propStf.numOfBeams,1) *
    matRad_getIsoCenter(cst,ct,0);
% Optimization Settings
plnCarbon.bioParam       =  matRad_BiologicalModel('carbon','RBExD', 'LEM');
plnCarbon.multScen       = matRad_NominalScenario(ct);
% Dose Calculation
plnCarbon.propDoseCalc.doseGrid.resolution      = ct.resolution;
% Mixed Beam Settings
plnCarbon.propMixedBeam.mixingRatio     = 0.1;
plnCarbon.propMixedBeam.useEWHe         = false;
plnCarbon.propStf.useRaShi              = true;
plnCarbon.propStf.isRaShiEW             = true;
```

Figure 3.4.: Code snippet for gernation of a mixed beam pln struct.

In the bottom section, the parameter `mixingRatio` defines the carbon-to-helium ion mixing ratio and activates the mixed beam concept during `stf` generation, in which the residual helium range strategies are considered. To apply the EW–He strategy, the parameter `useHe` must be enabled. If `useRaShi` is activated along with `mixingRatio`, the `stf` generator applies the Const–RS strategy described earlier. If no `mixingRatio` is provided, a conventional RS is used, added only when the machine's lowest energy is insufficient to reach the tumor. The parameter `isRaShiEW` is used to enable the EW–RS strategy.

Once the `stf` is generated, the corresponding helium `stf` and `pln` are also created. These are structurally identical to their carbon counterparts, differing only in radiation mode and biological dose model. Dedicated functions are available to combine the carbon and helium doses into a total mixed beam dose, as well as to merge their respective dose influence matrices.

Incorporation of Imaging Detector

Two different types of detectors were modeled: an idealized detector and the ProtonVDA detector. Figure 3.5 shows a code snippet of the generation of the `RangeDetector` class. This class handles parameters relevant for planning and reconstruction. For both the idealized and ProtonVDA detector use of either both trackers or only the front tracker can be chosen. In Figure 3.5 the used range detector setup is selected, in this case ProtonVDA without front tracker.

Next, the carbon `stf` is generated with a helper function. First the potential WET offset of the front trackers of the range detector is read into the `pln` struct to be considered in the generation of the `stf` and for dose calculation. Afterwards, a `stf` is generated while potentially using the presented helium range strategies.

Afterwards the optimal placement of the tracking planes is calculated, which depends on the chosen RS thickness. During therapy the placement of the detector is considered to be optimal when it is as close to the patient as possible. However, since in the MC simulations the entire CT of the patient is treated as one geometrical object, the detector is placed as close as possible to the CT cube to avoid overlap of the two geometrical components. Consequently, there is always some air between the patient and the detector, or a potential distal RS. The distal RS is placed immediately in front of the back tracker. The placement of the detectors is saved in the `pln` struct for easy access in the MC simulation and during image reconstruction.

```
RangeDetector = matRad_RangeDetectorVDAFL(ct,plnCarbon);
[stfCarbon, plnCarbon] = RangeDetector.generateMixedBeamStf(ct,cst,plnCarbon);
```

Figure 3.5.: Code snippet for generation of the range detector class and the stf.

The data collection for the simulated radiographs, both idealized and ProtonVDA detector, is based on scored phase spaces of primary helium ions in the respective planes of the front and back trackers. ”Scored phase spaces” refers to recorded data including the position, direction, energy and ID number of the helium ions. Since only primary helium ions are scored in these MC simulations, it is important to note that carbon and helium fragments are excluded. However, measurement data will include signals from these fragments, which degrade image quality. Therefore, a detector capable of filtering out such fragments is a crucial to reconstruct accurate image data

During image reconstruction the fitted helium energy-range relationship presented in section 4.2.1 is used for both detectors, to calculate the residual helium range and passed through WEPL from the scored energy. To incorporate the chosen sensitive detection region, data from helium ions with an energy below or above the detection limits is excluded from further evaluation.

Three different image types are distinguished:

- Full energy helium radiograph (FEHeRad): This reconstitution method uses data collected from all energies delivered in a field.
- Single energy helium radiograph (SEHeRad): This reconstruction method uses data collected from one energy, whereby the simulation ID, is used to filter the data.
- Spotwise: Here the simulation ID is used to calculate the mean and standard deviation of the WEPL of each spot, whereby no statistical cuts are applied. This method could be applied to measured data by grouping the data into spots based on the recorded acquisition time.

This framework for incorporation of the Range Detectors can easily be customized to implement other detector technologies.

Idealized Detector The idealized imaging detector has no material budget. A simplified reconstruction code, without statistical cuts and with a simpler path estimation, was implemented in matRad to be used with this detector. The path estimation is the cubic-spline-path as presented by Fekete et al. (2015). This detector allows for a full MATLAB implementation that is independent of the ProtonVDA code. After simulation the radiographs can be reconstructed by passing the location of the simulation files to the `RangeDetector` class.

ProtonVDA Detector The ProtonVDA detector is integrated into the simulation by modeling the geometry and materials of each component within the tracker planes. On the surface of the tracker planes the respective phase spaces files of the primary helium ions are scored. During creation of the treatment plan the user can choose if the front tracker should be used or not. For simulations without front tracker the same set up is used but the material of the components within the front tracker is automatically replaced with air. This ensures that the simulated front tracker does not interfere with the particles, while still allowing its scored data to be used for reconstruction with a virtual front tracker if desired, which can be useful for comparative studies of double and single sided setups.

The reconstruction code is written in C++ and provided by ProtonVDA. It was updated to align with the simulations. This included general adaptation to incorporate helium ions, for this purpose an additional integer variable (A), representing the mass

number of the particle was added. This allows to distinguish between proton and helium ions in the calculation of the scattering moments (section 2.1.1) and the residual range. Furthermore the data read in had to be updated to align with the output format of the MC simulations, specifically the used range shifters, beam position, beam spread, initial energy, current and the distance of the nozzle to the iso-center was read in from the `beamSetup_fieldF.txt`, for every field `F`. For reconstruction of the simulated radiographs the MLP algorithm, presented in section 2.3.2, was adapted with the formalism described by Krah et al. (2018) for single sided imaging. This algorithm requires the expected beam spread and beam divergence at iso-center, which was calculated from the read in values of the `beamSetup_fieldF.txt` file. Additionally the mean initial energy provided by the `beamSetup_fieldF.txt` was used to calculate the initial range. Moreover, the used RS thickness was subtracted from the WEPL of each particle, leaving only the corresponding WEPL of the patient. The reconstruction of SEHeRad was carried out by filtering the data according to the simulation ID. Similarly, the data was filtered for the Spotwise reconstruction, after which the mean and standard deviation was calculated. The simulation in this thesis were performed with the front tracker less version of the ProtonVDA detector.

3.3.5. Validation of a Mixed Carbon-Helium Treatment Plan

For an initial proof-of-concept, a simple phantom geometry for mixed-beam irradiation was designed. This phantom is displayed in fig. 3.7. It consist of a water box with a cubid target inside. A region of higher density material is inserted to provide image contrast in the radiographs. During creation of the treatment plan no range shifters were used. To compare impact of the helium contribution, two treatment plan optimization strategies were devised: The first one optimizes the total carbon-helium RBE weighted dose to 2 Gy per fraction, with 30 fractions, the second one optimizes the carbon RBE weighted dose to 2 Gy per fraction, with 30 fractions. The corresponding helium and carbon-helium dose was calculated in a second step. Next to the standard setting of the helium fluence (10 %) the contribution of the helium dose to the total dose was calculated for different values of the helium fluence (10, 20, 30, 40, 50, 60, 70, 80, 90, 100 %). This methodology is also described in and similar to Hardt et al. (2024).

The resulting treatment plans were re-simulated in TOPAS and the resulting HeRads were reconstructed using a single tracker and both trackers. During this thesis the Schneider et al. (2000) material converter implemented by TOPAS was used to convert the HU unit values of the CT into materials used in the simulation, it assigns materials with different elemental composition and density to the voxels of the image cube depending on their HU value. With an extension to TOPAS [5] the HU to RSP conversion for this

[5] https://github.com/topasmc/extensions/tree/master/HU,visited on 05/07/2025

Schneider conversion was extracted for 200 MeV protons. A digital reconstructed radiograph (DRR) was calculated using the housfield look-up table (HLUT) provided within matRad and extracted from the TOPAS simulation. More information on the treatment plan is listed in appendix A.2.

3.4. Online Treatment Verification

3.4.1. Verification of Patient Position

Accurate positioning of the patient is of great importance in radiotherapy, as a small deviation of position can cause significant dose changes (Lomax, 2008). As also presented in Hardt et al. (2024), the potential use of the mixed beam method for verification of the patient position is investigated. Ideally this way a change in the position of the patient between initial positioning and the treatment or during the treatment can be detected.

A method is presented to reconstruct the patient's position by comparing simulated HeRads from the current treatment fraction, where the patient's position is unknown—with reference images generated from the planning CT. These reference images are digital reconstructed radiographs (DRRs) along the beam direction for 225 different error scenarios on a $[-6.75\,\mathrm{mm}, 6.75\,\mathrm{mm}]$ grid in x BEV and z BEV direction. The HeRad of the unknown position scenario is compared to these reference images, whereby a mask is applied to filter out the noisy outer edge of the image.

The comparison metrics used are the mean squared error (MSE) and the structural similarity index measure (SSIM). The SSIM of two images I_x and I_y is defined as,

$$\mathrm{SSIM}(I_x, I_y) = \frac{(2\mu_x\mu_y + C_1)\,(2\sigma_{xy} + C_2)}{\left(\mu_x^2 + \mu_y^2 + C_1\right)\left(\sigma_x^2 + \sigma_y^2 + C_2\right)} \tag{3.22}$$

Hereby μ and σ are the mean and standard deviation of the corresponding image. The parameter σ_{xy} is the correlation of the images. C_1 and C_2 are custom constants added to ensure stability if $\mu_x^2 + \mu_y^2$ or $\sigma_x^2 + \sigma_y^2$ is close to 0. The SSIM metric is based on the computation of the luminance, contrast and structure of the images (Wang et al., 2004) and was used by Deng et al. (2023) and Dida et al. (2022) in the registration of images. Since a higher SSIM index indicates a higher similarity the negative SSIM is evaluated using the ssim function from MATLAB.

The image comparison metric is calculated for each reference image. A two-dimensional five degree polynomial is fitted to the comparison metric values and the position of the reference images. The minimum of this polynomial is calculated using the fminsearch function from MATLAB with starting point $[0, 0]$. The found minimum is the estimated patient position for that field. The estimated patient position for each field in the treatment plan is calculated, as well as the mean estimated patient position from all fields

which is the estimated patient position relative to the iso-center.

Investigation on a Prostate Case

The verification of patient position was investigated on a prostate patient, see fig. 3.9. In prostate cancer no significant onine movement or intra-fractional changes is expected. Consequently it is an adequate choice to verify the patient position.

A mixed beam treatment plan with two opposing beams (90°, 270°) was created. The residual helium range strategy was EW–RS, whereby the maximum sensitive range of the detection system was set to $R_{max} = 160\,\text{mm}$. Additionally the relative weight of the number of detectable spots to the total thickness of the range shifter was set to 0.25. More detailed information about the parameters used in the calculation of the treatment plan is summarized in appendix A.2.

Next to the nominal scenario with correct patient position, five random position error scenarios were sampled. The position error was modeled as a rigid, uncorrelated and normally distributed 3D translation of the planning CT, as suggested by Korevaar et al. (2019). Hereby a standard deviation of 2.25 mm in every direction was chosen. Helium radiographs were simulated for the nominal and the five sampled scenarios using 1×10^7 primary helium ions.

The dose was calculated for the nominal and the sampled position scenarios, additionally the dose was also calculated for the estimated patient positions and compared to the true patient position by evaluating the gamma pass rate eq. (2.31).

3.4.2. Verification under Inter and Intrafractional Changes

The methodology presented is similar to Hardt et al., 2024, where a different lung patient was used for evaluation. The methodology described in this thesis expands on Hardt et al., 2024 by adding the evaluation of inter-fractional changes based on multiple CTs obtained at different dates over the treatment course.

Investigation of Interfractional Changes

Rigid spatial shifts describing set-up uncertainties are not the only possible changes that can occur during the course of a treatment. The patient could loose weight, have fluid build up, the tumor could shrink – these anatomical changes result in a change of the patients WET that can be measured.

Interfractional changes were evaluated by comparing the helium radiograph of a later day, to the radiograph of the planning CT. Additionally, the dose was calculated and compared for both fractions. Of interest is how severe these interfractional changes are, also in comparison to intrafractional changes.

Verification of Intrafractional Motion

As explained in section 2.5.4, a strategy to minimize motion in lung cancer therapy is a ”breath-hold” technique where the patient is asked to hold her breath shortly during times of irradiation. It was investigated if this breath-hold can be verified with the help of a mixed carbon-helium beam. If the breath-hold can not be maintained, there will be a change in the motion phase during delivery of the IES, which corresponds to a change in the measured patient WET.

To isolate intrafractional changes and assess if the breath-hold was maintained without the influence of interfractional changes, data from the irradiation of two consecutive IESs can be compared. Comparing consecutive IESs is most effective, as they irradiate nearly the same cross-section of the tumor and therefore have the greatest spatial overlap. If both IESs are delivered during a stable breath-hold, the resulting HeRads should appear nearly identical, except for a noisy outer edge or regions where the IESs don't overlap. However, if the breath-hold is not maintained, differences between the HeRads will become apparent. Because an actively scanned beam is used, where each region of the image corresponds to a different irradiation time, the differences between the HeRads are expected to be localized to a specific region.

In addition to radiographs, the mean WEPL of a single spot can be analyzed. If both IESs are delivered during a stable breath-hold, their mean spotwise WEPL values are expected to be nearly identical. However, if the breath-hold is not maintained during one of the IESs, this will result in a noticeably greater difference after that time point. When comparing WEPL values of different IES, it is crucial to compare spots that correspond to the same ray, since as illustrated in fig. 2.6 spots of the same ray follow the same path through the patient and are thus expected to have the same WEPL. Next to the spotwise WEPL difference, also the total spotwise WEPL difference of the IES was evaluated and the correlation of the spotwise WEPL difference with time. A correlation with time is expected for the failed breath-hold scenarios, as a larger difference should be observed at later irradiation times, when the breath-hold failed.

A threshold of the mean spotwise WEPL difference of each spot was evaluated, as the difference of the mean spotwise WEPL could potentially be evaluated in real time during irradiation. If the observed WEPL difference of a spot exceeds a predefined threshold, the irradiation could be paused until the patient is in breath-hold again.

Correlation of Carbon and Helium Range Changes

Differences in the helium range will reflect changes in anatomy in the whole beam path traversed in the patient by the helium ions. This includes changes occurring distal to the tumor, which do not affect the carbon peak position and therefore do not significantly influence the delivered dose. The correlation of patient WET to carbon peak position,

was investigated by analytically calculating the difference in patient WET and difference in carbon peak position in the breath-hold and failed breath-hold scenario of an IES.

Investigation on a Lung Case

A mixed beam treatment plan for lung patient No.114 was calculated. This patient was selected because, in addition to the planning CT, the dataset also includes CT scans from different days this enables the investigation of interfractional changes. For this purpose, the CT scans were aligned using rigid registration in 3D Slicer (Fedorov et al., 2012). This allowed for the treatment plan, originally optimized on the planning CT, to be recalculated on a scan from a different day. The Day 1 CT was acquired three weeks after the initial planning CT (Day 0). Although 10 additional cone beam computed tomographys (CBCTs) scans were acquired in the interim, these CBCTs lacked the image quality necessary for treatment planning (Giacometti et al., 2020).

The mixed beam treatment plan was calculated using a beam angle of 0° and the EW–RS strategy. Additional planning parameters are provided in appendix A.2. Helium simulations of the treatment on Day 0 were simulated with 1×10^7 primarys. In addition, 12 of the 78 IES were simulated again with 1×10^6 primarys. The energys were selected to include two consecutive energies per proximal RS table 3.1.

x^P [cm]	Energy 1 [MeV/u]	Energy 2 [MeV/u]
45	222.31	218.52
35	223.56	221.05
25	221.05	218.52
15	214.70	210.83
5	218.52	214.70
0	232.20	229.76

Table 3.1.: Selected IES for evaluation of interfrational changes.

For these selected IES the simulation were also performed for Day 1 and in addition to the nominal breath-hold phase, Day 1 simulations were repeated with a simulated failed breath-hold scenario. This was modeled using 4D dose calculations, where a random time point during irradiation of the IES was sampled at which the breath-hold failed. After this point, the motion phase of the spot was assumed to change from the nominal motion phase (phase 0) to the subsequent motion phase (phase 1).

3.5. Overview of Investigated Patients and Phantoms

The following section provides an overview of the phantom and patient data used in this thesis. The Box Phantom with bone insert (fig. 3.7) was created using the phantom builder included in matRad. The Liver (fig. 3.8), Prostate (fig. 3.9) and Box Phantom

without bone insert (fig. 3.6) are also part of the matRad framework. The prostae and liver phantom originate from the CORT dataset (Craft et al., 2014).

Additionally, a publicly available lung dataset was used (Hugo et al., 2016), with an exemplary patient shown in fig. 3.10. This dataset provides phase-binned, respiration-correlated 4DCT scans with 10 motion phases. Phase 0 corresponds to the end of inspiration. As the dataset does not include a defined breathing period, a period of 5 s was assumed, resulting in a time resolution of 0.5 s per phase. A breathing period of 5 s corresponds to the average adult resting breathing period (Pleil et al., 2021).

While the dataset includes segmentations of several organs, the outer body contour was not segmented, which is required for analytical dose calculations. To address this, the body contour was generated by applying a threshold of −750 HU. This threshold excludes parts of the lung, hence MATLAB's imfill function was used to fill gaps in the segmentation. However, this method also resulted in parts of the patient couch being included in the body contour.

The dataset also includes a segmentation of the tumor, which was used as the planning target volume (PTV).

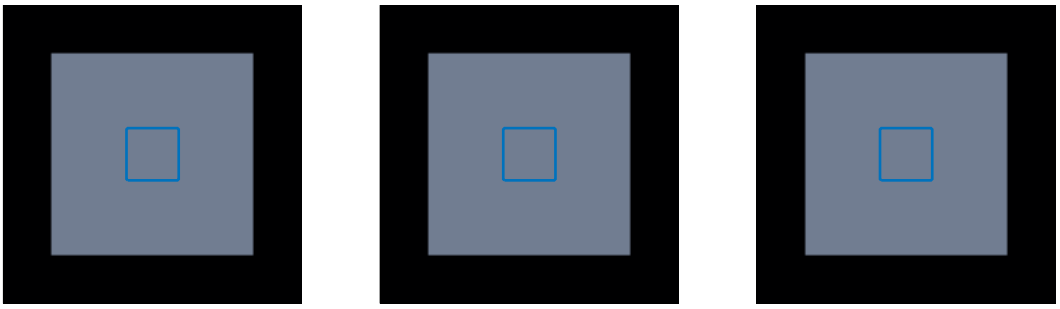

Figure 3.6.: Coronal (left), sagittal slice (center) and axial (right) slice through the isocenter of the box phantom. The segementation of the PTV (—) is drawn.

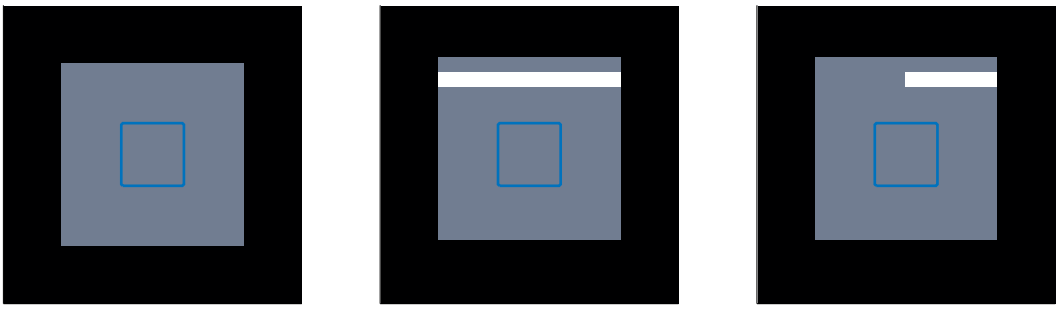

Figure 3.7.: Coronal (left), sagittal slice (center) and axial (right) slice through the isocenter of the box phantom. The segementation of the PTV (—) is drawn.

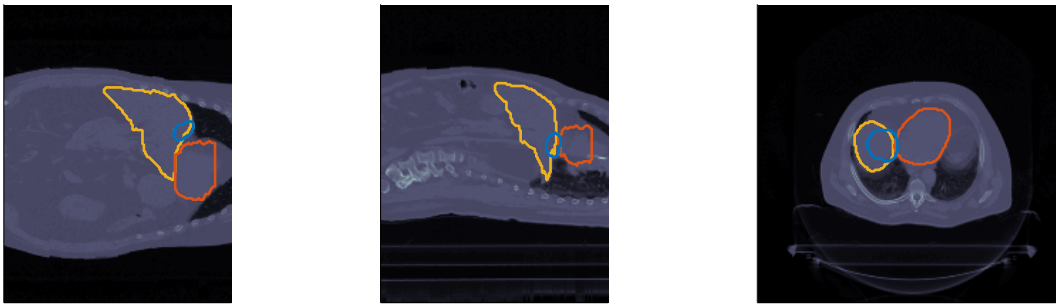

Figure 3.8.: Coronal (left), sagittal slice (center) and axial (right) slice through the isocenter of the liver patient. The segementations of PTV (—), liver (—) and heart (—) are drawn.

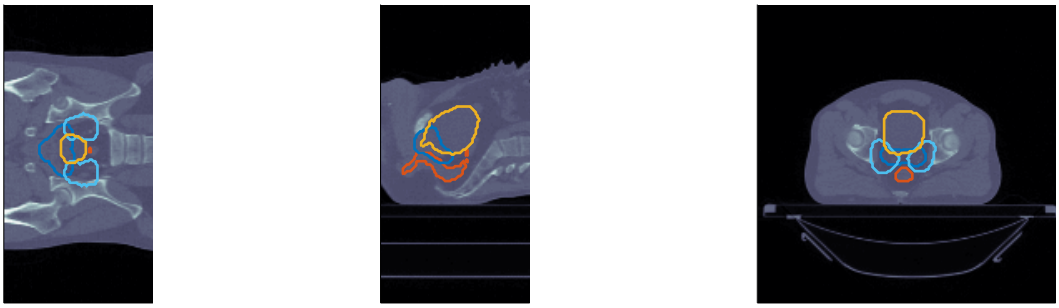

Figure 3.9.: Coronal (left), sagittal slice (center) and axial (right) slie through the isocenter of the prostate patient. The segementations of $PTV_{68\,Gy}$ (—), $PTV_{56\,Gy}$(—), bladder (—) and rectum (—) are drawn.

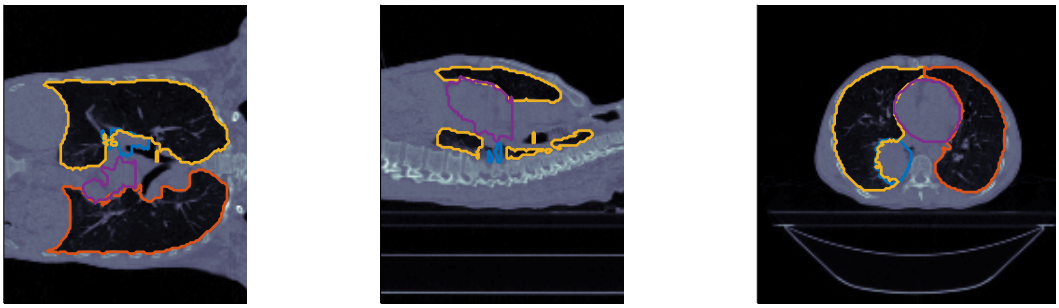

Figure 3.10.: Coronal (left), sagittal slice (center) and axial (right) slice through the isocenter of the lung patient (P114). The segementations of PTV (—), right lung (—), left lung (—) and heart (—) are drawn.

4

Results

4.1. Helium Radiograph Measurements

4.1.1. WET Verification Measurements

The ground truth WET values as well as those extracted from the measured and simulated radiograph and their relative error to the ground truth value is shown in table 4.1. The error of the ground truth represents the uncertainty in the length measurement of the insert or the PMMA cylinder. A photograph of the gammex phantom as well as the measured helium radiograph can be found in the appendix in fig. A.1. Both the measured and simulated WET values show satisfactory agreement with the reference value. The highest deviation for the simulation is for Muscle at 2.3 %. For the measured values the deviation of three materials, CB2-50 %, Solid Water and Muscle is 3 % or larger. The largest difference of simulated to measured WET values is 0.28 cm or 2.7 % for CB2-50 %.

ID	Material	WET [cm]			rel. Diff. [%]	
		GT	Meas.	Sim.	Meas.	Sim.
1	PMMA	11.56±0.01	11.76±0.14	11.79±0.03	−1.7	−1.9
2	CB2-30%	8.92±0.01	8.96±0.13	9.00±0.02	−0.4	−0.9
3	Liver	7.58±0.01	7.68±0.06	7.65±0.02	−1.3	−0.8
4	Brain	7.53±0.01	7.61±0.05	7.64±0.02	−1.0	−1.4
5	Inner Bone	7.61±0.01	7.71±0.06	7.66±0.02	−1.4	−0.8
6	CB2-50%	10.07±0.01	10.40±0.06	10.12±0.03	−3.3	−0.5
7	Solid Water	7.02±0.01	7.28±0.05	7.15±0.02	−3.8	−2.0
8	Muscle	7.23±0.01	7.45±0.06	7.40±0.02	−3.0	−2.3
9	Cortical Bone	11.41±0.01	11.44±0.06	11.46±0.02	−0.3	−0.5
10	B-200 Bone	7.74±0.01	7.80±0.06	7.77±0.02	−0.7	−0.3

Table 4.1.: WET values of the Gammex Phantom. The Ground Truth (GT) values were calculated. Measured (Meas.) and Simulated (Sim.) values are extracted from measured and simulated helium radiographs.

4.1.2. Phantom Measurement

The helium radiographs of the abdominal region of the anthropomorphic BRaViDA phantom are presented in fig. 4.1. In the radiograph acquired with helium ions at an energy of $E = 190\,\mathrm{MeV/u}$, $R = 24\,\mathrm{cm}$, the outline of the phantom, along with the spine and part of the sacrum, is clearly visible. On the right side of the phantom, however, the image appears very noisy due to detector saturation caused by high-energy helium ions that have not lost energy, as they did not pass through any material.

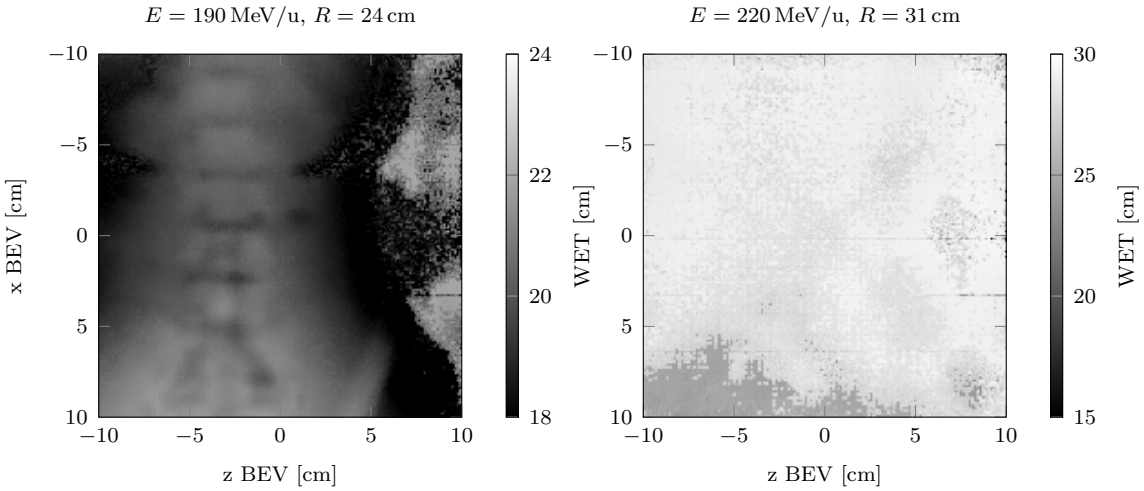

Figure 4.1.: Acquired helium radiographs of the abdominal region of the anthropomorphic BRaViDA phantom. Measurements were taken at $E = 190\,\mathrm{MeV/u}$, $R = 24\,\mathrm{cm}$ and $E = 220\,\mathrm{MeV/u}$, $R = 31\,\mathrm{cm}$.

The other radiograph ($E = 220\,\mathrm{MeV/u}$, $R = 31\,\mathrm{cm}$), shows the effect if an image is acquired with too high helium energy/range. The measured WET of the phantom is approximately 20 cm, resulting in a residual range of about 11 cm beyond the phantom. This is the detection limit of the detector, leading to saturation and loss of accuracy. In the lower left corner, where the phantom's WET is higher, some ions are still detected.

4.2. Characterization of the Helium Machine Data Kernel Set

The estimated energy spread for helium ions ranged from 4.0 % for the lowest energy to 0.2 % for the highest energy. During the MC simulation, deposited energy, was scored radially and in depth. Figure 4.2 shows the radially integrated depth dose curves for five different energies ranging from the lowest to the highest energy simulated energy of the helium machine kernel set. Lower dose in the plateau region is observed for higher energy and a smaller peak-to-plateau ratio.

The radial dose profiles were fitted with a weighted sum of three gaussian functions to extract the lateral dose profile, an example of these lateral fits is shown for different

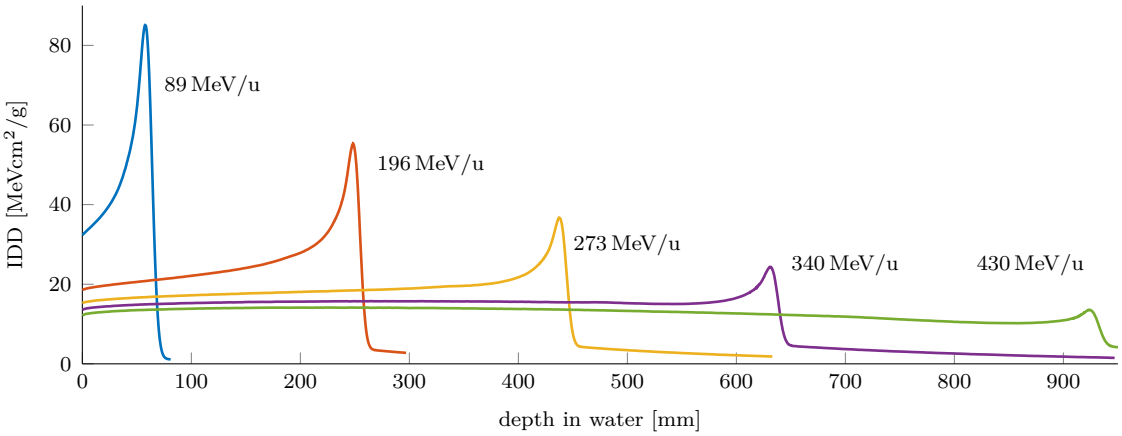

Figure 4.2.: Simulated depth dose curves of the helium kernel data set for 5 different energies. This data set was used for analytical dose calculation.

depths and energies in fig. A.3 and an example for the extracted fit parameters and LET in fig. A.4, these figures are located in the appendix.

For high energies it was observed that the laterally integrated entrance dose, was higher than the laterally integrated dose delivered at the Bragg-Peak. For the highest energy of 430.1 MeV/u with a range of 93 cm, a MC simulation that scored the fluence in depth showed that the expected loss of primary helium ions due to fragmentation is approximately 90 %. Thus too few helium ions remain to build up a characteristic Bragg-peak as seen for the lower energies. The Bragg-peak is still noticeable but contrary to the lower energys the laterally integrated dose curve does not have it's maximum here.

For high energies also significant lateral scattering was observed, the full width half maximum at the Bragg-peak is expected to be in the order of 2.5 cm (E=430.1 MeV/u). For comparison, for an intermediate energy of 196 MeV/u, with a range of 25 cm which is an energy that would be used in helium particle therapy, the full width half maximum at the Bragg-peak is approximately 1 cm. This kernel set was used for analytical dose calculation using the pencil beam algorithm presented in section 2.4.1.

4.2.1. Helium Energy Range Relationship

Figure 4.3 shows helium energy range relationship. For the MC simulations only every 10th data point is displayed. The measured data is taken from Berger et al. (2009). This measured data does not cover the full range of the helium energies used in this thesis. Unfortunately the used helium energies are somewhat unusual, as they are higher than the energies used for helium particle therapy and traditional helium imaging. For image reconstruction and in general to calculate the range, a energy range relation ship was fitted to the MC data, the result is also shown in fig. 4.3 and the fit parameters are displayed in table table 4.2.

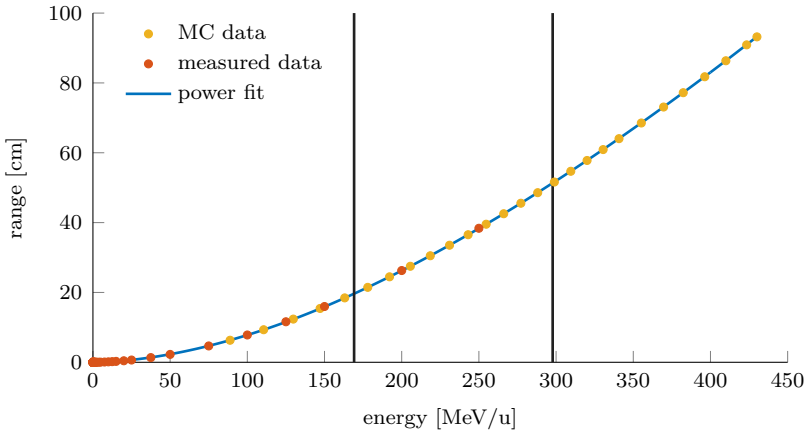

Figure 4.3.: Fitted range-energy relationship for helium ions. The fit was performed in three intervals using the simulated data. For better visibility the figure displays only every 10th data point of the simulation. Measurement data for comparison taken from Berger et al. (2009)

E [MeV/u]	α [(MeV/u)$^{1/p}$ · mm]	p	c [mm]
$E \leq 169.17$	0.02389	1.757	-
$169.17 < E < 297.79$	0.05517	1.61	−17.06
$E \geq 297.79$	0.1059	1.507	−53.12

Table 4.2.: Fitted parameters for the helium energy-range relationship, described in section 3.2.1

4.3. Validation of the Mixed Carbon-Helium Beam Framework

4.3.1. Impact of the Helium Contribution on Dose Calculation and Optimization

Figure 4.4 displays the carbon-helium and helium RBE weighted dose profiles as well as the DVHs for both optimization settings. Considering the carbon-helium depth dose profiles no significant difference can be observed between both optimization settings, for the lateral profile the optimization considering the total carbon-helium dose has a slightly wider penumbra. No significant difference can be observed in the carbon-helium DVH. The helium lateral profile for the carbon-helium dose optimization has a wider penumbra.

The combined carbon-helium dose influence matrix used approximately four times the memory of the carbon dose influence matrix, whereby the helium dose influence matrix consumes more memory than the carbon dose influence matrix. To optimize computational efficiency, dose influence matrices are only calculated in regions before the lateral dose falls below a predefined threshold. Since helium ions scatter more than carbon ions, this lateral cutoff is larger for helium. Additionally, because helium ions can pass through

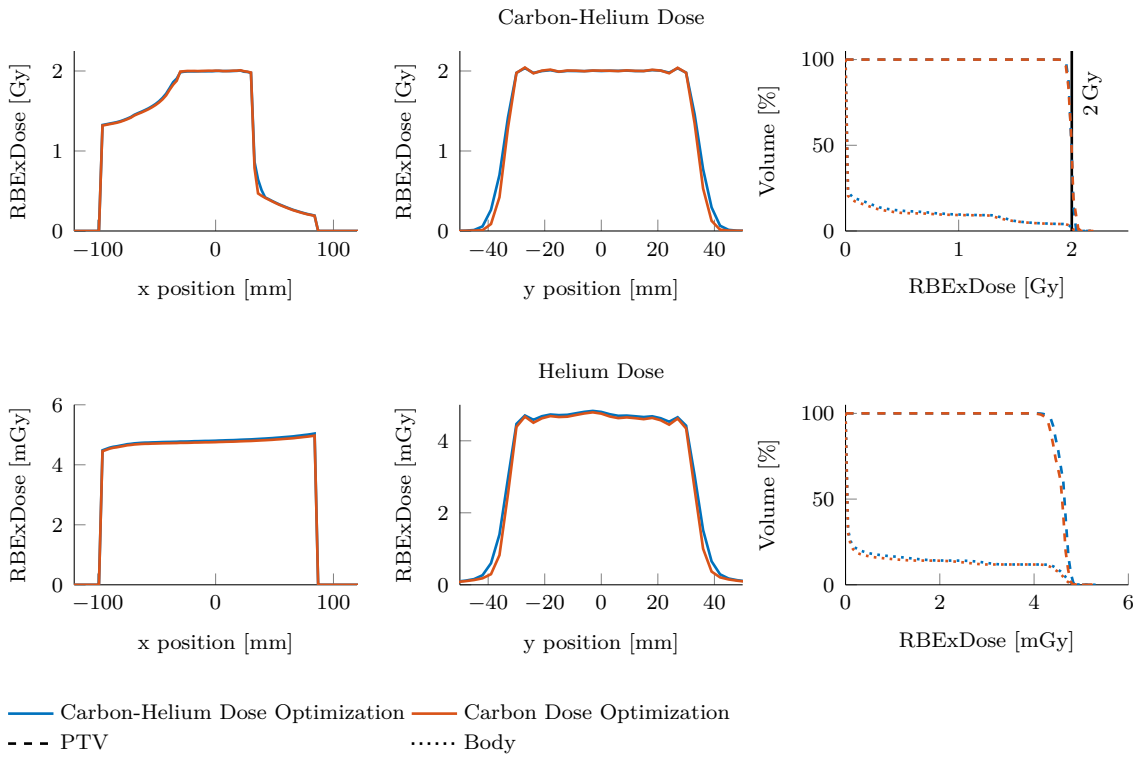

Figure 4.4.: Top Row: Depth and lateral profiles of the analytically calculated carbon-helium RBE weighted dose for the two optimization settings and the corresponding DVH. Bottom Row: Depth and lateral profiles of the helium RBE weighted dose for both optimization settings and the corresponding DVH. The prescribed dose of 2 Gy was annotated in the DVH

the entire patient, memory consumption increases further compared to the carbon dose influence matrix. For computational benefit, all other subsequent plans used the dose influence matrix of carbon ions only and the dose carbon RBE weighted dose was optimized with subsequent calculation of the helium RBE weighted dose and the carbon-helium RBE weighted dose.

The helium dose contributed little to the total delivered dose. Since the helium energy is higher and the helium range should ideally be high enough to exit the patient, the characteristic steep dose increase of the Bragg-Peak, as seen in fig. 2.2 cannot be observed. Instead, the helium dose is rather constant through out the patient. For the combined carbon-helium dose optimization, the integrated helium absorbed dose amounts to 1.4 % of the integrated carbon absorbed dose. The integrated helium contribution to the RBE weighted dose is lower with 0.4 %. In the target region, the helium RBE weighted dose is around 4.8 mGy whereas the carbon RBE weighted dose is around 2 Gy, therefore helium contributes 0.24 % of the carbon dose in the target region. This is also notably less than the carbon fragment tail in the patient, that can be seen as the dose falloff in the top left dose profile of fig. 4.4 at an x position of around 50 mm onward. In the carbon fragment tail the helium contribution is higher than in the target, at the distal edge of the patient the helium absorbed dose is 16 % of the carbon absorbed dose and the helium RBE weighted dose is 3 % of the carbon RBE weighted dose.

Impact of the Helium Fluence on the Delivered Dose

For the treatment plan optimized using the carbon RBE weighted dose, several helium contamination's were calculated (10, 20, 30, 40, 50, 60, 70, 80, 90, 100 %), as seen in table 4.3. The integral helium contribution relative to the carbon dose increases approximately linearly with the helium fluence. For a helium fluence of 30 %, the integral helium RBE weighted dose contributes 1 % of the integral carbon RBE weighted dose. For a helium fluence equal to the carbon fluence, the integral helium RBE weighted dose is 3.5 % of the integral carbon RBE weighted dose and the integral helium absorbed dose is 14 % of the integral carbon absorbed dose.

	Helium Fluence [%]									
	10	20	30	40	50	60	70	80	90	100
Absorbed Dose [%]	1.4	2.8	4.2	5.6	7.0	8.4	9.8	11.2	12.6	14.0
RBExDose [%]	0.3	0.7	1.0	1.4	1.7	2.1	2.4	2.8	3.1	3.5

Table 4.3.: Comparison of integrated helium to carbon doses, for helium fluences ranging from 10 % of the carbon fluence to 100 % of the carbon fluence.

4.3.2. Verification of the Monte-Carlo Simulation Pipeline

Figure 4.5 compares physical carbon and helium dose profiles for an analytical calculation and for the MC simulation. The treatment plan with combined carbon-helium dose optimization is considered here. It should be noted that matRad performs the analytical dose calculation only in voxels inside the patient as the pencil-beam algorithm does not require full transport of the ions. The MC simulation needs to transport particles through air explicitly, and thus the dose is reported in these regions as well, which is noticeable in fig. 4.5. As seen in fig. 4.5 the analytical and MC simulated dose profiles match well in the patient, except for the region of the high density insert at $x \approx -75\,\text{mm}$. These inconsistency in the insert are caused by the analytical dose calculation, by definition, reporting Dose-To-Water whereas the MC simulation calculates Dose-to-Material.

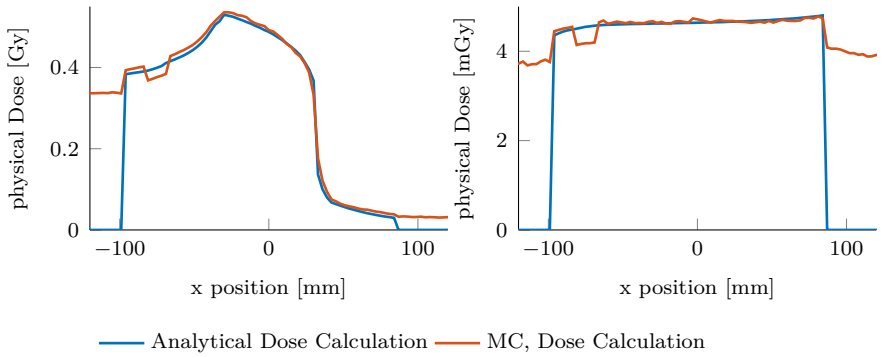

Figure 4.5.: Absorbed carbon (left) and helium (right) depth dose profiles for analytical dose calculation and MC simulation.

Figure 4.6 displays lateral line profiles through the DRR of the Box Phantom and of the reconstructed FEHeRads of the MC simulation, reconstructed using only data from the distal tracker and using data from both trackers. While in further evaluation only radiographs using the distal tracker were reconstructed the radiograph using both trackers is shown here for comparison.

As seen in the figure the WET values of the simulated radiographs are consistent with the DRR using the HLUT extracted from the TOPAS simulations. Between both DRRs there is a slight offset of $\sim 2\,\mathrm{mm}$ or $\sim 1.1\,\%$. The single sided radiograph has worse spatial resolution than the double sided setup. This is indicated by the sharper edge in the interface between both materials for the setup using both trackers. The function $f = a \cdot \mathrm{erf}(b \cdot x + c) + d$ was fitted with a non-linear least squares method of MATLAB to both profiles. The slope b for the reconstruction using only the back tracker was $b = 3.2\,\mathrm{cm}^{-1}$, whereas the slope for the radiograph using both trackers was $b = 9.5\,\mathrm{cm}^{-1}$.

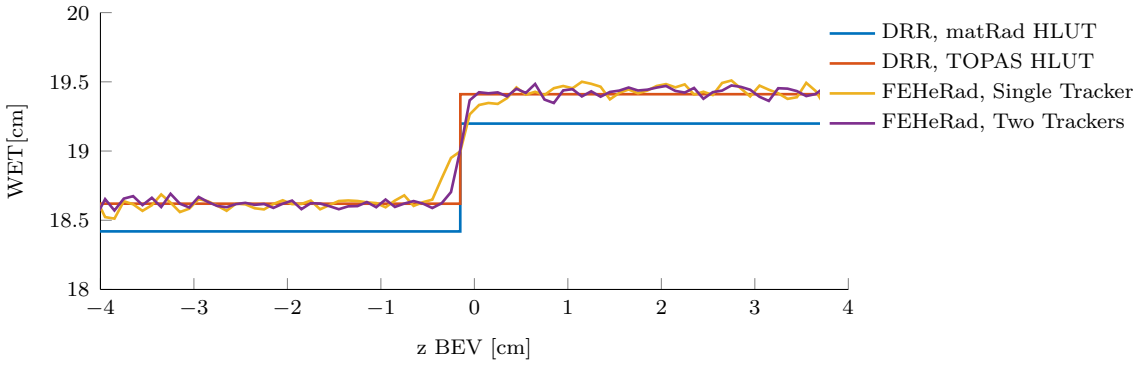

Figure 4.6.: Line plot of the DRR using the HLUT provided with in matRad, using the HLUT extracted from the TOPAS simulation and the FEHeRads of the Box Phantom, reconstructed using only the back tracker and reconstructed using both trackers.

4.3.3. Beam Widening Due to Range Shifters

Figure 4.7 shows the estimated beam widening due to the use of proximal RS for carbon and helium ions. For low helium energies this additional widening can become substantial (up to 20 mm). The combination of low helium energy and thick proximal range shifter is not very common. Normally a thicker range shifter will be used with a higher helium energy. The widening was calculated, not for all carbon energies and proximal RS combinations. For the lowest energy the used RS were sometimes thicker than the corresponding carbon range. This would also mean that these energys would not be used in a treatment plan, and thus it is nor necessary to calculate the helium widening in these cases, however this was done for completeness.

Figure 4.8 shows the absorbed carbon and helium dose profiles, calculated analytically and with MC simulations on a box phantom. Contrary to the results seen in fig. 4.5

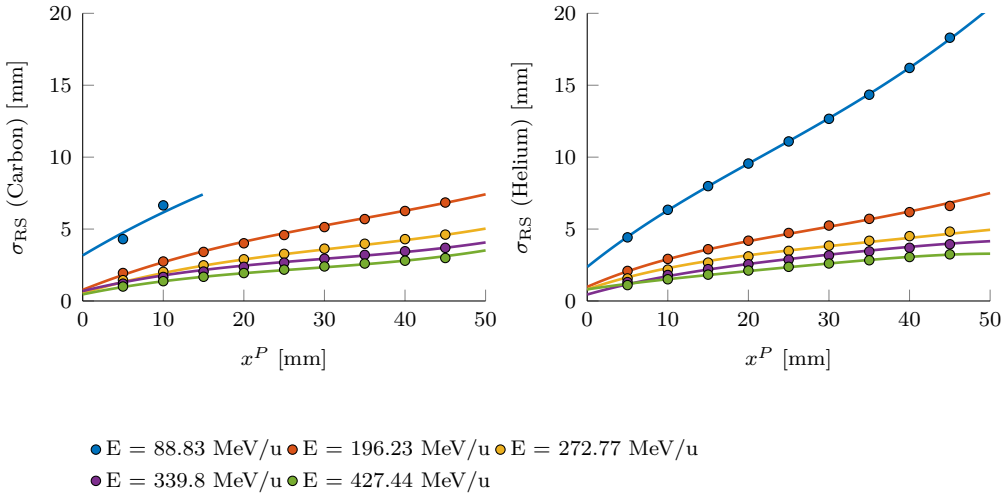

Figure 4.7.: Estimated (●) and fitted (—) beam widening due to the use of a proximal range shifter of varying thickness for carbon (left) and helium (right).

no high density insert was present in this phantom. A proximal RS of 45 mm thickness was added. The absorbed carbon dose shows good agreement between both methods. For helium ions, the analytical dose calculation overestimates the dose calculated with MC, which is related to the inaccuracies of the pencil-beam algorithm in modeling lateral scattering, especially in a wide beam. The proximal RS was positioned at the nozzle, leaving approximately 1 m of air between the RS and the patient, which is a significant distance that causes considerable scattering. For the energies used in this treatment plan, the estimated additional carbon beam widening caused by the range shifter ranges from 3.71 mm to 4.83 mm. For helium it ranges from 3.98 mm to 4.84 mm.

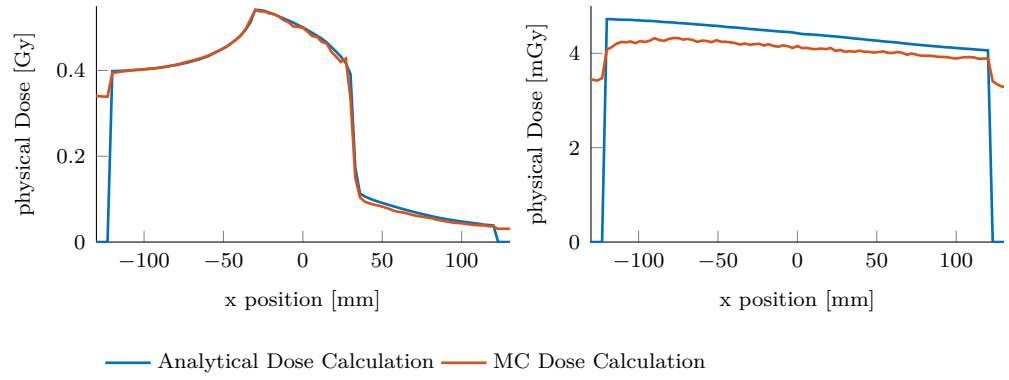

Figure 4.8.: Absorbed carbon (left) and helium (right) depth dose profiles, for irradiation of a water box, with a 45 mm proximal range shifter

4.4. Investigation of the Helium Range

This section presents the results of the investigation into viable helium ranges for mixed-beam treatments, for which the methodology was described in section 3.2.2 and section 3.2.3. Parts of the results are also described in Hardt et al. (2025).

4.4.1. Helium Range Analysis of Different Cancer Sites

Lung Cases

During investigation of the residual helium range, none of the previously mentioned strategys was applied. Figure 4.9 summarizes the minimum residual helium range for every investigated beam angle and patient case as well as the percentage of spots with a residual helium range smaller than 1 cm. This serves as an indication of the severity, determining whether only a small or large fraction of spots are identified with insufficient range. A negative value represents a spot where the helium range is to small and lies within the patient.

The opposing angles 0° and 180° seem well suited, for mixed beam irradiation without range shifters, since they combine a higher minimum residual helium range and lower percentage of too low spots. Whereby the 0° seems more suited to the 180° since it does not involve irradiating though the patient couch. Nevertheless still 9 of the investigated 15 patients had a minimum residual helium range smaller than the safety margin of 1 cm for this beam angle. For 6 of the investigated 15 cases none of the investigated angles had sufficient range. The most common available angle was 180° (8/15) followed by 0° and 135/225° (6/15).

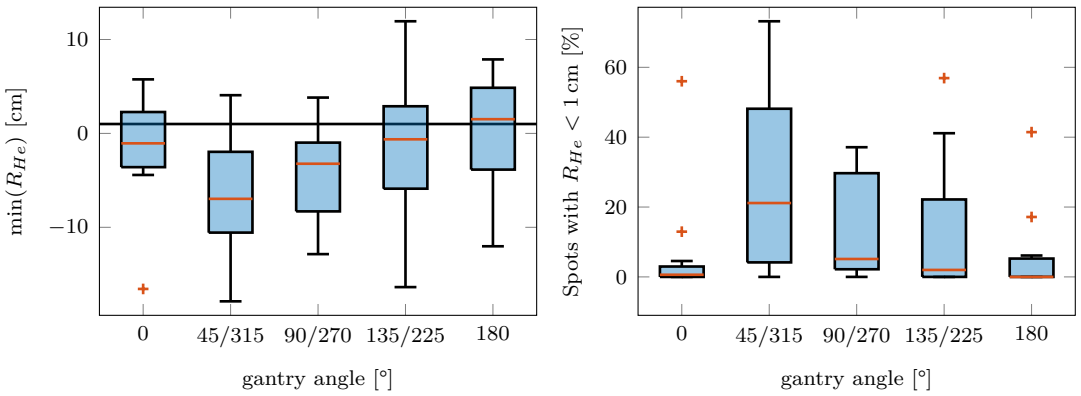

Figure 4.9.: Left: Box plot summarizing the minimum residual helium range of each lung patient for the different beam angles. A negative value represents a spot where the helium range is too small and lies within the patient. Right: Box plot summarizing the percentage of spots in each treatment plan with a residual helium range smaller than 1 cm for each beam angles

Figure 4.10 uses an exemplary lung patient (No. 114) to illustrate the distribution of spots with sufficient and not sufficient helium range. Again here the beam angle 0° and

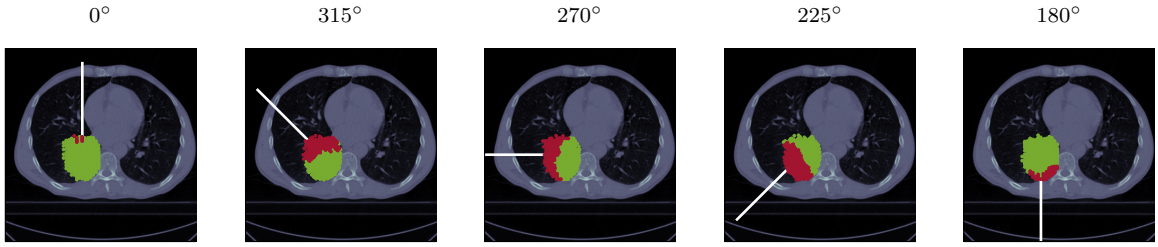

Figure 4.10.: Axial CT slice for patient No.114 with different beam angles. The overlay highlights the spots in green (●) with sufficiently large residual helium range and the ones with insufficient residual helium range in red (●).

180° seem to be performing the best, only a small region of the tumor, about 5 % and 6 % is irradiated with spots with too low residual helium range. For beam angle 315° one can nicely see that the region where the helium beam has to pass through the spine is most affected.

Prostate Case

For the prostate case the residual helium range of four beam angles was investigated, 45, 90, 270, 315°, as seen in fig. 4.11. All angles contained spots with insufficient helium range, although their number stayed in the lower single-digit percentage range. The angle with the largest number of spots with insufficient helium range was 90° with 1.1 % of spots flagged. For the other angles 0.9 % (270°), 0.2 % (45°) and 0.03 % (315°) of spots fell short.

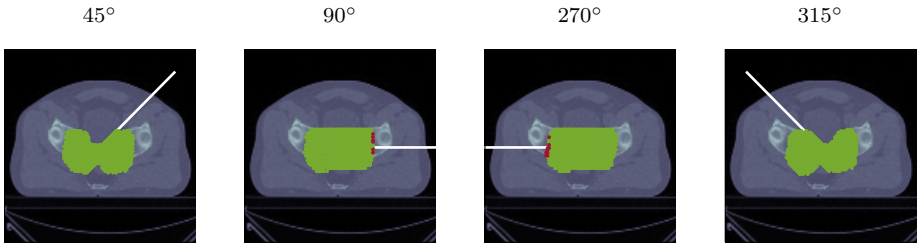

Figure 4.11.: Axial CT slice for the prostate patient with different beam angles. The overlay highlights the spots in green (●) with sufficiently large residual helium range and the ones with insufficient residual helium range in red (●).

Liver Case

For the liver case the residual helium range of three beam angles was investigated 0, 270, 315°, as seen in fig. 4.12. All three angles have to insufficient helium range. For a beam angle of 0° only 1 % have insufficient helium range. For the other two angles 47 % (270°) and 38 % (315°) fell short.

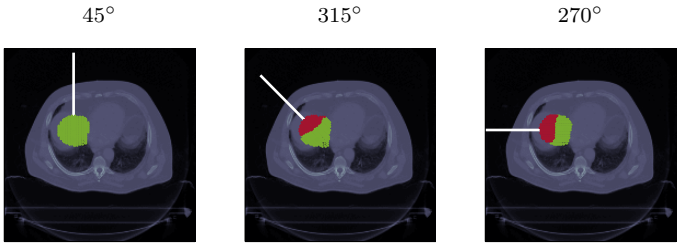

Figure 4.12.: Axial CT slice for the liver patient with different beam angles. The overlay highlights the spots in green (●) with sufficiently large residual helium range and the ones with insufficient residual helium range in red (●).

4.4.2. Comparison of Helium Range Strategies

The following section takes a closer look at the implemented residual helium range strategies: EW–He, Const–RS and EW–RS. As a reference a treatment plan without any residual heluim range strategy was calculated, this means that this plan can have spots with too low residual helium range. In general, all residual helium range strategies successfully ensure a large enough helium range but differ in the distal residual range. Thus, the strategies are compared in terms of percentage of detectable spots. Non-detectable spots are caused by ions stopping in the distal RS or energies exceeding the detector specifications.

Lung Cases

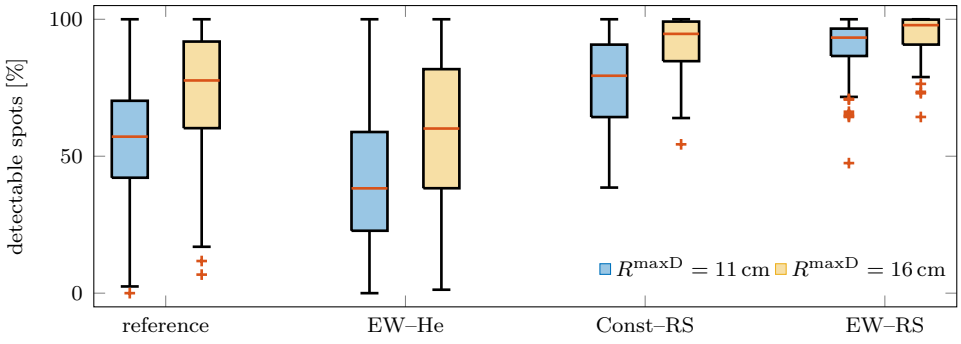

Figure 4.13.: Box plot summarizing the percentage of detectable spots in the lung treatment plans for two detectors: One detector with with a detectable range up to 11 cm and a larger detector with a detectable range up to 16 cm.

Figure 4.13 summarizes the percentage of detectable spots for all treatment angles of all patients for the different residual helium range strategies. The calculation was performed for two imaging detectors with a smaller and a larger maximum detectable range. Unsurprisingly, the larger imaging detector allows for the detection of more helium ions, although this difference between both detectors is not substantial for the EW–RS, that is, on average 5 pp. EW–He is the worst-performing strategy, even being outperformed by the reference plan. In the reference plan, an IES containing a spot with insufficient range

may still include other spots with sufficient range that can be measured. However, in the EW–He method, this IES is irradiated without a mixed in helium beam and therefore cannot be measured. Comparing the two RS strategies, the additional degree of freedom of the EW–RS method leads to an increase in percentage of detectable spots of on average 12 pp for the smaller imaging detector and of 4 pp for the larger imaging detector. However, on average for the larger imaging detector, smaller distal RS are used.

Lung Case No.114

	reference	EW–He	Const–RS	EW–RS
detectable spots [%]	55	35	76	93
detectable helium ions [%]	69	46	70	93

Table 4.4.: Percentage of detectable spots and helium ions for each residual helium range strategy.

In order investigate the different strategys more closely, the dose was optimized and calculated for an example lung patient (No.114) using a beam angle of 90°. Table 4.4 lists the percentage of detectable helium spots and since now the optimal fluence of each spot was calculated, also the percentage of detectable helium ions. When calculating the percentage of detectable helium ions for the EW–He method, the reference point was not the total amount of delivered helium ions but 10 %, which is the carbon-helium ratio, of the delivered carbon ions. This allows for better comparison between all strategys. For the reference and EW–He plan the percentage of detectable helium ions is higher than the percentage of detectable spots, for the Const–RS plan the percentage of detectable spots is higher. Due to higher fluence of the intermediate energies, which are detectable by the reference plan, the reference and Const–RS have the same percentage of detectable helium ions, although the percentage of detectable spots is significantly higher for the Const–RS strategy.

Figure 4.14 provides a closer insight into the chosen proximal RS thickness and the helium range at the detector. No distal RS was used in this case. For the EW–RS strategy thicker proximal RS are used, than for the Const–RS strategy. The residual helium range for the EW–RS strategy as shown in fig. 4.14 shows, that the thickest proximal RS is used for the lowest carbon range in the patient and the lowest energy, before the thickness off the proximal RS decreases. It is noticeable how the proximal RS is used to ”push back” the residual helium range in the detectable range of the imaging detector. So while the EW–RS method has 23 pp more detectable helium ions than the Const–RS method it comes at a cost of thicker proximal RS. For EW–He strategy helium is only used for the high energy where the helium range is sufficient. Also noticeable for the Const–RS method is that the smallest carbon range is not irradiated. These spots exhibit too low helium range and where therefore excluded, while a thicker RS would have come at the

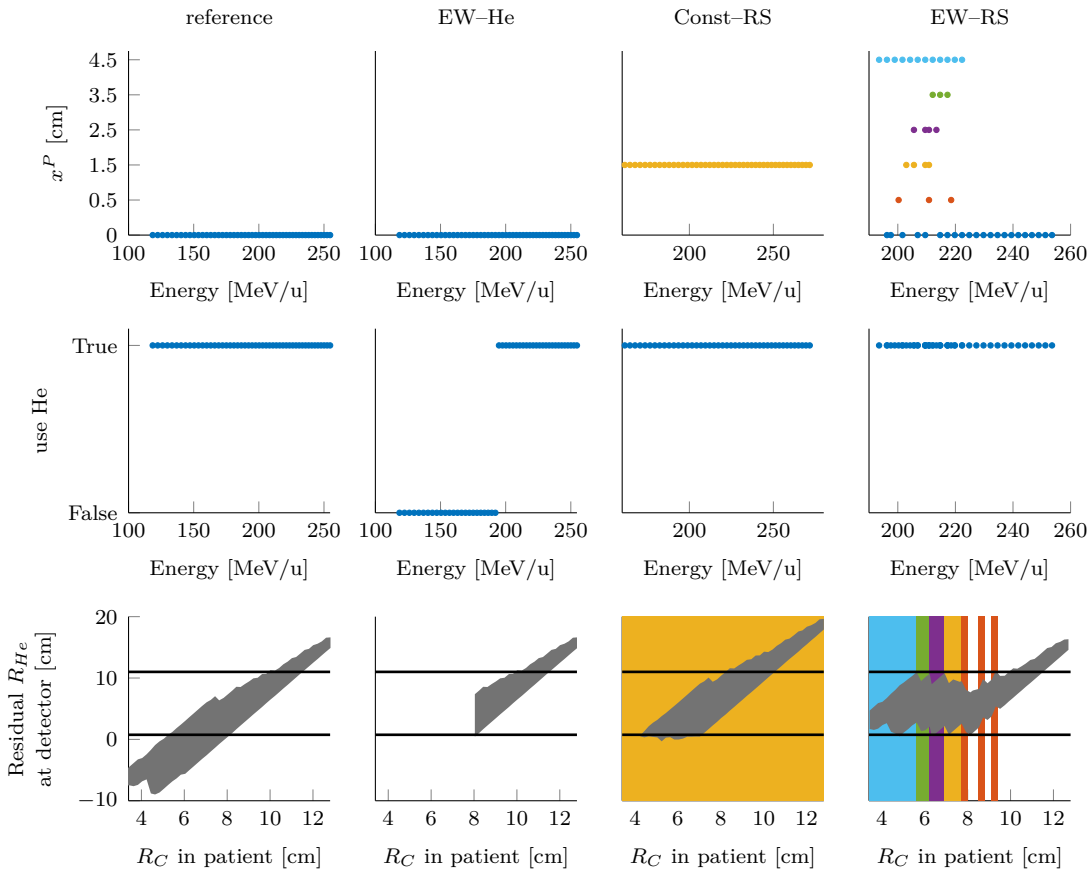

Figure 4.14.: For each strategy the top row displays the proximal range shifter thickness of each energy in the treatment plan. The middle row displays if helium was mixed into the carbon beam for each energy. The bottom row displays the residual helium range at the detector, for each irradiation depth in the patient. Highlighted is the minimum (0.75 cm) and maximum (11 cm) detectable range and the used proximal range shifter thickness. Whereby ■ represents a proximal range shifter thickness of 45 mm, ■ 35 mm, ■ 25 mm, ■ 15 mm and ■ 5 mm.

cost of a reduced amount of detectable spots.

The carbon-helium and helium only dose for all strategies is displayed in fig. 4.15. The difference to the reference plan is also shown. The corresponding carbon-helium and helium only DVHs are shown in fig. 4.16. The residual helium range strategies decrease the delivered helium dose, which is especially noticeable for the EW–He method. For this method, there is a significant reduction in helium dose to the PTV, left lung and body. However since the helium dose contributes little to the total dose the dose reduction is barely visible in the mixed-dose DVH.

The treatment plans utilizing RSs show more scattering, which manifests as a wide dose profile in fig. 4.15 and an increase in dose to the right lung. The mean dose increases from 0.28 Gy (reference) to 0.31 Gy (Const–RS) and 0.33 Gy (EW–RS). These plans also show a reduction in target coverage: the D_{95} value of the PTV decreases from 2.19 Gy (reference) to 2.13 Gy (Const–RS) and 2.16 Gy (EW–RS). In general there is an increase in the integral delivered dose of the plans using RS compared to the reference plan, it is 10 % (Const–RS) and 13 % (EW–RS). For all plans the contribution of the integral helium

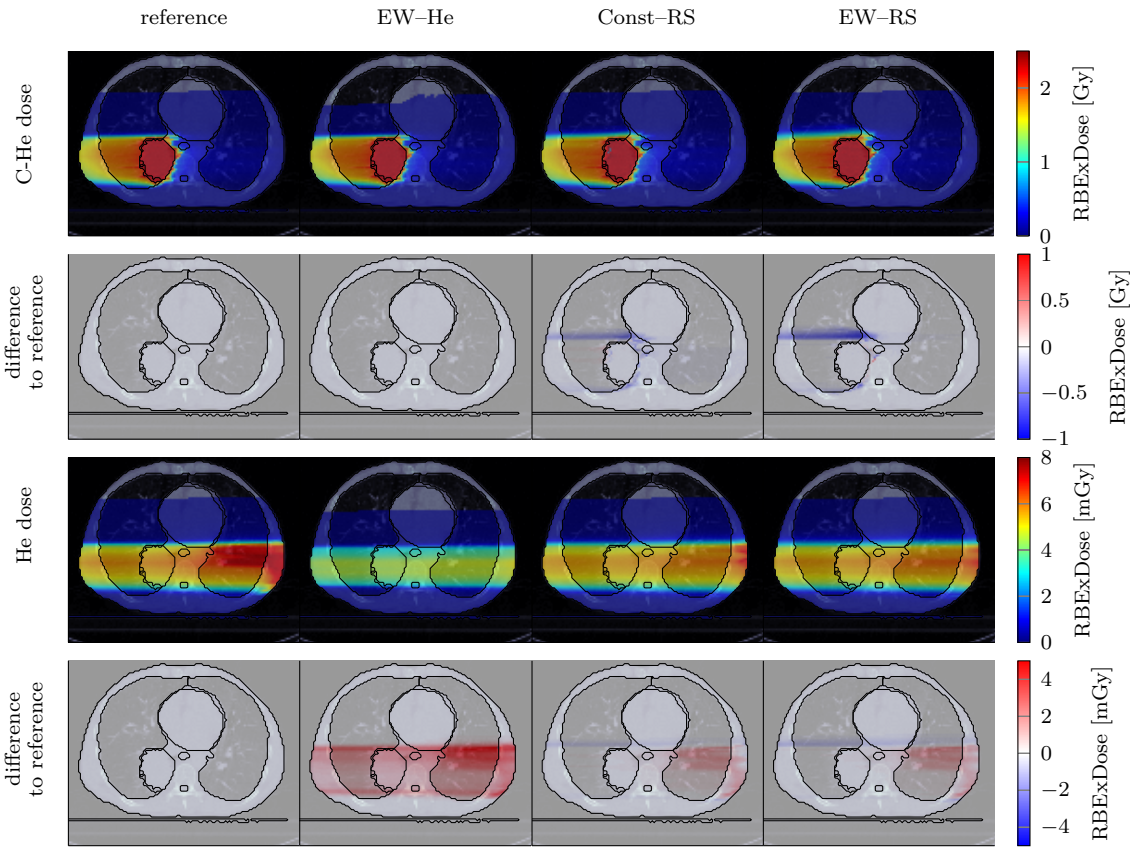

Figure 4.15.: Axial analytically calculated dose slices for each strategy. Top: total mixed carbon-helium RBE weighted doses with the difference to the reference plan below. Bottom: Helium RBE weighted dose and the difference to the reference plan please note the mGy scale in this case.

to the integral carbon-helium RBE weighted dose is below 1 %: 0.57 % (reference), 0.26 % (EW–He), 0.50 % (Const–RS) and 0.48 %(EW–RS).

A comparison of the simulated radiographs with and without proximal RS is shown in fig. A.5.

Prostate Case

In the prostate case the residual helium range can reach up to 45 cm (90°). Such high residual ranges limit detectability. The EW–RS method leads to the highest percentage of detectable spots, nevertheless for opposing beams (90°, 270°) it reaches only 56 % for the smaller detector. For the larger imaging detector an increase to 69 % can be observed. The other two investigated angles (45°, 315°) reach a higher percentage of detectable spots. With the smaller detection system 72 % can be detected, for the larger system 89 %. In the prostate case, distal RS were selected by the Const–RS and EW–RS method.

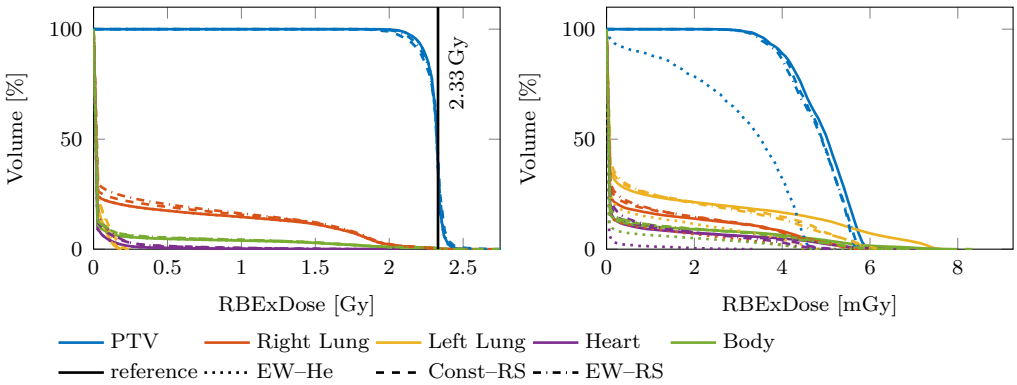

Figure 4.16.: DVH for the different strategies. On the left is the DVH of the total mixed carbon-helium RBE weighted dose and on the right of the helium dose, please note the mGy scale here. The prescribed dose was annotated.

Liver Case

For the liver case, the EW–RS method again showed the highest percentage of detectable spots, with up to 89 % detectable for a beam angle of 270° and the smaller imaging detector, the larger imaging detector enabled detection of 97 % of the spots. Only for one treatment angle, 0° a distal RS was used.

4.5. Methods for Online Treatment Verification

The next section presents the potential of the mixed beam treatment for online treatment verification, with the the methodology described in section 3.4. Part of the results are also described in Hardt et al. (2024).

4.5.1. Verification of Patient Position

The potential for verification of the patient position was investigated on a prostate patient with two opposing angles (90°, 270°). The carbon-helium and helium RBE weighted dose and DVH is displayed in fig. 4.17. For this treatment plan, the integrated helium absorbed dose contributes 1.6 % to the integrated carbon-helium absorbed dose, and the integrated helium RBE weighted dose contributes 0.4 % to the integrated carbon-helium RBE weighted dose. The energies used in this treatment plan ranged from 237 MeV/u to 395 MeV/u.

The total percentage of detectable spots is 69 %, using the detector with the larger sensitive range ($R^{\mathrm{maxD}} = 160\,\mathrm{mm}$). The percentage of detectable helium ions is 62 %. The distal RS of the field with beam angle 90° was 14 cm WET, for beam angle 270° was 11 cm WET. Proximal RS of varying thickness (0 cm - 4.5 cm WET) were used. The EW–RS method was used as a residual helium range strategy since it resulted in the highest amount of detectable helium spots.

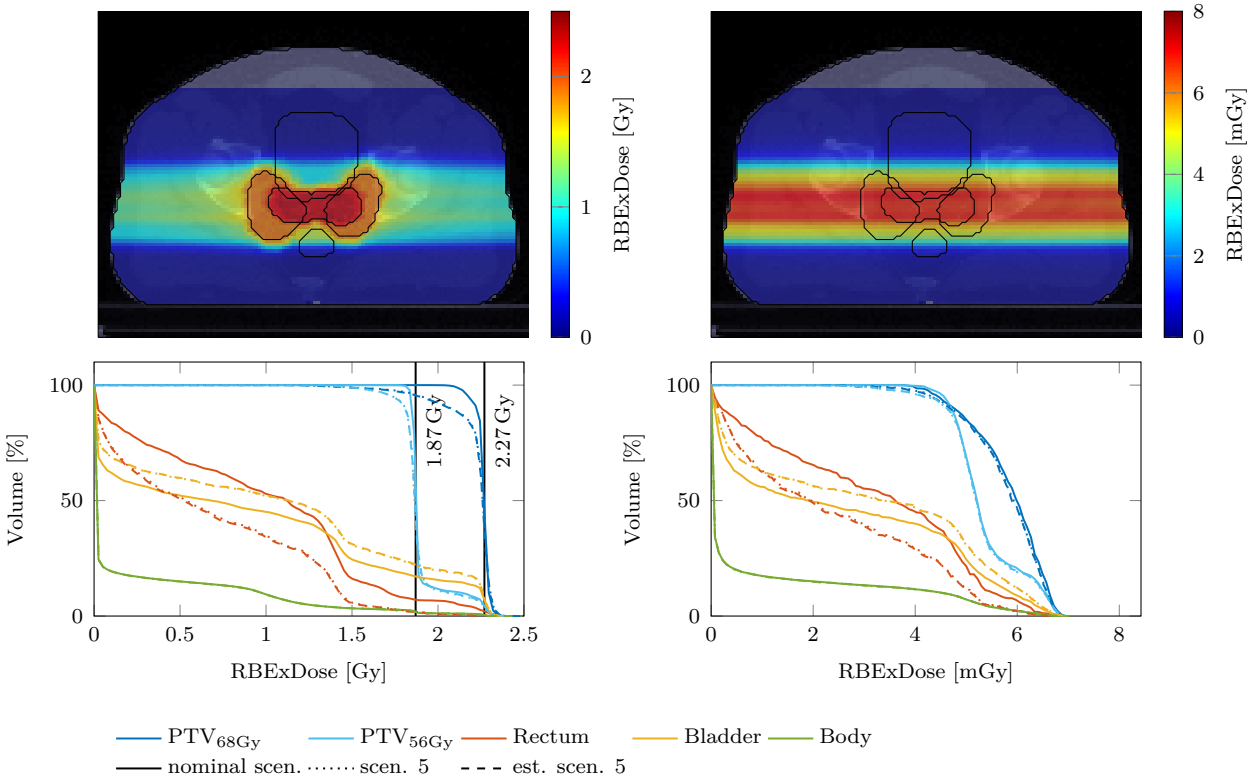

Figure 4.17.: Top: Axial analytically calculated RBE weighted dose slice of the carbon-helium dose (left) and the helium dose (right) of the nominal scenario of the prostate patient. Below are the corresponding DVHs of the carbon-helium (left) and helium RBE weighted dose. Displayed are the DVHs for the nominal scenario, scenario 5 and the estimated dose of scenario 5. Please note the mGy scale for the helium dose. The prescribed doses of the PTVs are annotated in the DVHs.

The FEHeRad of the nominal scenario, no positioning error, and the corresponding DRR is displayed in fig. 4.18. The highest contrast in these radiographs is provided, by the femoral bones and hip bone. The results of the patient position estimation for the MSE and SSIM metric are listed in table table 4.5. During evaluation, a mask was applied to include only pixels through which more than 20 ions passed in the reconstruction, thereby excluding the noisy outer edges of the radiograph. Only the position shift orthogonal to the beam axis (x axis) was considered. The MSE metrics allows to verify the patient position within an error of 1 mm the SSIM within an error of 0.5 mm. On average, the SSIM predicts the patient position more accurately.

Both metrics seem to overestimate the z position while the y position is estimated more accurately. For this beam configuration y axis in world coordinates corresponds to the x axis in the BEV coordinates, the z axis corresponds to the z BEV axis. Consequently position shifts perpendicular to the femoral bone were predicted more accurately.

The estimated patient position was used to recalculate an estimate of the delivered dose, which in turn can be used for quality assurance. The delivered carbon helium RBE weighted dose was evaluated for scenario 5 with the largest position shift. The mean dose

ID	True Position		Estimated Position				Error	
			MSE		SSIM		MSE	SSIM
	y [mm]	z [mm]	y [mm]	z [mm]	y [mm]	z [mm]	ϵ [mm]	ϵ [mm]
0	0	0	−0.2	0.6	0.0	0.2	0.7	0.2
1	−0.6	−0.8	−0.8	−0.2	−0.8	−0.7	0.6	0.2
2	2.5	−1.9	2.3	−1.2	2.5	−1.8	0.7	0.1
3	−0.6	−3.5	−0.8	−2.9	−0.7	−3.5	0.7	0.1
4	1.6	1.1	1.3	1.9	1.6	1.3	0.8	0.2
5	−4.6	0.6	−4.7	1.0	−4.9	0.8	0.4	0.3

Table 4.5.: True and estimated patient position using data from all treatment fields. The error ($\epsilon = \sqrt{\Delta y^2 + \Delta z^2}$) to the true position is calculated. The metrics were MSE and Structural Similarity Index Measure (SSIM) metric

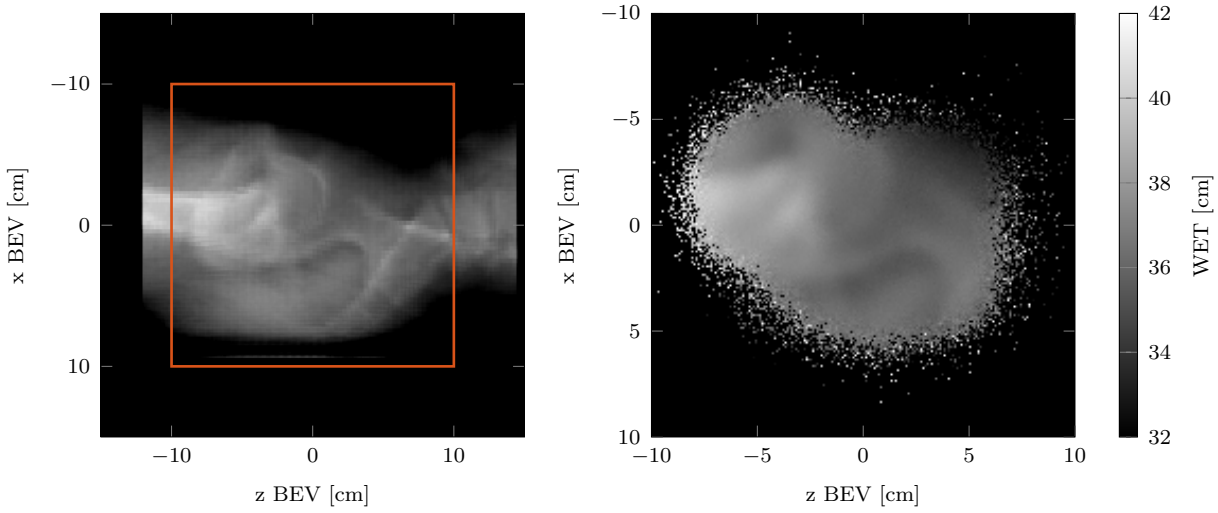

Figure 4.18.: Right: DRR of the nominal scenario of the prostate patient, highlighted is the area of the simulated FEHeRad. Left: Simulated FEHeRad, for a beam angle of 90°

to the rectum decreased from 0.96 Gy to 0.67 Gy from the nominal to the shifted scenario. The mean dose to the bladder, however, increased from 0.86 Gy to 1 Gy. Further, the $D_{95\%}$ value of the $\text{PTV}_{68\,\text{Gy}}$ decreased from 2.18 Gy to 1.91 Gy. For the $\text{PTV}_{56\,\text{Gy}}$, it decreased from 1.85 Gy to 1.74 Gy. Quantifying the underdosage of the target and over dosage of organs at risk that can occur if the patient is wrongly positioned, which can also be seen in the corresponding DVHs in fig. 4.17.

The dose was recalculated with the position estimated by the MSE metric for this scenario, and compared to the actuality delivered dose. The dose difference slice in fig. 4.19 and the DVH in fig. 4.17 shows good agreement between the estimated and actually delivered dose of scenario 5. The gamma pass index of the true and the estimated delivered dose was 99.98 %, for a 2 mm, 2 % criteria, with 7 interpolation points. For comparison the gamma pass rate between the dose delivered in the nominal scenario and in scenario 5 is 56.40 %.

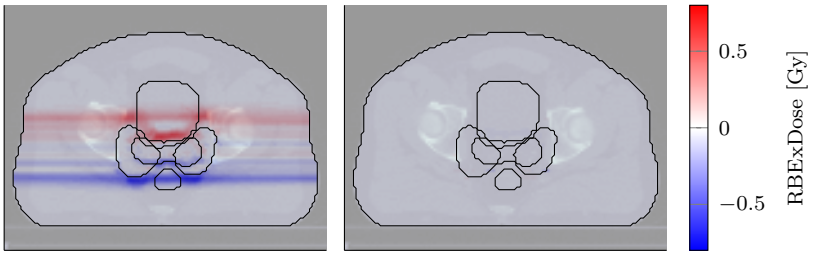

Figure 4.19.: Axial carbon-helium RBE weighted dose difference of scenario 5 vs nominal scenario (left) and scenario 5 vs estimated dose of scenario 5, based on the calculated position using the MSE metric (right).

4.5.2. Verification of Intra- and Intefractional Changes

Intra- and interfractional changes were investigated in a lung case, with a gantry angle of 0°. The RBE weighted dose and dose-volume histogram of the planning CT (Day 0, phase 0) of this lung case is displayed in fig. 4.21. As seen here the helium dose contribution is low. The integrated helium absorbed dose contributes 1.2 % to the integrated carbon-helium absorbed dose, the integrated helium RBE weighted dose contributes 0.3 % to the integrated carbon-helium RBE weighted dose. The energies used in this treatment plan ranged from 194 MeV/u to 318 MeV/u.

The total percentage of detectable spots with the detector with the smaller sensitive range is ($R^{\mathrm{maxD}} = 110\,\mathrm{mm}$) 71 %, while the percentage of detectable helium ions is 63 %. Among the residual helium range strategies, the EW–RS had the largest number of detectable spots and was therefore selected. Consequently, proximal RS chosen by the EW–RS strategy of varying thicknesses (0 cm - 4.5 cm WET) were used, along with a distal RS of 5 cm WET. The FEHeRad of the lung patient (Day 0, phase 0) and the corresponding DRR (Day 0, phase 0) is displayed in fig. 4.20.

Influence of the Sensitive Range of the Detector

The residual range strategy for the treatment plan was calculated based on a maximum sensitive range of the imaging detector of $R^{\mathrm{maxD}} = 110\,\mathrm{mm}$. However, the simulated radiograph was reconstructed twice: once for a maximum sensitive range of the detector of $R^{\mathrm{maxD}} = 110\,\mathrm{mm}$ and once for $R^{\mathrm{maxD}} = 160\,\mathrm{mm}$. The resulting SEHeRad ($E = 220.76\,\mathrm{MeV/u}$, $x^P = 0\,\mathrm{mm}$) for Day 0 and Day 1 is displayed in fig. 4.22. For the larger imaging detector 86 % of the helium spots are detectable, which is 15 pp more than for the smaller imaging detector and 83 % of the helium ions, which is 20 pp more than for the smaller imaging detector

Compared to the FEHeRad displayed in fig. 4.21, the SEHeRad captures a smaller area of the patient, as the irradiated cross section of the tumor is smaller. Comparing the SEHeRads acquired for both detectors, while the smaller detector still produces an instructive image, some range information at the top, particularly the lung lobe region is

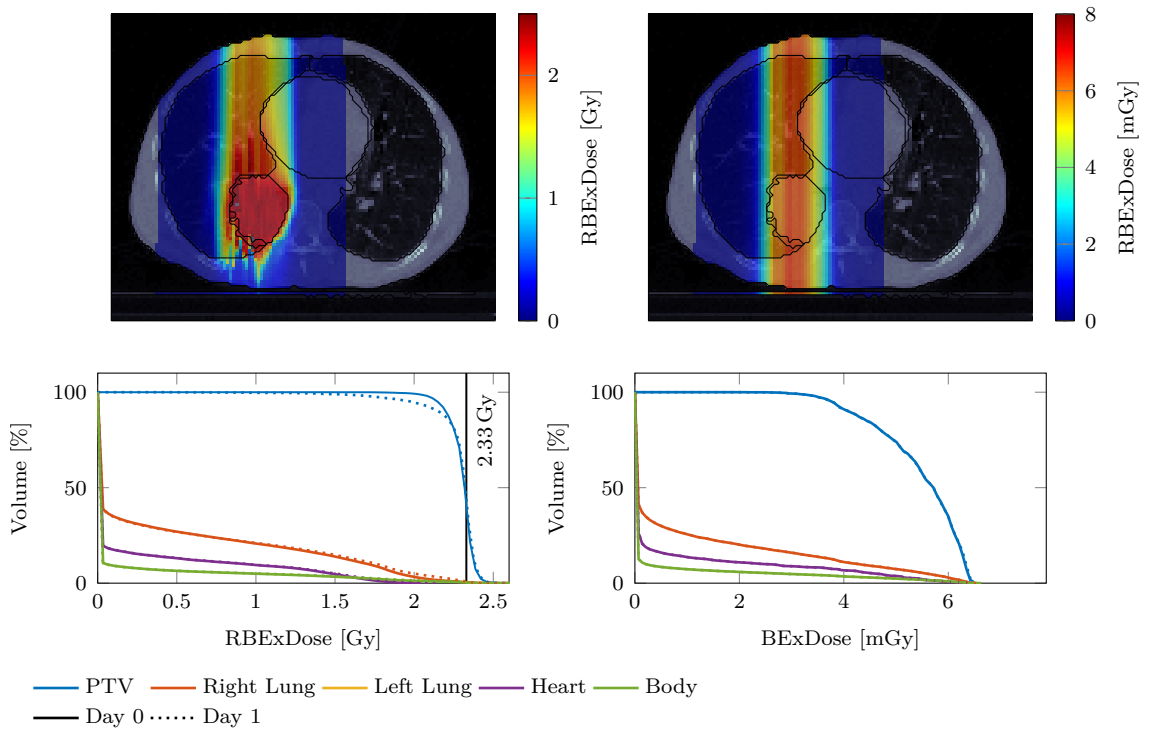

Figure 4.20.: Top: Axial analytically calculated RBE weighted dose slice of the carbon-helium dose (left) and the helium dose (right) of Day 0, phase 0 of the lung patient. Below are the corresponding DVHs for Day 0 and Day 1 of phase 0. Please note the mGy scale for the helium dose. The prescribed dose to the PTV is annotated in the DVH.

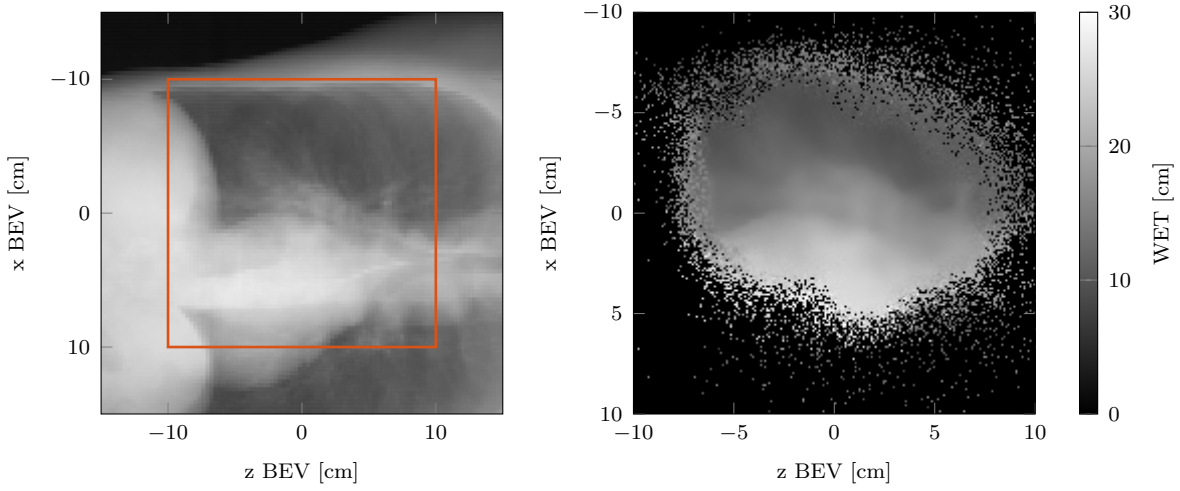

Figure 4.21.: Left: DRR of the patient (Day 0, phase 0), highlighted is the area of the simulated FEHeRad. Right: Simulated FEHeRad (Day 0, phase 0). Most noticeable in the simulated radiograph is the outline of the heart.

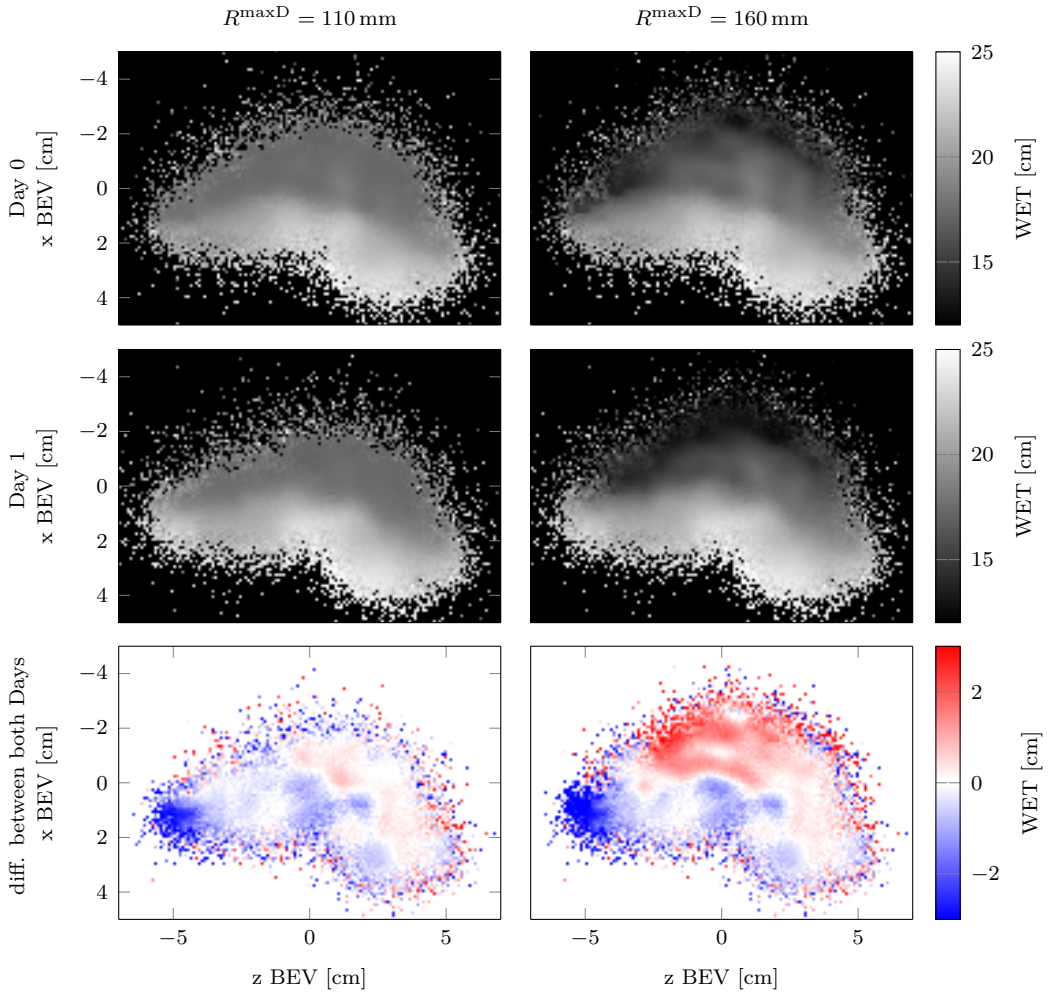

Figure 4.22.: Simulated SEHeRad ($E = 229.76\,\mathrm{MeV/u}, x^P = 0\,\mathrm{mm}$) for Day 0, phase 0, top row, and Day 1, phase 0, middle row and the difference of both images, bottom row. In the left column the image was reconstructed with a detector with a smaller sensitive range ($R^{\mathrm{maxD}} = 110\,\mathrm{mm}$) in the right column with a larger sensitive range ($R^{\mathrm{maxD}} = 160\,\mathrm{mm}$)

lost. As this region is less dense the helium ions passing through it have a higher residual range exceeding the detection capability of the smaller detector. The highest expected residual helium range for the corresponding IES is 122 mm.

The radiograph also suffers from reduced contrast. For instance, rib bones visible in the image from the larger detector are not discernible in the smaller detector's image. Additionally, in the top region, where residual helium ranges approach the upper limit of the smaller detector's sensitivity, systematically higher WET values are observed, when compared to the DRR or the SEHeRad of the larger detector. This overestimation occurs because only helium ions with lower than average residual energy are detected. Even though the percentage of detectable spots, seemed sufficient using the detector with the smaller sensitive range, information in the form of contrast or anatomical feature can be lost depending on the IES.

Interfractional Changes

Considering now the SEHeRads in fig. 4.22 showing WET changes occurring between two fractions. As seen here, they are in the order of multiple cm, occurring for example, due to different positions of the ribs or different motion phases of the heart. If the daily WET changes, occurring due to an error in the patient positioning or due to anatomical change, are too large they can overshadow the changes occurring between different motion phases.

When the dose delivered to the patient on Day 0 versus Day 1 is analyzed, it shows that Day 1 has a reduced target coverage as the D_{95} dose reduces from 2.15 Gy to 1.98 Gy. The maximum dose delivered to the right lung increases from 0.68 Gy to 0.71 Gy,and the maximum dose delivered to the heart increases from 0.18 Gy to 0.19 Gy. The dose delivered to the left lung and and total body is mostly unaffected. The corresponding DVHs can be seen in fig. 4.20

Intrafractional Changes and Breath-Hold

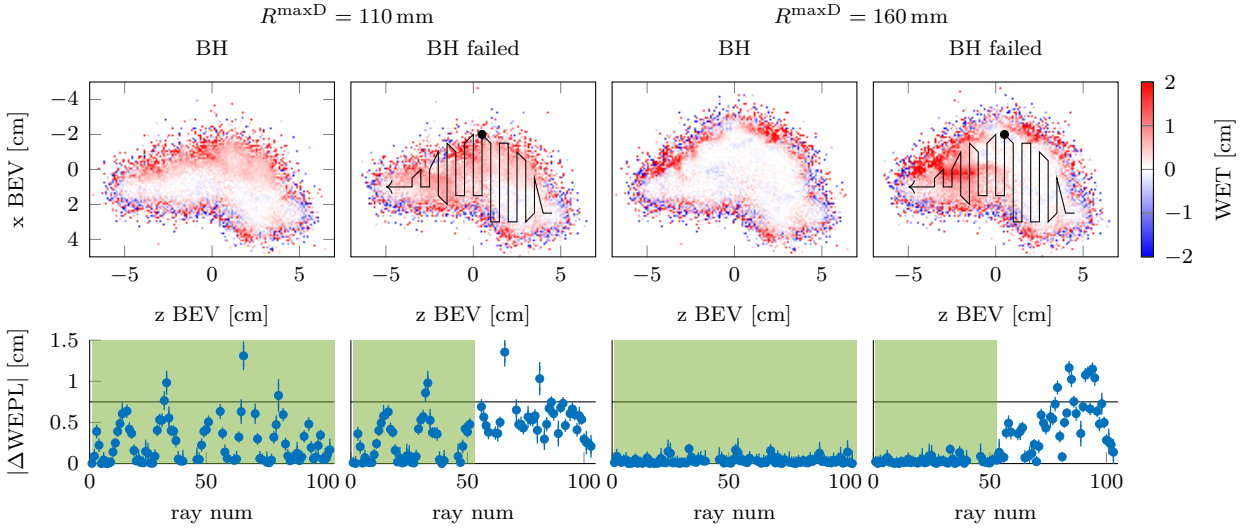

Figure 4.23.: Top row: Difference of simulated SEHeRads ($E = 229.76\,\mathrm{MeV/u}, x^P = 0\,\mathrm{mm}$) to ($E = 232.20\,\mathrm{MeV/u}, x^P = 0\,\mathrm{mm}$) for a detector with a smaller ($R^{\mathrm{maxD}} = 110\,\mathrm{mm}$) and a larger ($R^{\mathrm{maxD}} = 160\,\mathrm{mm}$) sensitive range, for successful breath hold (BH) and failed BH during irradiation. In the failed BH case, the spot scanning pattern and the point at which the BH failed is overlayed. Bottom row: Corresponding absolute difference of the WEPL for each spot with standard error. Highlighted in green are the spots delivered in the same phase. The comparison is performed for spots belonging to the same ray and exceeding more than 100 events.

Figure 4.23 investigates the potential use of the mixed beam method to verify delivery of the IES in the correct motion phase. Compared are for a detector with a smaller and larger sensitive range, simulated radiographs of consecutive IES in the breath-hold and failed breath-hold case. Additionally the absolute difference of the WEPL of each spot of the IESs is compared. The comparison was performed for spots belonging to the same

ray, exceeding 100 measured events.

Considering the detector with the smaller sensitive range ($R^{\mathrm{maxD}} = 110\,\mathrm{mm}$), the overestimation of the WET for areas with residual helium range close to the maximum detectable range of the detector becomes apparent. This overestimation of the WET is energy dependent, with the lower energy overestimating the true WET more. The overestimation is most noticeable in the difference radiograph and in the absolute difference of the WEPL, where a periodic increase corresponding to spots delivered in the affected area can be identified. This complicates the detection of a failed breath-hold, as the increase could also be misinterpreted as patient motion. Nevertheless, even for this case a failed breath-hold can be observed as both an increase in the WET difference in the radiograph and an increase in the spotwise WEPL difference. For the larger energy detector, where the entire IES can be measured, this becomes even more evident.

The WET changes occurring between different motion phases is small compared to the changes occurring between different days. The breath hold comparison is shown for the other IES in appendix A.5 in figs. A.7 to A.11. Also in fig. A.6, within the appendix, the FEHeRad of Day 1 and the difference of phase 0 to phase 1 for Day 1 is shown.

If during irradiation, the WEPL of each spot can be evaluated in real time, a threshold value can be applied. Figure 4.23 highlights such a a threshold value of 0.75 cm. While this threshold may be suitable for the detector with the larger sensitive range, it proves inadequate for the detector with the smaller range. In the latter case, the overestimation of WEPL in high-range spots leads to incorrect classification.

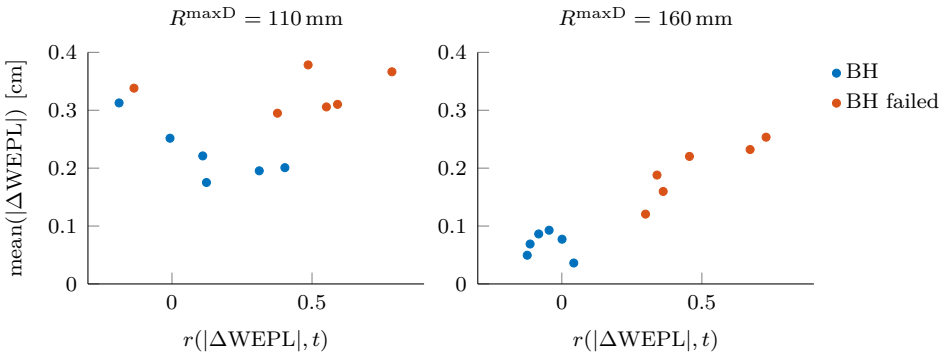

Figure 4.24.: Left: Scatter plot showing the correlation between WEPL difference and irradiation time ($r(|\Delta\mathrm{WEPL}|, t)$) versus the mean absolute WEPL difference (mean($|\Delta\mathrm{WEPL}|$)) for each investigated IES, under both successful and failed breath hold conditions, using the detector with the smaller sensitive range. Right: Equivalent plot using the detector with the larger sensitive range.

For all investigated IES the WEPL difference of each spot was evaluated. The total WEPL difference of all spots was calculated for all cases: breath-hold, failed-breath hold, small imaging detector, large imaging detector. Additionally, the correlation coefficient of the WEPL difference to irradiation time was determined. Figure 4.24 shows the results of this evaluation. Especially for detector with larger sensitive range, scenarios where the

breath-hold failed during irradiation tend do have a higher total WEPL difference and more correlation of the WEPL difference with time.

Correlation of Carbon and Helium Range Changes

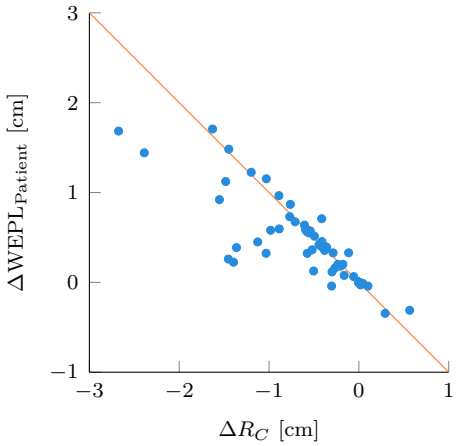

Figure 4.25.: Scatter plot of the analytical difference of the total patient WET ($\Delta\mathrm{WEPL}_{\mathrm{Patient}}$) to the carbon Bragg-Peak position (ΔR_C), for the failed BH scenario of IES ($E = 229.76\,\mathrm{MeV/u}, x^P = 0\,\mathrm{mm}$). The line in orange indicates where where both differences would be equal.

The correlation of patient WET to carbon peak position, was evaluated for the IES $E = 229.76\,\mathrm{MeV/u},\ x^P = 0\,\mathrm{mm}$. The results are displayed in fig. 4.25. For this case, a positive change in the WET of the patient, i.e. larger WET during the breath-hold, results in a more shallow position of the carbon peak during breath-hold. However as also seen here the changes in total WET or helium range do not always correspond to an equivalent change in the carbon peak position. This complicates inferring the carbon change with corresponding dose change solely from the measurable helium range change. In this investigated scenario the change in the carbon peak position tends to be under estimated, when compared to the helium range change. However, this result should only be understood as an example, as other anatomies might even invert this behavior.

5 Discussion

5.1. Detection of Mixed Carbon-Helium Beams

5.1.1. Experimental Helium Radiography

WET Accuracy

The accuracy of the measured and simulated WET compared to the ground truth was evaluated in section 4.1.1. The error of the simulated values to the ground truth values is within 3 %. Hereby the ground truth values were calculated using eq. (3.4). However this equation is merely an approximation, additionally the insets varied slightly in length. The most accurate method to determine the ground truth is to measure the WET directly as the proximal shift of the Bragg-Peak position of with and with out the material inserted in the beam path. These measurements have yet to be performed. Once performed and evaluated, they will give a closer insight to the WET accuracy of simulated and measured helium radiographs. Nevertheless, since there is some uncertainty to be expected in the accuracy of the WET values in any measurement and simulation, the focus during evaluation of the radiographs was on WET changes and not on absolute WET values.

Anthropomorphic Helium Radiograph

An anthropomorphic measurement was presented in section 4.1.2. While basic anatomical features are visible, the image quality suffered severely from helium fragments and missing front tracker. During image acquisition, selecting the used energy is crucial: as too high an energy can over saturate the detector and lead to inaccurate residual energy measurements. Filtering of helium fragments may certainly be improved in future studies.

Unstable Intensity of the Beam

The beam at HIT was operated in an experimental low intensity mode. Therefore, a feedback system controlling the intensity of the beam had to be turned off. This causes the intensity of the beam to become unstable with significant fluctuations during irradiation. Additionally, the intensity is not reproducible and lower at the beginning of the spill.

Especially in calibration measurements it would be much more preferable to rely on a constant intensity that covers the entire sensitive area of the detector. To emulate a constant calibration intensity, the beam was scanned several times: three times across the detector from bottom to top and three times from top to bottom. However, the unstable fluence still results in a more challenging calibration and acquisition of radiographs, as the calibration data set includes some energies with very unstable beam fluence, degrading the accuracy. Further rescanning could enhance the accuracy of the calibration procedure and of acquired radiographs, however this results in longer acquisition times.

Limitations of the Simulation

The main limitation in the simulation of the detection system is that only primary helium ions are scored and no carbon or helium fragments. The image quality of the helium radiograph would suffer due to nuclear fragments from both helium and carbon ions. The impact of especially the carbon fragments occurring in a mixed beam has yet to be investigated as soon as mixed-carbon helium beams can be consistently produced and used for measurements. Further, no error in the energy detection was modeled.

As such the simulations conducted in this work represent heavily idealized conditions. It is still unclear how various detectors are able to resolve the required information in time and space, and how the obtained information could be fed back close to real time and be practically used. These issues are particularity crucial for online motion monitoring. Nonetheless the primary goal of this thesis is to suggest potential use cases of such a mixed carbon–helium irradiation and imaging system, outlining desired performance of the respective systems and treatment planning strategies considering the availability of these radiographs during and after irradiation.

The SEHeRad evaluated in section 4.5.2 where simulated using 1×10^6 histories each. There are between 1.5 to 2.9 times more helium ions in the delivery of the energy than helium histories in the simulation, therefore the number of simulated helium ions and delivered helium ions are of the same magnitude. Consequently for SEHeRad it is computational feasible to simulate the same number of ions as also delivered in the IES of the treatment plan. Additionally the noise level in these images should be comparable to noise image of measured radiographs. For the prostate case the entire treatment field was simulated, to acquire the FEHeRad, here there are 19 times as many helium ions in the delivery than helium histories in the simulation.

As seen in fig. 4.6 the DRR and the simulated HeRad are in good agreement when the same HU to RSP conversion is used.

5.1.2. Considerations for a Mixed Carbon-Helium Beam Detector

Ideally, a detector for a mixed carbon-helium beam should be capable of handling high particle fluxes, provide reliable particle identification and offer a large sensitive WET range.

A key challenge in mixed beam irradiation, particularly at high energies, is the fragmentation and subsequent loss of primary ions, along with beam broadening. This scattering and widening of the beam contribute to increased range mixing, as helium ions traverse more heterogeneous tissue with varying densities. Consequently, accurately determining the carbon ion range based on the helium range, or reconstructing the patient's WET, becomes more difficult.

Particle Fluence

A mixed carbon-helium beam detector has to be optimized for the higher fluence rate used in particle therapy, compared to the lower fluence rate typically used in particle imaging. Carbon intensities used in particle therapy are in the range of 2 MHz to 80 MHz (Ondreka et al., 2009), this represents primary carbon particles per second. This corresponds to a helium fluence of 0.2 MHz to 8 MHz. Therefore, neglecting loss of primaries and production of fragments in the beam monitoring system or potential range shifters, particle rates between 2 MHz to 88 MHz can be expected.

The particle fluence distal of the patient consists of carbon fragments, primary protons, deuterium, tritium, ^{3}He and ^{4}He, in addition to the primary helium fluence from the mixed beam and the corresponding helium fragments. A TOPAS simulation of the fluence energy spectrum for both carbon and helium beams, along with their respective fragments, was analyzed. The data was provided by Facchiano et al., 2025. For a beam energy of $E = 250\,\mathrm{MeV/u}$ ($R_C = 13\,\mathrm{cm}$, $R_{He} = 38\,\mathrm{cm}$) the total fluence was evaluated at a depth of 30 cm, approximately 8 cm before the helium Bragg peak and near the entrance of the detector. At this depth, the combined fluence of primary particles and fragments amounted to 32 % of the primary carbon fluence corresponding to a fluence of 0.7 MHz to 28 MHz at the detector entrance. In general, the fragments possess significantly lower energy than the primary helium ions and exhibit greater scattering, resulting in their distribution farther from the primary beam path. A substantial number of low-energy secondary protons and helium ions produced from carbon fragmentation will also reach the detector.

The ProtonVDA detector operates at a readout rate of 3 MHz. At the time of this work, the front tracker of the detector could not be used at all times due to technical difficulties and availability of spare parts. However, for the mixed beam method, it is anyway infeasible to use the front tracker, as the high fluence would lead to its saturation.

In the absence of the front tracker, the spatial resolution of the resulting images is reduced, as illustrated in fig. 4.6, since the ion position proximal of the patient and thus the origin of the tracked ion path must be estimated.

Another detector approach is integrated mode imaging, which can accommodate the particles fluence of clinical ion beams. However, single-event systems generally provide superior image quality. Recently, Fullarton et al. (2025) used an integrated mode detector, a plastic scintillator coupled with CCD cameras, to acquire proton radiographs to track the position of moving objects in a phantom study, showing the potential for motion monitoring. Additionally, Simard et al. (2025) demonstrated and analyzed the use of an integrated mode system for carbon radiography, comparing integrated mode imaging for a heavy ion to proton radiography.

Particle Identification

To improve the quality of measured data in mixed beam imaging, it is essential for the detector to support particle identification in order to filter out signals arising from the produced fragments, that is mainly protons.

In case of the ProtonVDA detector, the absence of a trigger from the front tracker complicates the distinction between signals produced by primary helium ions and those generated by helium fragments. While cuts are applied to the E signal to filter out data produced by fragments, this approach is limited and does not allow for proper particle identification.

Gehrke et al. (2018b) used pixelated silicon Timepix detectors for helium radiography. These detectors measure energy deposition and can identify particles based on cluster size and volume. However, since they rely on measuring deposited energy, their accuracy is highest when ions are detected near the end of their range. As a result the WET accuracy is highly sensitive to the initial ion energy. To address this, an *Energy Painting* technique was developed, in which different areas of the radiograph are acquired at different energies tailored to the expected WET of the patient (Metzner et al., 2024). For mixed beams however, the energy can not be chosen this freely, making this detector impractical for mixed beam imaging.

In Volz et al. (2018) a $\Delta E - E$ telescope, made of a five stage plastic scintillator detector (Bashkirov et al., 2016) is used for helium radiography. The energy deposited in the stage where the ions stop is denoted as E, and the energy deposited in the preceding stage as ΔE. When ΔE is plotted against E, different particles form distinct curves or bands. However for the used detector, the identifiable particle rate was only 1 MHz which is lower than the ProtonVDA detector and thus too low for mixed beam irradiation.

A time of flight (TOF) detector could be a suitable option for mixed beam irradiation. In this approach, the TOF in air can be used to determine the velocity of ions after passing through the patient. When coupled with a small scintillator detector to measure the

deposited energy, this system could enable particle identification. The detection sensitivity of a TOF system depends on the spacing between the detector planes and their temporal resolution (Ulrich-Pur et al., 2024; Krah et al., 2022). One advantage of this system would be that, unlike a calorimeter or range telescope, it does not require the particles to stop within the detector material. This results in reduced fragment production, scattering and loss of primary particles in the detector. However, the feasibility of using a proximal detection unit must be considered, especially under the high particle fluences in radiation therapy.

Sensitive Detection Range

In ion imaging, the beam energy is typically selected based on the the expected WET of the patient and the sensitive range of the detector. However, in mixed beam applications, this approach is only partly possible, as the beam energies are determined by the carbon energies needed for treatment. Section 3.2.3 outlines several strategies used to adjust the carbon and consequently helium range, with respect to the expected residual helium range at the detector.

An analysis of these strategies indicates that for the abdominal cases, prostate and liver, the detector with larger sensitive range (16 cm) appears necessary. Notably, in the prostae case, even this detector size proved limiting: only 62 % of helium ions were detectable in the opposing beam plan presented in section 4.5.1, suggesting that a detector with an even greater sensitive WET range may be beneficial.

For lung cases the detector with smaller sensitive range (11 cm) seemed sufficient when number of detectable spots were compared, especially in combination with the EW–He strategy for residual helium range. However, as shown in fig. 4.22 a detector with too small sensitive range can lead to the loss of important information, and the cost benefit of a detector with larger sensitive range than 11 cm should be considered for lung cases.

Additionally, a larger sensitive WET range allows for the use of thinner distal RS, which are employed to shift the helium range into the sensitive range of the detector, which is associated with improved image quality. However, an experimental investigation of the detection properties, especially when thick distal RS are used, is necessary to fully understand the impact of all factors on detection properties.

The two investigated configurations were a maximum detectable helium range of 11 cm and a maximum detectable range of 16 cm. For comparison, the ProtonVDA detector has a maximum measurable range of approximately 11 cm, while the range telescope used by Volz et al. (2020) has a maximum range of 12.7 cm and the cubic polyviniltoluene-based scintillator used by Mazzucconi et al. (2018) exhibited a maximum WET of approximately 18 cm.

5.2. Treatment Planning for Mixed Carbon-Helium Beams

5.2.1. Mixed Carbon-Helium Dose

Mixed Beam Dose Calculation

Fast dose calculation for mixed carbon-helium beams with pencil-beam algorithms could, in principle, directly store the mixed carbon-helium kernel. To maintain the flexibility required for this work, carbon and helium dose calculation were performed independently by the pencil-beam algorithm. This allows for the investigation of the contributions of only carbon or helium. Further, the mixing ratio can easily be changed to investigate multiple configurations and can be adjusted if needed for the used detector.

Early results from accelerating the mixed carbon-helium beam indicate that our assumption of an equal carbon and helium phase space is incorrect. However, since the helium dose contribution is low, the resulting inaccuracies are negligible. Furthermore, once the phase space of a clinical mixed beam is established, integrating this information into the existing framework will be straightforward.

Evaluation of the depth-dose curves at high helium energies reveals that fragmentation and the resulting loss of primary helium ions are so significant that the dose at the Bragg peak exceeds the dose in the ”plateau” region.

Optimization of the Mixed Beam Dose

The difference between optimization using the total carbon-helium RBE weighted dose and using the carbon RBE weighted dose was evaluated. It was shown that both combined and carbon-only optimization achieve suitable plans, as the contribution of the RBE weighted helium dose to the total RBE weighted dose is low. Due to the proportionality of deposited energy and absorbed dose with Z^2 (eq. (2.3)) helium ions with only 10 % of the carbon fluence are expected to deposit around 1 % of the carbon absorbed dose. The contibution to the RBE weighted dose is expected to be even lower, as carbon ions have a higher RBE than helium ions and exhibit increased RBE near the Bragg-Peak, with lower RBE in the plateau region (Grün et al., 2015; Bronk et al., 2020; Phillips et al., 1977).

Of practical computational interest here is the is the memory required to calculate a combined dose influence matrix. The dose influence matrix is a large, sparse matrix containing for each spot in the treatment plan the dose delivered to each voxel in the CT at unit intensity. This matrix is expected to be less sparse for helium ions due to higher scattering and the transmission of the beam. This means a mixed beam matrix will require more than twice the memory of a pure carbon beam. If the helium dose is calculated from a known optimal intensity vector w the memory consumption is significantly reduced, as

there is no need to compute the dose influence matrix as an intermediate step. Thus, the dose optimizations within this thesis were performed considering only the carbon RBE weighted dose.

Contribution of Helium to the Total Delivered Dose

The contribution of the integral helium RBE weighted dose was under 1 % for every treatment plan. In the investigation of the Box Phantom, a helium fluence exceeding 30 % resulted in an integrated helium RBE weighted dose greater than 1 % of the integrated carbon dose. This suggests that a helium fluence above 10 % could be used if necessary for detection. Additionally, fluctuations of the helium fluence are not expected to significantly affect the delivered dose distribution.

In this thesis, no combined RBE model for both ions in the mixed radiation field was used. Instead, the total effect was calculated by calculating the combined dose averaged α and $\sqrt{\beta}$ values from the linear quadratic model (3.2.1). A data-driven parameterization of the helium RBE was chosen, uncertaintys of the helium RBE model are expected to be negligible due to the small fluence contribution of the helium as well as the primary low LET of the helium passing through the patient. In principle, the planning framework could also incorporate other RBE models if the respective kernels are precomputed.

Dose Contribution of Range Shifters

As shown in fig. 4.8 the analytical and MC dose calculation aligns well for carbon ions, but for the lighter helium transmission beams, the analytical dose calculation overestimates the dose compared to MC dose calculation. This suggests that the modeling of the additional beam widening with the added spread σ_{RS} is not accurate enough for helium ions. For helium ions a more refined modeling of beam widening due to RS should be used. This could be implemented as a weighted sum of multiple σ_{RS} to better capture the broader distribution of scattered the helium particles.

It should also be noted that the RS was positioned at the nozzle, approximately 1 m away from the iso center. Shirey et al. (2017) also reports that the accuracy of the pencil beam dose calculation for protons suffers for larger air gaps. Hence, minimizing the air gap would be beneficial. This thesis explored a system designed to automatically adjust the proximal RS, with implementation at the nozzle being the most feasible option, since a RS is already integrated there in the HIT setup. Alternative configurations to minimize the air gap are also conceivable, including the possibility of a couch-mounted RS. Since the analytical dose calculation of the carbon dose is satisfactory and the analytical dose calculation for helium overestimates the delivered dose, these inaccuracy's are acceptable.

Monte Carlo Simulation

Pencil beam algorithms are widely used in treatment planning due to their computational efficiency, but they are known to inadequately model multiple Coulomb scattering. This limitation is particularly noticeable in lung therapy, where scattering in the low-density lung tissue as well as at the interface between the target and the lung tissue is incorrectly modeled (Schuemann et al., 2015). For lung tumors, it has been demonstrated that pencil beam algorithms can overestimate the delivered dose by up to 46 % in proton therapy (Taylor et al., 2017).

Figure 4.5 displays the analytically and MC simulated dose profiles. Since the carbon kernel set used for the analytical pencil beam dose calculation was not simulated with MC, and phase space data was instead approximated from an existing kernel, there are some uncertainties in the approximation of the unknown phase space. However, for the helium dose, this was not an issue, as the kernel set used in the analytical dose calculation was also simulated, allowing the same phase space parametrization to be used in the simulation of the kernel set and the simulation of a treatment plan. Without the use of RS, the MC and analytical dose calculation are compatible in the homogeneous region of the phantom.

Using 1×10^7 histories in the simulation of a full treatment plan is a good compromise between computational efficiency and accuracy, as the simulation already takes several hours. In general the focus of the MC simulations in this thesis was not an accurate dose calculation but an estimation of acquired mixed beam helium radiographs.

Figure 4.6 shows the simulated radiographs and the DRRs using the HLUT from matRad and the HLUT extracted from the material conversion used in the TOPAS simulations. The used material conversion assigned materials of different elemental composition and densities to the individual voxels, based on their HU value, leading to a slightly different RSP than the one given within matRads HLUT. Another option during the simulation would be to use water as material for all voxels, with the density provided thru matRads HLUT. While the simulated HeRads and the DRR using the TOPAS HLUT agree well, there is a $\sim 2\,\text{mm}$ or $\sim 1.1\,\%$ offset between the DRRs. The simulations were still performed using this material conversion and not with water of different density, as the material conversion allows for the incorporation of tissue like material, allowing for more more accurate simulation of scattering or fragmentation. The differences between the two DRRs are within the expected range uncertainty and can be interpreted as an uncertainty in the HU conversion.

In general, the simulated helium energies were above the typical helium energies used in radiation therapy and in the MC tool TOPAS. Comparing the cross sections and ranges with measured data at these unusually high helium energies for radiation therapy would be beneficial. Mairani et al. (2022) discusses the need for more reliable models of non-elastic interactions of helium ions.

5.2.2. Treatment Planning Strategies

Residual Helium Range Strategies

The developed mixed carbon-helium beam treatment planning framework was applied to evaluate the feasibility and limitations of the mixed beam approach, particular with respect to residual helium range across different patient sites (lung, prostate, liver). Residual helium range is a limiting factor in the selection of patients and treatment angles, as not all combinations are viable without additional mitigating strategies.

Analysis revealed that in most cases, the helium range was insufficient for at least a subset of the planned carbon spots, regardless of the used beam angle. However, all implemented helium range strategies (EW–He, Const–RS, EW–RS) successfully ensure adequate helium range. Therefore the planning strategies evaluated here allow for more flexibility in the determining optimal treatment angle, thereby expanding clinical applicability of the mixed beam approach across a wider range of patient cases and treatment sites.

Among the strategies, EW–RS resulted in the highest number of detectable spots. Additionally, this method was less dependent on the sensitive range of the detector, as the difference in detectable spots between the two tested detectors in lung cases was only 5 pp. In contrast the EW–He approach produced the fewest number of detectable spots. While the Const–RS method yielded fewer detectable spots than EW–RS, it may be more practical for clinical implementation. Since the proximal RS is not changed during treatment, it can also be positioned closer to the patient, reducing scattering and improving resolution.

A hybrid approach that combines the EW–He and Const–RS methods may be worth exploring. In this approach, a thinner proximal RS could be employed, while energy layers still exhibiting insufficient helium range would be irradiated with a pure carbon beam.

The main drawback of using RS to optimize residual helium range lies in the additional scattering and fragmentation they introduce. These effects contribute to a loss of target coverage, increased patient dose, and more noise in the acquired helium data.

Selection of Beam Angles

The selection of beam angles in particle therapy is a critical aspect of treatment planning. In clinical practice, one of the factors in choosing a beam angle is minimizing the dose to nearby OARs. In mixed beam planning, an additional consideration arises: the helium range. For lung cases, beam angles of 0° and 180° appear to be the most suitable for treatment, as they have the least amount of spots with insufficient helium range. Disadvantages of using the 180° beam would be that it requires irradiating through the patient couch and a potential distal RS would have to be placed above the patient.

A combination of treatment angles could also be used. In the lung case: the upper

portion of the tumor can be irradiated using a 180° beam, while the lower portion can be irradiated from 0°. This strategy ensures that only spots with sufficient helium range are used from each direction. A similar approach could be applied in the prostate case, using opposing beam angles of 90° and 270°.

However, the limitation of this strategy is that only very few centers use carbon gantry's. As of 2025, only three are in clinical use (PTCOG, 2025a), including the HIT (Heidelberg Ion Therapy Center) among them. Most facilities use fixed beam lines and are limited to horizontal and vertical orientations, with a few offering an oblique beam line. A fixed beam line may offer an advantage over a gantry for mixed beam irradiation, as it could simplify the setup of a distal range shifter.

To increase flexibility in beam angle section of mixed beam treatments, upright particle therapy may offer a promising solution. This emerging treatment method places the patient in seated position rather than lying on a treatment couch. Instead of rotating the beam around the patient, the patient is rotated to achieve different treatment angles Rahim et al., 2020.

5.3. Validation of Treatment Delivery with Mixed Carbon-Helium Beams

The main advantage of the mixed beam approach lies in its potential for true online monitoring and its high sensitivity to WET changes during treatment. The reconstructed SEHeRad after delivery of each energy layer and the FEHeRad could provide valuable feedback to the treating physician. These radiographs would enable a 2D image reconstruction of the treated anatomy from beam's eye view, offering insight into both range deviations and the underlying anatomical changes. This information forms the basis for a patient positioning verification system and intrafractional monitoring, contributing to more precise and adaptive particle therapy.

Compared to other range verification methods like PET or prompt gamma imaging the patients WET is measured, that is correlated to the carbon peak position. The other methods, measure an activity signal or emission profile correlated to the particle's range. The benefit of measuring WET is that it can, for example, also be used to check the RSP to HU conversion used during treatment planning.

MR-guided particle therapy is another emerging technique, offering good soft tissue contrast and real-time capabilities. However for online adaptive planning the conversion of MRI images to relative stopping power is especially challenging since it has to be fast and accurate (Paganetti et al., 2021; Hoffmann et al., 2020). The mixed beam method doesn't require this additional step, but unlike a 3D image acquired in MRI imaging only 2D projections are acquired.

5.3.1. Patient Positioning

The reconstruction of the patient position was evaluated using the nominal and five sampled scenarios of a prostate case. The evaluation used the MSE and SSIM metric. For the MSE metric an accuracy better than 1 mm was achieved for the SSIM an accuracy better than 0.5 mm. Unlike MSE, which is sensitive to changes at the level of individual pixels, SSIM is a more global metric that considers structural information in the image by analyzing the cross-correlation of pixel values. Therefore the SSIM is less sensitive to the absolute pixel values and to uncertainties in the conversion of HU values to RSP.

The accuracy was lower along the z axis, suggesting the region imaged influences the accuracy of the method and thus the used beam angle and patient site. Therefore, this method is expected to be most effective in high-contrast regions, such as those containing bone structures. In the prostate case this is provided by the hip and femoral bones. The expected contrast in the radiographs could also be considered when beam angles for treatment are selected. Additionally, the accuracy of this method is likely to decrease when inter fractional changes are introduced, and a radiograph from a different fraction is compared to the DRR of the planning CT.

For patient positioning, orthogonal x-ray images are commonly used. The advantage of using mixed beams as a secondary verification system is its potential to detect patient movement that may occur between initial positioning and irradiation. Additionally, SE-HeRads could be used to determine when the position change occurred. While various algorithms exist for radiograph-based patient positioning, the primary goal of this work was not to develop a superior registration method, but rather to demonstrate the potential application of image registration in the context of mixed beam radiation therapy.

The dose was recalculated for an estimated patient position and compared to the true patient position of that scenario, achieving a gamma pass rate of 99.98 %. For that reason it seems that the patient position can be verified from mixed beam radiographs and the actually delivered dose can be recalculated with sufficient accuracy.

5.3.2. Inter-fractional Changes

Intra and inter-fractional WET and the resulting dose changes were evaluated on a lung patient. The lung is an especially interesting patient site for mixed beam radiation therapy. Firstly, the expected residual helium range is smaller than in the investigated abdominal cases and this eases the detection. Secondly, for non small cell lung cancer, studies have shown that proton therapy is highly sensitive to range and motion uncertainty, which can diminish its advantage over conventional photon therapy (Liao et al., 2018), this accounts for carbon therapy as well (Steitz et al., 2016). In such scenarios, mixed beam irradiation offers a potential benefit through in-vivo range monitoring.

During evalaution of interfractional changes in the lung patient, it should be noted that

image regsitration between the planning CT and the fraction CT was performed using 3D Slicer. This process may introduce a registration error, potentially leading to additional WET variation due to the misalignment. However, such errors could also occur during actual treatment delivers, as this corresponds to an inaccurately positioned patient.

5.3.3. Intra-fractional Canges

It was investigated on whether a successful breath-hold during irradiation of an IES can be verified with the mixed beam method and whether a change in the motion phase occurring in a failed breath-hold can be detected.

The motion phase in which an energy was delivered could be verified, as demonstrated in fig. 4.23. Here the change in motion is noticeable as both an increased spotwise WEPL difference and as a WET difference in the SEHeRad. Interfractional changes were eliminated from this evaluation since the radiographs compared corresponded to successively delivered IES from the same day. As the changes occurring between fractions, presents a challenge in verification, since small changes between motion phases might be overshadowed by WET changes occurring between treatment fractions. Larger RS with more image noise increase the difficulty in evaluating these radiographs.

A threshold on the WEPL difference, to classify a failed breath-hold was applied, which could be evaluated online during treatment. This would serve as a low-latency verification mechanism, complementing higher-latency image verification tools by pausing irradiation until the patient returns to the breath-hold position or the radiographs are evaluated. A broader treatment planning study with more patient cases and fractions seems sensible to determine the optimal threshold value. The challenge is finding a threshold that is sensitive enough to detect a failed breath-hold but not to sensitive that it results in frequent interruptions of the treatment. This would prolong the treatment which may cause the patient to become restless leading to even more motion. Prolonging treatment also reduces the efficiency of a treatment facility.

When evaluating the mean spotwise WEPL difference it would be sensible to investigate in advance which spots are most likely to experience significant carbon range changes due to a WEPL change. For example, spots that cross from the tumor into the lung, or could irradiate the heart. This would allow for the online evaluation and verification to focus on these spots. Such analysis could be conducted during treatment planning by evaluating multiple error scenarios.

The total mean spotwise WEPL difference, as well as the correlation coefficient of the mean spotwise WEPL difference with time, was calculated for all IES. Particularly for the detector with the larger sensitive range, it seems sensible to use these two metrics to classify whether the breath-hold was successfully maintained or not. These metrics are straightforward to compute and would enable a fast, lightweight evaluation during

treatment, facilitating a more detailed analysis of potential dose changes post-treatment.

5.3.4. Correlation of Carbon and Helium Range Changes

When using helium as a range probe for the carbon ion beam, a challenge arises because the helium range is sensitive to anatomical changes distal of the tumor which do not effect the carbon range, as shown in fig. 4.25. Dick et al. (2024) investigates the use of a deep learning model to infer the carbon range from the helium range for lung patients. For estimated range changes below 10 mm, they can predict the carbon range with an accuracy better than 1 mm in 50 % of the spots.

Another potential method to evaluate the origin of the range change is *focus stacking*. The reconstruction in this thesis calculated the position of the particle in the iso-center plane. Contrary to this, focus stacking reconstructs images for different radiological depths in the object, whereby the spatial resolution of a feature is greatest for an image reconstructed at its radiological depth. Volz et al. (2024) used focus stacking to improve the spatial resolution of radiographs as well as to extract the depth position of a feature. This could possible be used to determine whether the observed WET change occurred proximal or distal of the tumor.

5.3.5. Dose Reconstruction

A potential application of the mixed beam method is dose reconstruction based on the acquired radiographs. This thesis presented one pathway in the context of positioning verification, where the dose was approximated by finding the closest pre-simulated scenario. By estimating the delivered dose, the total dose could be accumulated for further quality assurance. Additionally, if necessary, this information could be used for re-optimization of the treatment plan taking into account the already delivered dose , which could be implemented as part of a more comprehensive evaluation.

To support this, biomedical models, such as those used in image registration by Teske et al. (2017) and Bauer et al. (2023) for head and neck motion, can be employed to evaluate realistic motion scenarios. These models incorporate accurate representations of bone movement and soft tissue deformation (Brock et al., 2005). In combination with the evaluation of SEHeRad between the delivery of IES, these scenario-based dose calculations could enable an estimate of the delivered dose, which in turn could serve as a tool to determine whether the currently delivered dose remains acceptable. However, evaluating a wide range of motion scenarios along with their corresponding dose can quickly become computationally expensive.

Another possibility would be the deformation of the CT based on the radiograph and then recalculating the dose on said deformed CT. Miura et al. (2022) presents a supervised deep learning based framework for deformable image registration between DRR and

abdominal CT images. In this approach, the CT of the current motion phase is reconstructed using the CT of the reference phase and DRR of both the reference and current motion phase. This framework could potentially be adapted to mixed beam radiographs to estimate patient anatomy during irradiation.

Mixed beam radiographs introduce additional complexity due to their small field of view, compared to conventional radiographs. This smaller field of view provides less anatomical information for image registration. However, for dose recalculation, the focus is primary on the volume surrounding the beam, rather entire volume covered by a full field of view radiograph.

6

Conclusion and Outlook

This thesis presents a first investigation into the potential application of mixed-beams for online treatment verification. This is achieved by developing a full mixed-beam planning framework. Using the planning framework, several key modes of potential mixed-beam application were investigated. This included applications for potential positioning verification, monitoring inter- and intrafractional changes, especially considering breathing in the lung, and dose reconstruction. Further, the range of applicability due to limitations in the mixed-in helium range was investigated and mitigation strategies were proposed.

The developed simulation framework includes a simulation pipeline for TOPAS capable of simulating and reconstruct helium radiographs. While this framework was initially tailored to the HIT beam delivery system and ProtonVDA imaging detectors, the framework's adaptability allows for extension to various ion therapy devices and different imaging detectors as well as reconstruction equipment. The framework includes a developed helium pencil-beam kernel set, derived from an existing carbon kernel set, enabling fast pencil beam dose calculation. The separate contribution of helium and carbon to the total dose, as well as different mixing ratios were investigated. For all treatment plans an additional helium fluence of 10 % resulted in less than 1 % contribution to the integrated carbon-helium RBE weighted dose.

The residual helium range in mixed beam treatment plans was evaluated across several beam angles in lung cases, as well as in a prostate and a liver case, revealing that the helium range was too low in most scenarios. Three different strategies were applied to ensure sufficient helium range. The EW–He strategy uses a mixed carbon-helium beam only for energies with sufficient helium range, otherwise a pure carbon beam is used. The Const–RS and EW–RS incorporate proximal and distal range shifters to ensure sufficient helium range while also optimizing detection capabilities by incorporating the sensitive range of the detector in the selection of the range shifters. Overall, all evaluated residual helium range strategies successfully ensure sufficient helium range. Strategies involving range shifters further increase the number of detectable spots. These strategies allow more flexibility in the chosen treatment angle and increase the clinical usability of the mixed carbon-helium beam method.

Mixed carbon-helium beams, were explored as a method to reconstruct the patient posi-

tion from previously calculated error scenarios. Hereby, it seems that dose reconstruction by comparison with precalculated error scenarios is possible. Additionally, the framework was applied to assess breath-hold verification in lung treatment plans. Generally, the mixed carbon-helium beam method shows promising results for range verification, providing online beams-eye-view information.

As part of a project connected to this treatment planning investigation, first helium images of an anthropomorphic phantom acquired with the ProtonVDA detector could be presented. These results demonstrate the feasibility of helium imaging with existing technology, but also reveal that significant experimental development is still required for a clinical mixed beam detector.

Further work in the mixed beam field will focus on a clinical acceptable acceleration of the mixed carbon-helium beam, implementing scanning of the beam and investigating the inter and intra spill variability of the helium fluence. These advancements will enable studies using a truly mixed beam, rather than the sequential irradiation employed so far, thereby facilitating the optimization of a dedicated mixed beam detector. The developed framework provides a foundation for exploring the mixed beam method in larger treatment planning studies, investigating the correlation of helium range changes to carbon range changes, the resulting dose differences and the development of automated triggers to interrupt the treatment delivery. Furthermore dose reconstruction based on mixed beam radiographs, can be investigated as well was dose accumulation over several fractions and replanning strategies.

This thesis demonstrated that mixed beams can offer a benefit for both online range probing and retrospective treatment verification. Together with the first successfully generated mixed beams, this approach could be applied clinically given the availability of an appropriate detector.

A

Suplementary Material

A.1. Supplementary to Helium Radiography Measurements

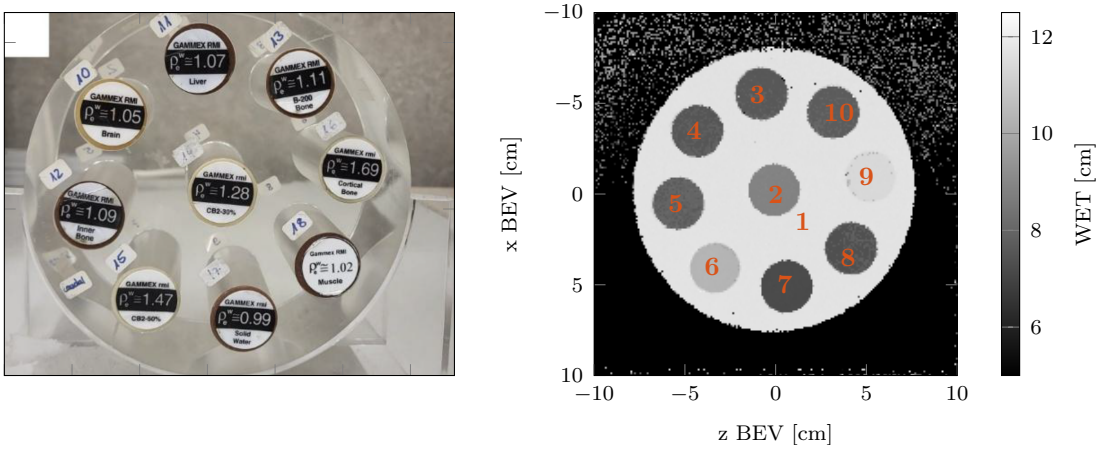

Figure A.1.: Left: Gammex phantom with tissue inserts. Right: Acquired helium radiograph. Annotated is the ID number of the insert used in table 4.1.

Figure A.2.: The BRaViDA phantom, used for anthropomorphic measurements, adapted from Bakhtiari Moghaddam (2022)

A.2. Summary of parameters used in the treatment plans

The following section provides an overview of the parameter used in creation of the treatment plans. For all plans expect for the prostate the lateral spot spacing was 2 mm, for the prostate it was set to 3 mm. For all plans the bixel width was 5 mm, the rotation of the patient couch was 0° and the dose was calculated on a 3 mm^2 grid. Furthermore the number of fractions was allways set to 30 and the mixing ratio of helium in the carbon beam was 0.1. Additionally the optimization was always performed on the carbon RBE weighted dose, for the Box Phantom an additional optimization on the carbon-helium RBE weighted dose was performed.

The simulation of an entire treatment plan was performed with 1×10^7 histories, if a single energy of a treatment plan was simulated the simulation was performed with 1×10^6 histories. And simulations were perforemed with the following physics lists: G4DecayPhysics, G4StoppingPhysics, G4EmExtraPhysics, G4EMStandardPhysics_option4, G4HadronElasticPhysics, g4h-phy_QGSP_BIC_HP and G4QMDReaction physics. To accurately model helium ions G4BinaryLightIonReaction was activated with the Tripathi cross section data (Tripathi et al., 1999) as modified by Horst et al. (2019).

During this thesis the Schneider et al. (2000) material converter implemented by TOPAS was used to convert the HU unit values of the CT into materials used in the simulation. Additionally with an extension to TOPAS [1] the HU to RSP conversion for this conversion was extracted for 200 MeV protons.

The following table summarizes the optimization settings, hereby the objective function with a relative weight of $p = 100$ and a persribed dose of $d = 2$Gy per fraction is abbreviated as SD(100,2) . Similarly the squared overdosing objective function is abbreviated as SO(100,2). The objective functions are described in section 2.4.2.

Squared Deviation:

$$\mathcal{F}^{SD}(d) = \frac{1}{N_S} \sum_{i \in S} (d_i - d^\star)^2 \,, \tag{A.1}$$

Squared Over and Underdosing:

$$\mathcal{F}^{OD}(d) = \frac{1}{N_S} \sum_{i \in S} \Theta(d_i - d^{max})(d_i - d^{max})^2 \,, \tag{A.2}$$

$$\mathcal{F}^{UD}(d) = \frac{1}{N_S} \sum_{i \in S} \Theta(d^{min} - d_i)(d_i - d^{min})^2 \,, \tag{A.3}$$

[1] https://github.com/topasmc/extensions/tree/master/HU, visited on 05/07/2025

Patient	Angles [°]	Opimization settings		Helium range strategy
Box Phantom with Bone Insert	0	PTV Body	SD(800, 2.00) SO(100, 0.30)	none
Box Phantom	0	PTV Body	SD(800, 2.00) SO(100, 0.17)	Const RS, pre set to $x^P = 45\,\text{cm}, x^D = 0\,\text{cm}$
Prostate	90, 270	PTV_{68} PTV_{56} Bladder Rectum Body	SD(1000,2.27) SD(1000,1.86) SO(300, 1.67) SO(300, 2.67) SO(100, 1.00)	EW RS
Lung P114	270	PTV Heart Body	SD(1500, 2.33) SO(1000, 1.33) SO(3000, 1.33)	none, EW He Const RS, EW RS
Lung P114	0	PTV Heart Body	SD(1500, 2.33) SO(1000, 1.33) SO(3000, 1.33)	EW RS

Table A.1.: Overview of parameters used in the calculation of the treatment plan. The objective function squared deviation is abbreviatied with SD, the objective function squared overdosing with SO

A.3. Supplementary to Helium Machine Data Kernel Set

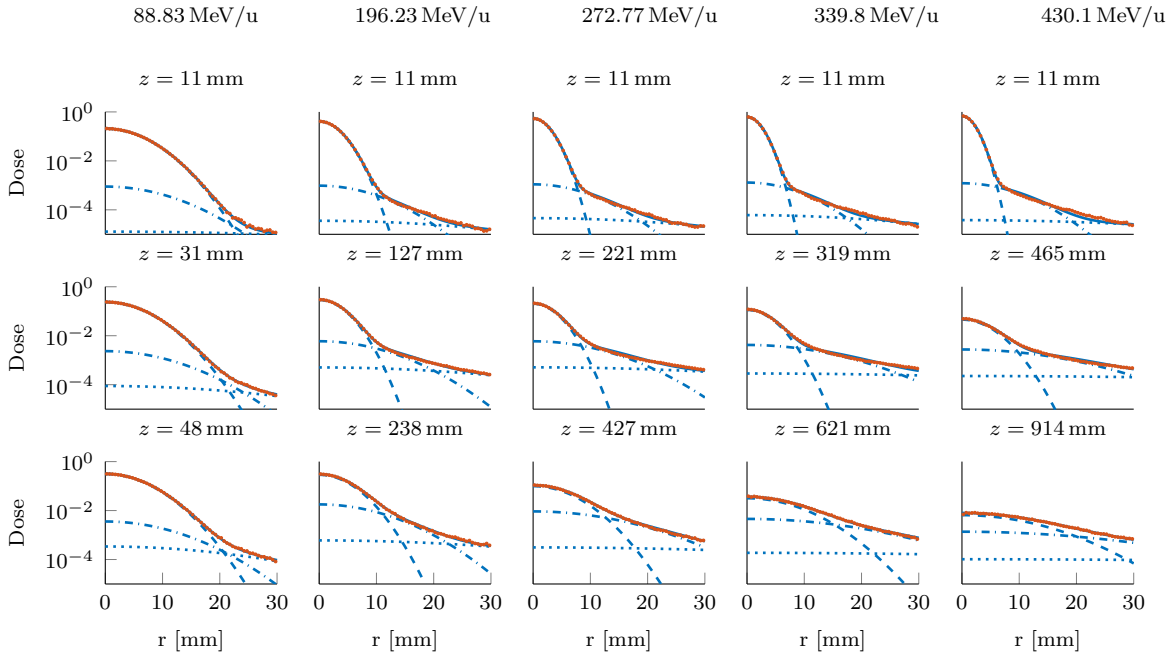

Figure A.3.: Lateral dose profiles for several energies and depths. The top row is close to the entrance, the middle row approximately on the mid point way of the helium range bottom row shortly before the peak. Displayed is the monte carlo data (●) the latteral fit (——) aswell as the first (- - -) second (-·-·-) and third (·····) component.

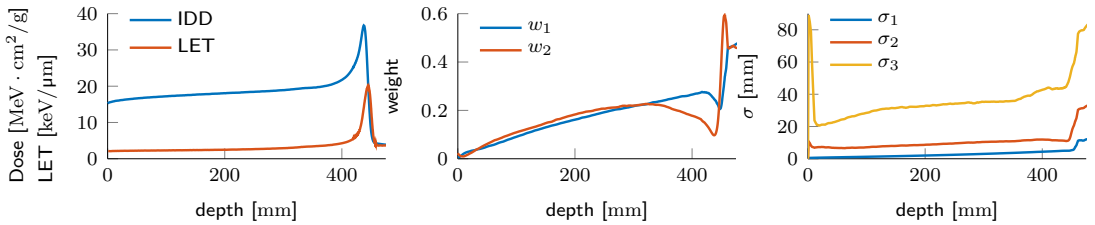

Figure A.4.: Example trends in depth of the lateral kernel data for 272.77 MeV/u. Left: integrated depth dose curves and LET, middle: fitted weight parameter w of the triple gaussian function, right: fitted σ.

A.4. Supplementary to Comparison of Residual Helium Range Strategies

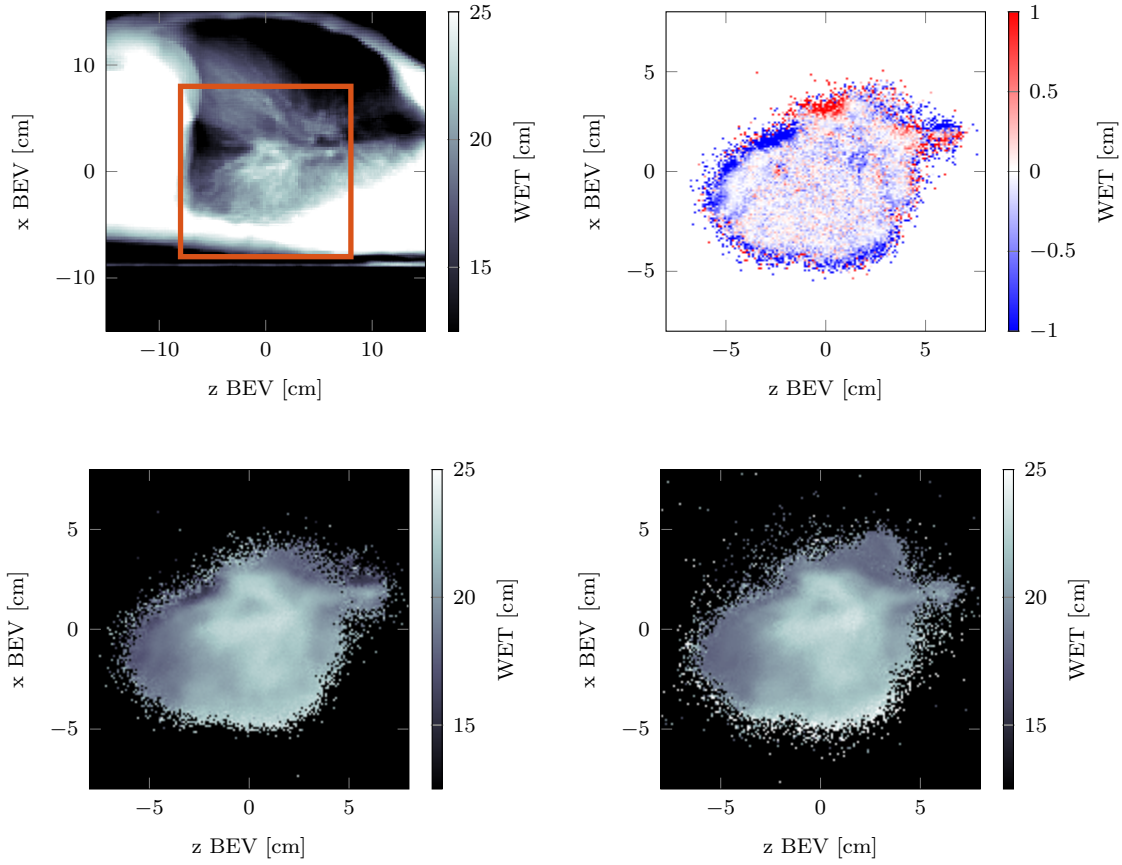

Figure A.5.: Top Left projected CT highlighted is the area (——) shown in the other figures. Bottom left: simulated helium radiograph (197.58 MeV/u, 0 cm). Bottom right simulated helium radiograph (217.25 MeV/u, 1.5 cm). Top right: Difference Image of both radiographs

A.5. Supplementary to Intrafractional Motion

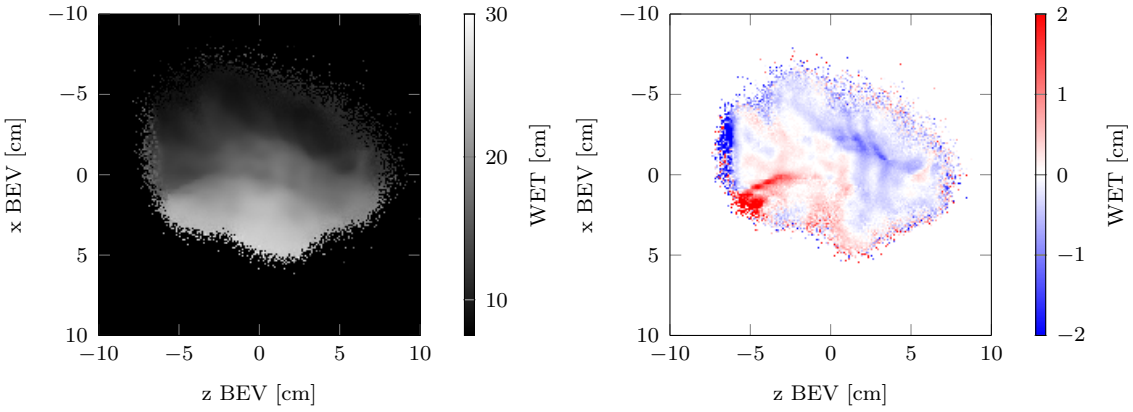

Figure A.6.: Simulated FEHeRad of Day 0 ($R^{\mathrm{maxD}} = 160\,\mathrm{mm}$). Left: Phase 0, right: difference of phase 0 to phase 1.

In the following BH indicates where breath-hold was maintained during irradiation of the IES, i.e both radiographs are delivered in the same motion phase. BH failed indicates where breath-hold could not be maintained the entire irradiation, therefore the motion phase of one radiograph changes during irradiation. Overlayed is the spot scanning pattern and the point at which the BH failed. Bottom row: Corresponding absolute difference of the mean WEPL and standard error of each spot for both irradiation's. Highlighted in green are the spots delivered in the same phase. The comparison is performed for spots belonging to the same ray and exceeding more than 100 events. The threshold value of 0.75 cm is visualized, this threshold could be used for online BH verification.

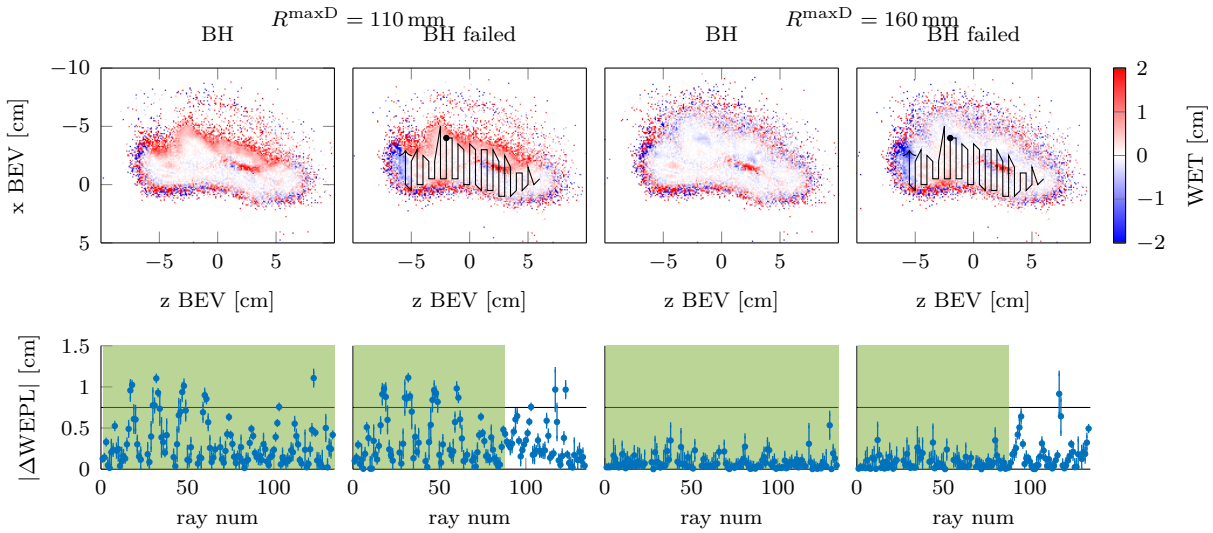

Figure A.7.: BH difference of simulated SEHeRad $E = 218.52\,\mathrm{MeV/u}, x^P = 45\,\mathrm{mm}$ to $E = 222.31\,\mathrm{MeV/u}, x^P = 45\,\mathrm{mm}$.

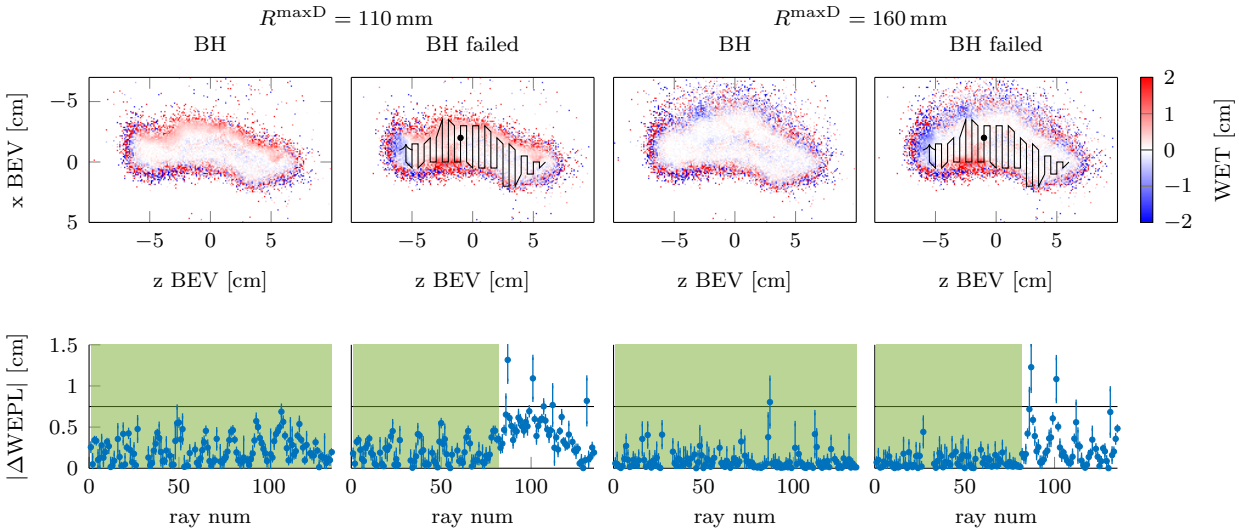

Figure A.8.: BH difference of simulated SEHeRad $E = 221.05\,\mathrm{MeV/u}, x^P = 35\,\mathrm{mm}$ to $E = 223.56\,\mathrm{MeV/u}, x^P = 35\,\mathrm{mm}$.

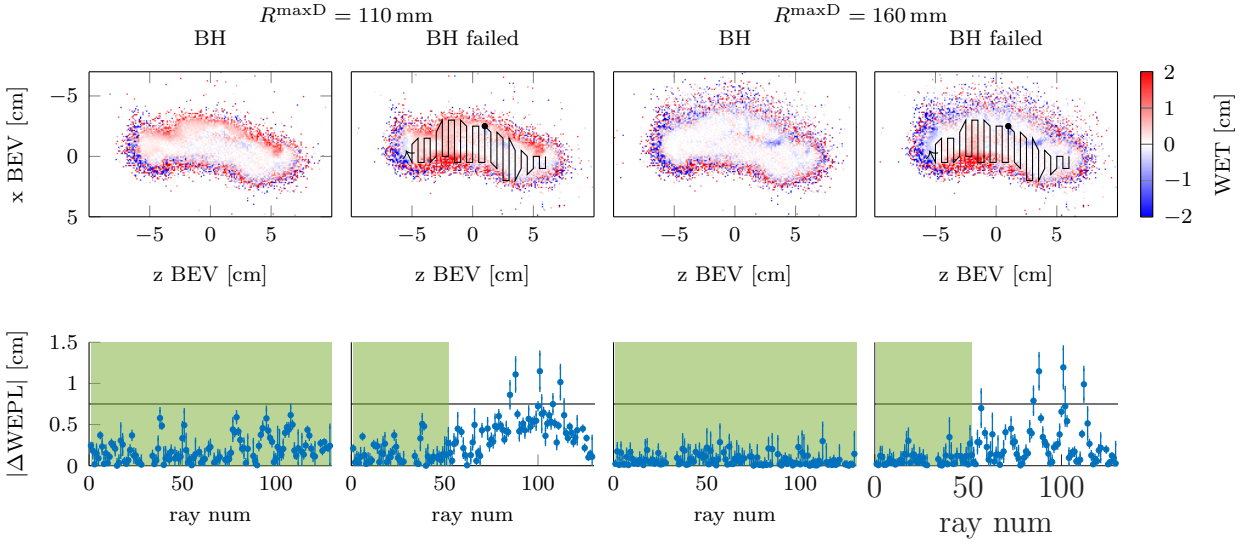

Figure A.9.: BH difference of simulated SEHeRad $E = 218.52\,\mathrm{MeV/u}, x^P = 25\,\mathrm{mm}$ to $E = 221.05\,\mathrm{MeV/u}, x^P = 25\,\mathrm{mm}$.

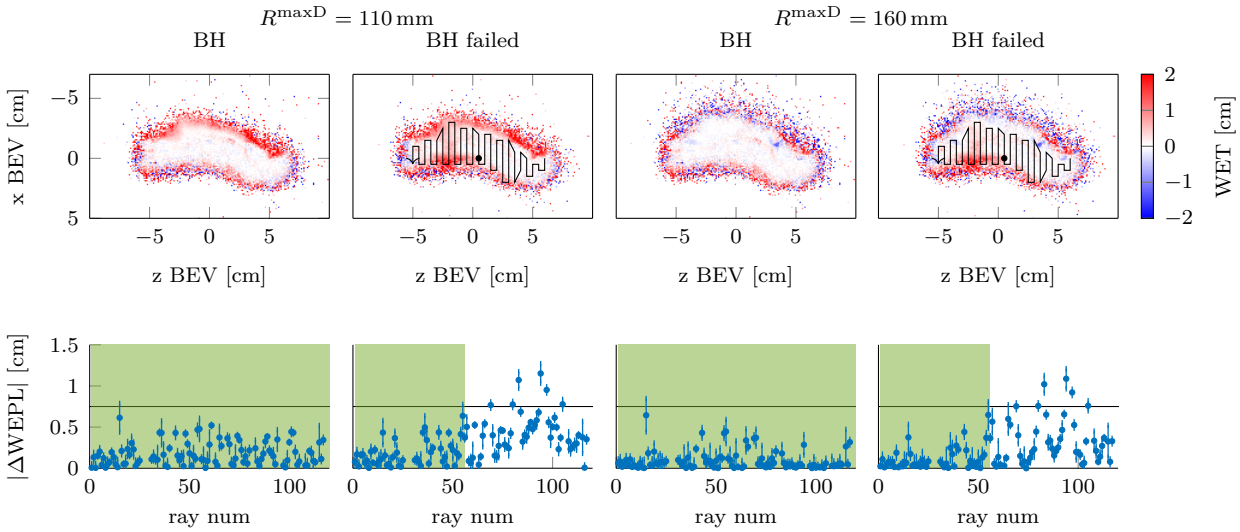

Figure A.10.: BH difference of simulated SEHeRad $E = 210.83\,\mathrm{MeV/u}, x^P = 15\,\mathrm{mm}$ to $E = 214.70\,\mathrm{MeV/u}, x^P = 15\,\mathrm{mm}$.

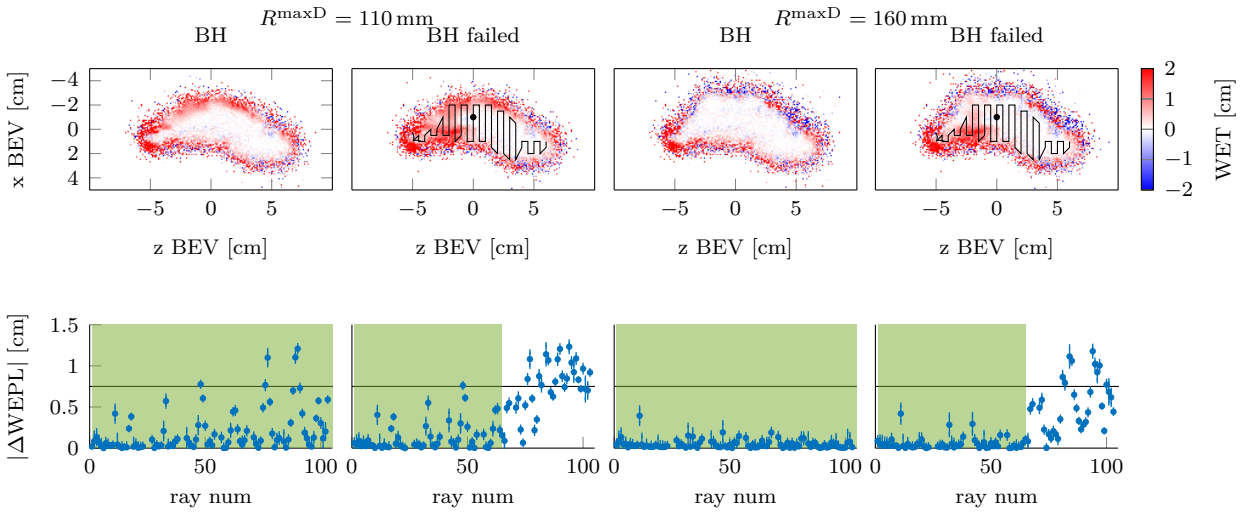

Figure A.11.: BH difference of simulated SEHeRad $E = 214.70\,\mathrm{MeV/u}, x^P = 5\,\mathrm{mm}$ to $E = 218.52\,\mathrm{MeV/u}, x^P = 5\,\mathrm{mm}$.

List of Figures

List of Tables

Bibliography

Abbani, N., N. Al-Hasnawi, B. Ackermann, et al. (Nov. 18, 2024). *matRad*. Version v3.1.0. DOI: 10.5281/zenodo.14181851. URL: https://zenodo.org/records/14181851 (cit. on pp. 4, 14, 35, IX, XXIX).

Agostinelli, S., J. Allison, K. Amako, et al. (July 1, 2003). "Geant4—a simulation toolkit". In: *Nuclear Instruments and Methods in Physics Research Section A: Accelerators, Spectrometers, Detectors and Associated Equipment* 506.3, pp. 250–303. ISSN: 0168-9002. DOI: 10.1016/S0168-9002(03)01368-8 (cit. on pp. 15, 36).

Allison, J., K. Amako, J. Apostolakis, et al. (Nov. 1, 2016). "Recent developments in Geant4". In: *Nuclear Instruments and Methods in Physics Research Section A: Accelerators, Spectrometers, Detectors and Associated Equipment* 835, pp. 186–225. ISSN: 0168-9002. DOI: 10.1016/j.nima.2016.06.125 (cit. on pp. 15, 36).

Anetai, Y., I. Sumida, Y. Kumazaki, et al. (2022). "Assessment of using a gamma index analysis for patient-specific quality assurance in Japan". In: *Journal of Applied Clinical Medical Physics* 23.10, e13745. ISSN: 1526-9914. DOI: 10.1002/acm2.13745 (cit. on p. 18).

Arbor, N., D. Dauvergne, G. Dedes, et al. (Sept. 2015). "Monte Carlo comparison of x-ray and proton CT for range calculations of proton therapy beams". In: *Physics in Medicine & Biology* 60.19, p. 7585. ISSN: 0031-9155. DOI: 10.1088/0031-9155/60/19/7585 (cit. on p. 25).

Bakhtiari Moghaddam, A. (2022). "Herstellung eines 4D-Phantoms fur ¨ AlignRT-System BRaViDA". Master Thesis. Heidelberg University (cit. on pp. 26, I, XIII).

Bakhtiari Moghaddam, A., C. P. Karger, P. Häring, et al. (Sept. 1, 2024). "PP18.07 BRAVIDA: A Dynamic Anthopomorphic Phantom for End-to-End Testing in Advanced Radiotherapy". In: *Physica Medica*. Abstracts of the 5th European Congress of Medical Physics 125, p. 103711. ISSN: 1120-1797. DOI: 10.1016/j.ejmp.2024.103711 (cit. on p. 26).

Bashkirov, V. A., R. W. Schulte, R. F. Hurley, et al. (2016). "Novel scintillation detector design and performance for proton radiography and computed tomography". In: *Medical Physics* 43.2, pp. 664–674. ISSN: 2473-4209. DOI: 10.1118/1.4939255 (cit. on p. 76).

Bauer, C. J., H. Teske, A. Walter, et al. (Apr. 19, 2023). "Biofidelic image registration for head and neck region utilizing an in-silico articulated skeleton as a transformation model". In: *Physics in Medicine and Biology* 68.9. ISSN: 1361-6560. DOI: 10.1088/1361-6560/acc7f1 (cit. on p. 85).

Berger, M., J. Coursey, M. Zucker, and J. Chang (Oct. 7, 2009). "Stopping-Power & Range Tables for Electrons, Protons, and Helium Ions". In: *NIST*. DOI: https://dx.doi.org/10.18434/T4NC7P (cit. on pp. 4, 16, 51, 52, IX, X).

Berger, M. (1963). "Monte Carlo calculation of the penetration and diffusion of fast charged particles". In: *Methods in Computational Physics: Advances in Research and Applications* 1 (cit. on p. 15).

Bethe, H. (1930). "Zur Theorie des Durchgangs schneller Korpuskularstrahlen durch Materie". In: *Annalen der Physik* 397.3, pp. 325–400. ISSN: 1521-3889. DOI: 10.1002/andp.19303970303 (cit. on p. 5).

Bloch, F. (1933). "Zur Bremsung rasch bewegter Teilchen beim Durchgang durch Materie". In: *Annalen der Physik* 408.3, pp. 285–320. ISSN: 1521-3889. DOI: 10.1002/andp.19334080303 (cit. on p. 5).

Bortfeld, T. (Dec. 1997). "An analytical approximation of the Bragg curve for therapeutic proton beams". In: *Medical Physics* 24.12, pp. 2024–2033. ISSN: 0094-2405. DOI: 10.1118/1.598116 (cit. on p. 16).

Brock, K. K., M. B. Sharpe, L. A. Dawson, S. M. Kim, and D. A. Jaffray (2005). "Accuracy of finite element model-based multi-organ deformable image registration". In: *Medical Physics* 32.6, pp. 1647–1659. ISSN: 2473-4209. DOI: 10.1118/1.1915012 (cit. on p. 85).

Bronk, L., F. Guan, D. Patel, et al. (Dec. 5, 2020). "Mapping the Relative Biological Effectiveness of Proton, Helium and Carbon Ions with High-Throughput Techniques". In: *Cancers* 12.12, p. 3658. ISSN: 2072-6694. DOI: 10.3390/cancers12123658 (cit. on p. 78).

Cirrone, P. and G. Petringa (2023). *Monte Carlo in Heavy Charged Particle Therapy: New Challenges in Ion Therapy*. Milton, UNITED KINGDOM: Taylor & Francis Group. ISBN: 978-1-000-98761-4 (cit. on p. 15).

Courant, E. D. and H. S. Snyder (1958). "Theory of the alternating-Gradient Synchrotron". In: *Ann Phys* (cit. on pp. 16, 27).

Craft, D., M. Bangert, T. Long, D. Papp, and J. Unkelbach (Dec. 1, 2014). "Shared data for intensity modulated radiation therapy (IMRT) optimization research: the CORT dataset". In: *GigaScience* 3.1, pp. 2047–217X–3–37. ISSN: 2047-217X. DOI: 10.1186/2047-217X-3-37 (cit. on pp. 30, 47).

Cristoforetti, R., J. J. Hardt, and N. Wahl (Jan. 10, 2025). *Scenario-free robust optimization algorithm for IMRT and IMPT treatment planning*. DOI: 10.48550/arXiv.2501.05818. arXiv: 2501.05818[physics]. URL: http://arxiv.org/abs/2501.05818 (cit. on p. 19).

DeJongh, E. A., D. F. DeJongh, I. Polnyi, et al. (Mar. 2021). "Technical Note: A fast and monolithic prototype clinical proton radiography system optimized for pencil beam scanning". In: *Medical physics* 48.3, pp. 1356–1364. ISSN: 0094-2405. DOI: 10.1002/mp.14700 (cit. on pp. 13, 23, 24).

Deng, L., Y. Zhang, J. Qi, et al. (2023). "Enhancement of cone beam CT image registration by super-resolution pre-processing algorithm". In: *Mathematical Biosciences and Engineering* 20.3, pp. 4403–4420. ISSN: 1551-0018. DOI: 10.3934/mbe.2023204 (cit. on p. 43).

Destatis (2024). *Todesursachen in Deutschland 2023*. Statistisches Bundesamt (cit. on p. 1).

Dick, M., L. Volz, M. Durante, and C. Graeff (June 1, 2024). "SO050 / #858 - RANGE PREDICTION FOR A MIXED HELIUM-CARBON BEAM". In: *International Journal of Particle Therapy*. Proceedings to the 62nd Annual Conference of the Particle Therapy Cooperative Group (PTCOG) 12, p. 100362. ISSN: 2331-5180. DOI: 10.1016/j.ijpt.2024.100362 (cit. on p. 85).

Dida, H., F. Charif, and A. Benchabane (2022). "Image registration of computed tomography of lung infected with COVID-19 using an improved sine cosine algorithm". In: *Medical & Biological Engineering & Computing* 60.9, pp. 2521–2535. ISSN: 0140-0118. DOI: 10.1007/s11517-022-02606-z (cit. on p. 43).

Doerner, E. and P. Caprile (June 5, 2018). "Technical Note: An hybrid parallel implementation for EGSnrc Monte Carlo user codes". In: *Medical Physics*. ISSN: 2473-4209. DOI: 10.1002/mp.13033 (cit. on p. 35).

Durante, M., R. Orecchia, and J. S. Loeffler (Aug. 2017). "Charged-particle therapy in cancer: clinical uses and future perspectives". In: *Nature Reviews Clinical Oncology* 14.8, pp. 483–495. ISSN: 1759-4782. DOI: 10.1038/nrclinonc.2017.30 (cit. on p. 9).

Durante, M. and H. Paganetti (Aug. 2016). "Nuclear physics in particle therapy: a review". In: *Reports on Progress in Physics* 79.9, p. 096702. ISSN: 0034-4885. DOI: 10.1088/0034-4885/79/9/096702 (cit. on p. 6).

Eyges, L. (Nov. 15, 1948). "Multiple Scattering with Energy Loss". In: *Physical Review* 74.10, pp. 1534–1535. DOI: 10.1103/PhysRev.74.1534 (cit. on p. 6).

Facchiano, S., R. Ortiz, R. Cristoforetti, et al. (2025). "An ion treatment planning framework for inclusion of nanodosimetric ionization detail through cluster dose". In: *Currently in preparation for publication* (cit. on p. 75).

Faddegon, B., J. Ramos-Méndez, J. Schuemann, et al. (Apr. 2020). "The TOPAS tool for particle simulation, a Monte Carlo simulation tool for physics, biology and clinical research". In: *Physica medica: PM: an international journal devoted to the applications of physics to medicine and biology: official*

journal of the Italian Association of Biomedical Physics (AIFB) 72, pp. 114–121. ISSN: 1724-191X. DOI: 10.1016/j.ejmp.2020.03.019 (cit. on pp. 16, 35, 36).

Fedorov, A., R. Beichel, J. Kalpathy-Cramer, et al. (Nov. 2012). "3D Slicer as an Image Computing Platform for the Quantitative Imaging Network". In: *Magnetic resonance imaging* 30.9, pp. 1323–1341. ISSN: 0730-725X. DOI: 10.1016/j.mri.2012.05.001 (cit. on p. 46).

Fekete, C.-A. C., P. Doolan, M. F. Dias, L. Beaulieu, and J. Seco (June 2015). "Developing a phenomenological model of the proton trajectory within a heterogeneous medium required for proton imaging". In: *Physics in Medicine & Biology* 60.13, p. 5071. ISSN: 0031-9155. DOI: 10.1088/0031-9155/60/13/5071 (cit. on p. 41).

Fowler, J. F. (1989). "The linear-quadratic formula and progress in fractionated radiotherapy". In: *British Journal of Radiology* 62.740. DOI: https://doi.org/10.1259/0007-1285-62-740-679 (cit. on p. 29).

Fullarton, R., M. Simard, L. Volz, et al. (Feb. 2025). "Imaging lung tumor motion using integrated-mode proton radiography—A phantom study towards tumor tracking in proton radiotherapy". In: *Medical Physics* 52.2, pp. 1146–1158. ISSN: 0094-2405. DOI: 10.1002/mp.17508 (cit. on p. 76).

Galonska, M., W. Barth, C. Graeff, et al. (2024). "First dual isotope beam production for simultaneous heavy ion radiotherapy and radiography". In: *JACoW* IPAC2024, WEAN1. DOI: 10.18429/JACoW-IPAC2024-WEAN1" (cit. on p. 10).

Geant4-Colloberation (2024). "Book For Application Developers". In: 11 (cit. on p. 27).

Gehrke, T., C. Amato, S. Berke, and M. Martišíková (Feb. 5, 2018a). "Theoretical and experimental comparison of proton and helium-beam radiography using silicon pixel detectors". In: *Physics in Medicine & Biology* 63.3, p. 035037. ISSN: 0031-9155. DOI: 10.1088/1361-6560/aaa60f (cit. on pp. 6, 13).

Gehrke, T., R. Gallas, O. Jäkel, and M. Martišíková (Feb. 2018b). "Proof of principle of helium-beam radiography using silicon pixel detectors for energy deposition measurement, identification, and tracking of single ions". In: *Medical Physics* 45.2, pp. 817–829. ISSN: 2473-4209. DOI: 10.1002/mp.12723 (cit. on p. 76).

Giacometti, V., A. R. Hounsell, and C. K. McGarry (Aug. 1, 2020). "A review of dose calculation approaches with cone beam CT in photon and proton therapy". In: *Physica Medica* 76, pp. 243–276. ISSN: 1120-1797. DOI: 10.1016/j.ejmp.2020.06.017 (cit. on p. 46).

Gillin, M. T., N. Sahoo, M. Bues, et al. (Jan. 2010). "Commissioning of the discrete spot scanning proton beam delivery system at the University of Texas M.D. Anderson Cancer Center, Proton Therapy Center, Houston". In: *Medical Physics* 37.1, pp. 154–163. ISSN: 0094-2405. DOI: 10.1118/1.3259742 (cit. on p. 32).

GitHub (2025). *GitHub Copilot*. URL: https://github.com/features/copilot (visited on 05/10/2025) (cit. on p. xi).

Graeff, C., L. Volz, M. C. Martire, et al. (June 1, 2024). "O072 / #772 - First experimental production of a mixed carbon/helium beam for online range monitoring and image guidance". In: *International Journal of Particle Therapy*. Proceedings to the 62nd Annual Conference of the Particle Therapy Cooperative Group (PTCOG) 12, p. 100185. ISSN: 2331-5180. DOI: 10.1016/j.ijpt.2024.100185 (cit. on pp. 2, 10, 27).

Graeff, C., U. Weber, C. Schuy, et al. (Aug. 1, 2018). "[OA027] Helium as a range probe in carbon ion therapy". In: *Physica Medica*. Abstracts from the 2nd European Congress of Medical Physics 52, p. 11. ISSN: 1120-1797. DOI: 10.1016/j.ejmp.2018.06.099 (cit. on p. 2).

Grün, R., T. Friedrich, M. Krämer, et al. (2015). "Assessment of potential advantages of relevant ions for particle therapy: A model based study". In: *Medical Physics* 42.2, pp. 1037–1047. ISSN: 2473-4209. DOI: 10.1118/1.4905374 (cit. on p. 78).

Hanley, J., M. M. Debois, D. Mah, et al. (Oct. 1, 1999). "Deep inspiration breath-hold technique for lung tumors: the potential value of target immobilization and reduced lung density in dose escalation". In: *International Journal of Radiation Oncology*Biology*Physics* 45.3, pp. 603–611. ISSN: 0360-3016. DOI: 10.1016/S0360-3016(99)00154-6 (cit. on p. 21).

Hardt, J. J., A. A. Pryanichnikov, N. Homolka, et al. (2024). "The potential of mixed carbon-helium beams for online treatment verification: a simulation and treatment planning study". In: *Physics in Medicine and Biology*. ISSN: 0031-9155. DOI: 10.1088/1361-6560/ad46db (cit. on pp. xi, 42–44, 63).

Hardt, J. J., A. A. Pryanichnikov, O. Jäkel, J. Seco, and N. Wahl (May 2, 2025). *Helium Range Viability for Online Range Probing in Mixed Carbon-Helium Beams*. DOI: 10.48550/arXiv.2505.01165. URL: http://arxiv.org/abs/2505.01165 (cit. on pp. xi, 30, 31, 35, 57).

Hoffmann, A., B. Oborn, M. Moteabbed, et al. (May 29, 2020). "MR-guided proton therapy: a review and a preview". In: *Radiation Oncology* 15.1, p. 129. ISSN: 1748-717X. DOI: 10.1186/s13014-020-01571-x (cit. on pp. 21, 82).

Hong, L., M. Goitein, M. Bucciolini, et al. (Aug. 1, 1996). "A pencil beam algorithm for proton dose calculations". In: *Physics in Medicine & Biology* 41.8, p. 1305. ISSN: 0031-9155. DOI: 10.1088/0031-9155/41/8/005 (cit. on pp. 14, 35).

Horst, F., G. Aricò, K.-T. Brinkmann, et al. (Jan. 7, 2019). "Measurement of He 4 charge- and mass-changing cross sections on H, C, O, and Si targets in the energy range 70–220 MeV/u for radiation transport calculations in ion-beam therapy". In: *Physical Review C* 99.1, p. 014603. ISSN: 2469-9985, 2469-9993. DOI: 10.1103/PhysRevC.99.014603 (cit. on pp. 36, II).

Huang, S., M. Kang, K. Souris, et al. (2018). "Validation and clinical implementation of an accurate Monte Carlo code for pencil beam scanning proton therapy". In: *Journal of Applied Clinical Medical Physics* 19.5, pp. 558–572. ISSN: 1526-9914. DOI: 10.1002/acm2.12420 (cit. on p. 16).

Hugo, G. D., E. Weiss, W. C. Sleeman, et al. (2016). *Data from 4D Lung Imaging of NSCLC Patients (Version 2) [Data set]*. DOI: https://doi.org/10.7937/K9/TCIA.2016.ELN8YGLE. URL: https://doi.org/10.7937/K9/TCIA.2016.ELN8YGLE (cit. on pp. 30, 47).

Hünemohr, N., B. Krauss, C. Tremmel, B. Ackermann, O. Jäkel, and S. Greilich (Dec. 2013). "Experimental verification of ion stopping power prediction from dual energy CT data in tissue surrogates". In: *Physics in Medicine & Biology* 59.1, p. 83. ISSN: 0031-9155. DOI: 10.1088/0031-9155/59/1/83 (cit. on p. 26).

Jäkel, O. (Nov. 1, 2009). "Medical physics aspects of particle therapy". In: *Radiation Protection Dosimetry* 137.1, pp. 156–166. ISSN: 0144-8420. DOI: 10.1093/rpd/ncp192 (cit. on p. 9).

Jäkel, O. (Mar. 2020). "Physical advantages of particles: protons and light ions". In: *The British Journal of Radiology* 93.1107, p. 20190428. ISSN: 0007-1285. DOI: 10.1259/bjr.20190428 (cit. on pp. 1, 7).

Kausel, M., C. Schmitzer, A. Gsponer, et al. (Jan. 22, 2025). *A double multi-turn injection scheme for generating mixed helium and carbon ion beams at medical synchrotron facilities*. DOI: 10.48550/arXiv.2501.12797. arXiv: 2501.12797[physics]. URL: http://arxiv.org/abs/2501.12797 (cit. on pp. 2, 10, 11, 27).

Kellerer, L., R. Radogna, L. Volz, et al. (Aug. 2020). "A scintillator-based range telescope for particle therapy". In: *Physics in Medicine & Biology* 65.16, p. 165001. ISSN: 0031-9155. DOI: 10.1088/1361-6560/ab9415 (cit. on p. 2).

Korevaar, E. W., S. J. M. Habraken, D. Scandurra, et al. (Dec. 1, 2019). "Practical robustness evaluation in radiotherapy – A photon and proton-proof alternative to PTV-based plan evaluation". In: *Radiotherapy and Oncology* 141, pp. 267–274. ISSN: 0167-8140. DOI: 10.1016/j.radonc.2019.08.005 (cit. on p. 44).

Krah, N., D. Dauvergne, J. M. Létang, S. Rit, and É. Testa (Aug. 2022). "Relative stopping power resolution in time-of-flight proton CT". In: *Physics in Medicine & Biology* 67.16, p. 165004. ISSN: 0031-9155. DOI: 10.1088/1361-6560/ac7191 (cit. on p. 77).

Krah, N., F. Khellaf, J. M. Létang, S. Rit, and I. Rinaldi (July 2, 2018). "A comprehensive theoretical comparison of proton imaging set-ups in terms of spatial resolution". In: *Physics in Medicine & Biology* 63.13, p. 135013. ISSN: 1361-6560. DOI: 10.1088/1361-6560/aaca1f (cit. on pp. 12, 13, 42).

Kraus, K. M., E. Heath, and U. Oelfke (Sept. 2011). "Dosimetric consequences of tumour motion due to respiration for a scanned proton beam". In: *Physics in Medicine & Biology* 56.20, p. 6563. ISSN: 0031-9155. DOI: 10.1088/0031-9155/56/20/003 (cit. on p. 19).

Letellier, V., S. Schmidt, O. Cosson, P. F. Doubliez, P. Velten, and M. De Leenheer (Oct. 1, 2023). "Beam Delivery and Patient Alignment: Perspective of the Innovative Cycloton 400MEV/u Multi-Ion System". In: *International Journal of Radiation Oncology*Biology*Physics*. ASTRO 2023: 65th Annual Meeting 117.2, e683. ISSN: 0360-3016. DOI: 10.1016/j.ijrobp.2023.06.2147 (cit. on p. 7).

Liao, Z., J. J. Lee, R. Komaki, et al. (June 20, 2018). "Bayesian Adaptive Randomization Trial of Passive Scattering Proton Therapy and Intensity-Modulated Photon Radiotherapy for Locally Advanced Non–Small-Cell Lung Cancer". In: *Journal of Clinical Oncology* 36.18, pp. 1813–1822. ISSN: 0732-183X. DOI: 10.1200/JCO.2017.74.0720 (cit. on p. 83).

Lomax, A. (Jan. 1999). "Intensity modulation methods for proton radiotherapy". In: *Physics in Medicine & Biology* 44.1, p. 185. ISSN: 0031-9155. DOI: 10.1088/0031-9155/44/1/014 (cit. on p. 14).

Lomax, A. (Feb. 21, 2008). "Intensity modulated proton therapy and its sensitivity to treatment uncertainties 2: the potential effects of inter-fraction and inter-field motions". In: *Physics in Medicine and Biology* 53.4, pp. 1043–1056. ISSN: 0031-9155. DOI: 10.1088/0031-9155/53/4/015 (cit. on p. 43).

Low, D. A., W. B. Harms, S. Mutic, and J. A. Purdy (1998). "A technique for the quantitative evaluation of dose distributions". In: *Medical Physics* 25.5, pp. 656–661. ISSN: 2473-4209. DOI: 10.1118/1.598248 (cit. on p. 18).

Mairani, A., G. Magro, I. Dokic, et al. (Jan. 2016). "Data-driven RBE parameterization for helium ion beams". In: *Physics in Medicine and Biology* 61.2, pp. 888–905. ISSN: 0031-9155. DOI: 10.1088/0031-9155/61/2/888 (cit. on p. 29).

Mairani, A., S. Mein, E. Blakely, et al. (Aug. 5, 2022). "Roadmap: helium ion therapy". In: *Physics in Medicine & Biology* 67.15, 15TR02. ISSN: 0031-9155. DOI: 10.1088/1361-6560/ac65d3 (cit. on p. 80).

MATLAB (2024). Natick, Massachusetts, United States. URL: https://de.mathworks.com/ (cit. on p. 35).

matRad (2025). *Dose influence matrix calculation*. GitHub. URL: https://github.com/e0404/matRad/wiki/Dose-influence-matrix-calculation (visited on 03/02/2025) (cit. on pp. 14, IX).

Mazzucconi, D., S. Agosteo, M. Ferrarini, et al. (2018). "Mixed particle beam for simultaneous treatment and online range verification in carbon ion therapy: Proof-of-concept study". In: *Medical Physics* 45.11, pp. 5234–5243. ISSN: 2473-4209. DOI: 10.1002/mp.13219 (cit. on pp. 2, 77).

Metzner, M., D. Zhevachevska, A. Schlechter, et al. (Feb. 19, 2024). "Energy painting: helium-beam radiography with thin detectors and multiple beam energies". In: *Physics in Medicine and Biology* 69.5. ISSN: 1361-6560. DOI: 10.1088/1361-6560/ad247e (cit. on p. 76).

Miura, R., M. Nakao, M. Nakamura, and T. Matsuda (Dec. 11, 2022). *2D/3D Deep Image Registration by Learning 3D Displacement Fields for Abdominal Organs*. DOI: 10.48550/arXiv.2212.05445. arXiv: 2212.05445[eess]. URL: http://arxiv.org/abs/2212.05445 (cit. on p. 85).

Mori, S., A.-C. Knopf, and K. Umegaki (2018). "Motion management in particle therapy". In: *Medical Physics* 45.11, e994–e1010. ISSN: 2473-4209. DOI: 10.1002/mp.12679 (cit. on p. 21).

Newhauser, W. D. and R. Zhang (Apr. 21, 2015). "The physics of proton therapy". In: *Physics in Medicine and Biology* 60.8, R155–R209. ISSN: 0031-9155, 1361-6560. DOI: 10.1088/0031-9155/60/8/R155 (cit. on p. 4).

Ng, J., F. Gregucci, R. T. Pennell, et al. (Jan. 27, 2023). "MRI-LINAC: A transformative technology in radiation oncology". In: *Frontiers in Oncology* 13, p. 1117874. ISSN: 2234-943X. DOI: 10.3389/fonc.2023.1117874 (cit. on p. 21).

Ohara, K., T. Okumura, M. Akisada, et al. (Oct. 1, 1989). "Irradiation synchronized with respiration gate". In: *International Journal of Radiation Oncology*Biology*Physics* 17.4, pp. 853–857. ISSN: 0360-3016. DOI: 10.1016/0360-3016(89)90078-3 (cit. on p. 21).

Ondreka, D. and U. Weinrich (2009). "The Heidelberg Ion Therapy (HIT) Accelerator Coming into Operation". In: *AIP Conference Proceedings*. APPLICATION OF ACCELERATORS IN RESEARCH AND INDUSTRY: Twentieth International Conference. Fort Worth (Texas): AIP, pp. 426–428. DOI: 10.1063/1.3120065. URL: https://pubs.aip.org/aip/acp/article/1099/1/426-428/829024 (cit. on pp. 39, 75).

Ondreka, D., L. Bozyk, C. Graeff, P. Spiller, J. Stadlmann, and L. Volz (2024). "Slow extraction of a dual-isotope beam from SIS18". In: *JACoW* IPAC2024, TUPS29. DOI: 10.18429/JACoW-IPAC2024-TUPS29 (cit. on p. 10).

OpenAI (2025). *ChatGPT*. URL: https://openai.com (visited on 05/10/2025) (cit. on p. xi).

Ordoñez, C. E., N. T. Karonis, K. L. Duffin, et al. (June 1, 2019). "Fast in situ image reconstruction for proton radiography". In: *Journal of Radiation Oncology* 8.2, pp. 185–198. ISSN: 1948-7908. DOI: 10.1007/s13566-019-00387-x (cit. on p. 25).

Owen, H., A. Lomax, and S. Jolly (Feb. 2016). "Current and future accelerator technologies for charged particle therapy". In: *Nuclear Instruments and Methods in Physics Research Section A: Accelerators, Spectrometers, Detectors and Associated Equipment* 809, pp. 96–104. ISSN: 01689002. DOI: 10.1016/j.nima.2015.08.038 (cit. on p. 8).

Paganetti, H. (June 2009). "Dose to water versus dose to medium in proton beam therapy". In: *Physics in Medicine & Biology* 54.14, p. 4399. ISSN: 0031-9155. DOI: 10.1088/0031-9155/54/14/004 (cit. on p. 19).

Paganetti, H. (June 7, 2012). "Range uncertainties in proton therapy and the role of Monte Carlo simulations". In: *Physics in Medicine and Biology* 57.11, R99–R117. ISSN: 0031-9155, 1361-6560. DOI: 10.1088/0031-9155/57/11/R99 (cit. on pp. 1, 5, 6, 16, 18).

Paganetti, H., P. Botas, G. C. Sharp, and B. Winey (Nov. 2021). "Adaptive proton therapy". In: *Physics in Medicine & Biology* 66.22, 22TR01. ISSN: 0031-9155. DOI: 10.1088/1361-6560/ac344f (cit. on p. 82).

Parodi, K. (July 1, 2014). "Heavy ion radiography and tomography". In: *Physica Medica*. Particle Radiosurgery Conference 30.5, pp. 539–543. ISSN: 1120-1797. DOI: 10.1016/j.ejmp.2014.02.004 (cit. on p. 11).

Parodi, K., A. Mairani, S. Brons, et al. (May 2012). "Monte Carlo simulations to support start-up and treatment planning of scanned proton and carbon ion therapy at a synchrotron-based facility". In: *Physics in Medicine and Biology* 57.12, pp. 3759–3784. ISSN: 0031-9155. DOI: 10.1088/0031-9155/57/12/3759 (cit. on pp. 15, 16).

Parodi, K. and J. C. Polf (Nov. 2018). "In vivo range verification in particle therapy". In: *Medical Physics* 45.11, e1036–e1050. ISSN: 0094-2405. DOI: 10.1002/mp.12960 (cit. on p. 20).

Parodi, K., A. Mairani, and F. Sommerer (July 2013). "Monte Carlo-based parametrization of the lateral dose spread for clinical treatment planning of scanned proton and carbon ion beams". In: *Journal of Radiation Research* 54 (Suppl 1), pp. i91–i96. ISSN: 0449-3060. DOI: 10.1093/jrr/rrt051 (cit. on pp. 15, 16).

Penfold, S. N. (2011). "Image reconstruction and Monte Carlo simulations in the development of proton computed tomography for applications in proton radiation therapy". thesis. University of Wollongong. URL: https://ro.uow.edu.au/articles/thesis/Image_reconstruction_and_Monte_Carlo_simulations_in_the_development_of_proton_computed_tomography_for_applications_in_proton_radiation_therapy/27660870/1 (cit. on p. 24).

Perl, J., J. Shin, J. Schumann, B. Faddegon, and H. Paganetti (Nov. 2012). "TOPAS: an innovative proton Monte Carlo platform for research and clinical applications". In: *Medical Physics* 39.11, pp. 6818–6837. ISSN: 0094-2405. DOI: 10.1118/1.4758060 (cit. on pp. 16, 35, 36).

Phillips, M. H., E. Pedroni, H. Blattmann, T. Boehringer, A. Coray, and S. Scheib (Jan. 1992). "Effects of respiratory motion on dose uniformity with a charged particle scanning method". In: *Physics in Medicine & Biology* 37.1, p. 223. ISSN: 0031-9155. DOI: 10.1088/0031-9155/37/1/016 (cit. on p. 21).

Phillips, T. L., K. K. Fu, and S. B. Curtis (Jan. 1, 1977). "Tumor biology of helium and heavy ions". In: *International Journal of Radiation Oncology*Biology*Physics*. Particles and Radiation Therapy Second International Conference 3, pp. 109–113. ISSN: 0360-3016. DOI: 10.1016/0360-3016(77)90236-X (cit. on p. 78).

Pleil, J. D., M. A. G. Wallace, M. D. Davis, and C. M. Matty (Sept. 27, 2021). "The physics of human breathing: flow, timing, volume, and pressure parameters for normal, on-demand, and ventilator respiration". In: *Journal of breath research* 15.4, 10.1088/1752–7163/ac2589. ISSN: 1752-7155. DOI: 10.1088/1752-7163/ac2589 (cit. on p. 47).

Poludniowski, G., N. M. Allinson, and P. M. Evans (Sept. 2015). "Proton radiography and tomography with application to proton therapy". In: *The British Journal of Radiology* 88.1053, p. 20150134. ISSN: 0007-1285. DOI: 10.1259/bjr.20150134 (cit. on p. 11).

Pryanichnikov, A., J. J. Hardt, L. Martin, et al. (2025a). "Experimental Single Plane Position Tracking Proton an Helium Pencil Beam Radiographs: Feasibility Study". In: *International Journal of Particle Therapy*. Proceedings to the 63nd Annual Conference of the Particle Therapy Cooperative Group (PTCOG) (cit. on p. 23).

Pryanichnikov, A., J. J. Hardt, L. Martin, et al. (2025b). "Single Plane Positioning Tracking Proton and Helium Pencil Beam Radiographs: Phantom Study". In: 67th Annual Meeting, American Association of Physicists in Medicine (cit. on p. 23).

Pryanichnikov, A., J. J. Hardt, E. A. DeJongh, et al. (May 1, 2025c). "Feasibility study of using fast low-dose pencil beam proton and helium radiographs for intrafractional motion management". In: *Physica Medica* 133, p. 104959. ISSN: 1120-1797. DOI: 10.1016/j.ejmp.2025.104959 (cit. on p. 23).

Pryanichnikov, A. A., J. J. Hardt, L. Martin, et al. (2025d). "Experimental proton and helium pencil beam radiographs with clinical scanner prototype for range-guidance in ion therapy". In: European Society for Radiotherapy and Oncology (cit. on p. 23).

PTCOG (2025a). *PTCOG - Facilities in Operation (public)*. URL: https://ptcog.site/index.php/facilities-in-operation-public (visited on 03/02/2025) (cit. on pp. 9, 82).

PTCOG (2025b). *PTCOG - Patient Statistics (public)*. URL: https://ptcog.site/index.php/patient-statistics-2 (visited on 03/02/2025) (cit. on p. 1).

Rahim, S., J. Korte, N. Hardcastle, S. Hegarty, T. Kron, and S. Everitt (Feb. 25, 2020). "Upright Radiation Therapy. A Historical Reflection and Opportunities for Future Applications". In: *Frontiers in Oncology* 10. ISSN: 2234-943X. DOI: 10.3389/fonc.2020.00213 (cit. on p. 82).

Renner, E., C. Schmitzer, F. Plassard, et al. (2024). "Towards the slow extraction of mixed He and C beams for online range verification". In: *JACoW*, THPR43. DOI: 10.18429/JACoW-IPAC2024-THPR43 (cit. on pp. 9–11).

Schiavi, A., M. Senzacqua, S. Pioli, et al. (Sept. 2017). "Fred: a GPU-accelerated fast-Monte Carlo code for rapid treatment plan recalculation in ion beam therapy". In: *Physics in Medicine & Biology* 62.18, p. 7482. ISSN: 0031-9155. DOI: 10.1088/1361-6560/aa8134 (cit. on p. 35).

Schlegel, W., C. P. Karger, and O. Jäkel, eds. (2018). *Medizinische Physik: Grundlagen – Bildgebung – Therapie – Technik*. Berlin, Heidelberg: Springer. ISBN: 978-3-662-54800-4 978-3-662-54801-1. DOI: 10.1007/978-3-662-54801-1. URL: http://link.springer.com/10.1007/978-3-662-54801-1 (cit. on pp. 3, 5–8, 13–18, IX).

Schneider, U., E. Pedroni, and A. Lomax (Jan. 1996). "The calibration of CT Hounsfield units for radiotherapy treatment planning". In: *Physics in Medicine & Biology* 41.1, p. 111. ISSN: 0031-9155. DOI: 10.1088/0031-9155/41/1/009 (cit. on p. 25).

Schneider, W., T. Bortfeld, and W. Schlegel (Jan. 2000). "Correlation between CT numbers and tissue parameters needed for Monte Carlo simulations of clinical dose distributions". In: *Physics in Medicine and Biology* 45.2, pp. 459–478. ISSN: 0031-9155. DOI: 10.1088/0031-9155/45/2/314 (cit. on pp. 42, II).

Scholz, M., A. M. Kellerer, W. Kraft-Weyrather, and G. Kraft (Mar. 1, 1997). "Computation of cell survival in heavy ion beams for therapy". In: *Radiation and Environmental Biophysics* 36.1, pp. 59–66. ISSN: 1432-2099. DOI: 10.1007/s004110050055 (cit. on p. 29).

Schuemann, J., D. Giantsoudi, C. Grassberger, M. Moteabbed, C. H. Min, and H. Paganetti (Aug. 1, 2015). "Assessing the Clinical Impact of Approximations in Analytical Dose Calculations for Proton Therapy". In: *International Journal of Radiation Oncology*Biology*Physics* 92.5, pp. 1157–1164. ISSN: 0360-3016. DOI: 10.1016/j.ijrobp.2015.04.006 (cit. on p. 80).

Schulte, R. W., S. N. Penfold, J. T. Tafas, and K. E. Schubert (2008). "A maximum likelihood proton path formalism for application in proton computed tomography". In: *Medical Physics* 35.11, pp. 4849–4856. ISSN: 2473-4209. DOI: 10.1118/1.2986139 (cit. on pp. 6, 12, 13).

Seltzer, S., D. Barlett, D. Burns, et al. (2011). "Fundamental qantities and units for ionizing radiation". In: *Journal of the ICRU* 11 (cit. on pp. 3, 4, 7).

Shirey, R. J. and H. T. Wu (Dec. 14, 2017). "Quantifying the effect of air gap, depth, and range shifter thickness on TPS dosimetric accuracy in superficial PBS proton therapy". In: *Journal of Applied Clinical Medical Physics* 19.1, pp. 164–173. ISSN: 1526-9914. DOI: 10.1002/acm2.12241 (cit. on p. 79).

Siddon, R. L. (1985). "Fast calculation of the exact radiological path for a three-dimensional CT array". In: *Medical Physics* 12.2, pp. 252–255. ISSN: 0094-2405. DOI: 10.1118/1.595715 (cit. on pp. 14, 30).

Simard, M., R. Fullarton, L. Volz, et al. (2025). "A comparison of carbon ions versus protons for integrated mode ion imaging". In: *Medical Physics* n/a (n/a). ISSN: 2473-4209. DOI: 10.1002/mp.17645 (cit. on p. 76).

Souris, K., A. Barragan Montero, G. Janssens, D. Di Perri, E. Sterpin, and J. A. Lee (2019). "Technical Note: Monte Carlo methods to comprehensively evaluate the robustness of 4D treatments in proton therapy". In: *Medical Physics* 46.10, pp. 4676–4684. ISSN: 2473-4209. DOI: 10.1002/mp.13749 (cit. on p. 35).

Souris, K., J. A. Lee, and E. Sterpin (2016). "Fast multipurpose Monte Carlo simulation for proton therapy using multi- and many-core CPU architectures". In: *Medical Physics* 43.4, pp. 1700–1712. ISSN: 2473-4209. DOI: 10.1118/1.4943377 (cit. on p. 35).

Steitz, J., P. Naumann, S. Ulrich, et al. (Oct. 7, 2016). "Worst case optimization for interfractional motion mitigation in carbon ion therapy of pancreatic cancer". In: *Radiation Oncology (London, England)* 11, p. 134. ISSN: 1748-717X. DOI: 10.1186/s13014-016-0705-8 (cit. on p. 83).

Taylor, P. A., S. F. Kry, and D. S. Followill (Nov. 1, 2017). "Pencil Beam Algorithms Are Unsuitable for Proton Dose Calculations in Lung". In: *International Journal of Radiation Oncology*Biology*Physics* 99.3, pp. 750–756. ISSN: 0360-3016. DOI: 10.1016/j.ijrobp.2017.06.003 (cit. on p. 80).

Tecker, F. (Aug. 2021). "Injection and Extraction". In: *CAS - CERN Accelerator School 2021: Introduction to Accelerator Physics* (cit. on p. 10).

Teske, H., K. Bartelheimer, J. Meis, R. Bendl, E. M. Stoiber, and K. Giske (May 2017). "Construction of a biomechanical head and neck motion model as a guide to evaluation of deformable image registration". In: *Physics in Medicine & Biology* 62.12, N271. ISSN: 0031-9155. DOI: 10.1088/1361-6560/aa69b6 (cit. on p. 85).

Tessonnier, T., A. Mairani, S. Brons, et al. (Aug. 2017). "Helium ions at the heidelberg ion beam therapy center: comparisons between FLUKA Monte Carlo code predictions and dosimetric measurements". In: *Physics in Medicine & Biology* 62.16, p. 6784. ISSN: 0031-9155. DOI: 10.1088/1361-6560/aa7b12 (cit. on p. 15).

Tessonnier, T., S. Ecker, J. Besuglow, et al. (July 15, 2023). "Commissioning of Helium Ion Therapy and the First Patient Treatment With Active Beam Delivery". In: *International Journal of Radiation Oncology*Biology*Physics* 116.4, pp. 935–948. ISSN: 0360-3016. DOI: 10.1016/j.ijrobp.2023.01.015 (cit. on pp. 9, 15).

Tripathi, R. K., F. A. Cucinotta, and J. W. Wilson (Sept. 1, 1999). "Accurate universal parameterization of absorption cross sections III – light systems". In: *Nuclear Instruments and Methods in Physics Research Section B: Beam Interactions with Materials and Atoms* 155.4, pp. 349–356. ISSN: 0168-583X. DOI: 10.1016/S0168-583X(99)00479-6 (cit. on pp. 36, II).

Ulrich-Pur, F., T. Bergauer, T. Galatyuk, et al. (Mar. 2024). "First experimental time-of-flight-based proton radiography using low gain avalanche diodes". In: *Physics in Medicine & Biology* 69.7, p. 075031. ISSN: 0031-9155. DOI: 10.1088/1361-6560/ad3326 (cit. on p. 77).

Unkelbach, J., M. Alber, M. Bangert, et al. (Nov. 2018). "Robust radiotherapy planning". In: *Physics in Medicine &\mathsemicolon$ Biology* 63.22, 22TR02. ISSN: 0031-9155. DOI: 10.1088/1361-6560/aae659 (cit. on p. 19).

Volz, L., C. Graeff, M. Durante, and C.-A. Collins-Fekete (Jan. 10, 2024). "Focus stacking single-event particle radiography for high spatial resolution images and 3D feature localization". In: *Physics in Medicine and Biology* 69.2, p. 024001. ISSN: 1361-6560. DOI: 10.1088/1361-6560/ad131a (cit. on p. 85).

Volz, L., L. Kelleter, S. Both, et al. (Feb. 2020). "Experimental exploration of a mixed helium/carbon beam for online treatment monitoring in carbon ion beam therapy". In: *Physics in Medicine and Biology* 65.5, p. 055002. ISSN: 0031-9155. DOI: 10.1088/1361-6560/ab6e52 (cit. on pp. 2, 77).

Volz, L., P. Piersimoni, V. A. Bashkirov, et al. (Oct. 2, 2018). "The impact of secondary fragments on the image quality of helium ion imaging". In: *Physics in Medicine and Biology* 63.19, p. 195016. ISSN: 1361-6560. DOI: 10.1088/1361-6560/aadf25 (cit. on p. 76).

Wang, M., L. Zhang, J. Zheng, G. Li, W. Dai, and L. Dong (Jan. 1, 2023). "Investigating the effects of a range shifter on skin dose in proton therapy". In: *Nuclear Engineering and Technology* 55.1, pp. 215–221. ISSN: 1738-5733. DOI: 10.1016/j.net.2022.09.016 (cit. on p. 32).

Wang, Z., A. Bovik, H. Sheikh, and E. Simoncelli (Apr. 2004). "Image quality assessment: from error visibility to structural similarity". In: *IEEE Transactions on Image Processing* 13.4, pp. 600–612. ISSN: 1941-0042. DOI: 10.1109/TIP.2003.819861 (cit. on p. 43).

Weinrich, U. and C. M. Kleffner (2008). "Commissioning of the Carbon Beam Gantry at the Heidelberg Ion Therapy (HIT) Accelerator". In: *EPAC08-TUPP134* (cit. on p. 9).

Wieser, H.-P., E. Cisternas, N. Wahl, et al. (2017). "Development of the open-source dose calculation and optimization toolkit matRad". In: *Medical Physics* 44.6, pp. 2556–2568. ISSN: 2473-4209. DOI: 10.1002/mp.12251 (cit. on pp. 4, 14, 17, 35, IX).

Wilkens, J. J. and U. Oelfke (June 21, 2006). "Fast multifield optimization of the biological effect in ion therapy". In: *Physics in Medicine and Biology* 51.12, pp. 3127–3140. ISSN: 0031-9155, 1361-6560. DOI: 10.1088/0031-9155/51/12/009 (cit. on p. 29).

Xie, Y., E. H. Bentefour, G. Janssens, et al. (Sept. 1, 2017). "Prompt Gamma Imaging for In Vivo Range Verification of Pencil Beam Scanning Proton Therapy". In: *International Journal of Radiation Oncology*Biology*Physics* 99.1, pp. 210–218. ISSN: 0360-3016. DOI: 10.1016/j.ijrobp.2017.04.027 (cit. on p. 20).

Zaider, M. and H. H. Rossi (1980). "The Synergistic Effects of Different Radiations". In: *Radiation Research* 83.3, pp. 732–739. ISSN: 0033-7587. DOI: 10.2307/3575352 (cit. on p. 29).

Publications

This is a list of publications and conference contributions from the years 2022 to 2025, during my doctorate studies.

Journal Articles

Hardt, J. J., A. A. Pryanichnikov, N. Homolka, E. A. DeJongh, D. F. DeJongh, R. Cristoforetti, O. Jäkel, J. Seco, and N. Wahl (2024b). "The potential of mixed carbon-helium beams for online treatment verification: a simulation and treatment planning study". In: *Physics in Medicine and Biology*. issn: 0031-9155. doi: 10.1088/1361-6560/ad46db. url: http://iopscience.iop.org/article/10.1088/1361-6560/ad46db, Presented in this thesis

Pryanichnikov, A., **J. J. Hardt**, E. A. DeJongh, L. Martin, D. F. DeJongh, O. J¨akel, N. Wahl, and J. Seco (May 1, 2025c). "Feasibility study of using fast low-dose pencil beam proton and helium radiographs for intrafractional motion management". In: *Physica Medica* 133, p. 104959. issn: 1120-1797. doi: 10.1016/j.ejmp.2025.104959. url:http://www.sciencedirect.com/science/article/pii/S1120179725000699

Cristoforetti, R., **J. J. Hardt**, and N. Wahl (Jan. 10, 2025a). "Scenario-free robust optimization algorithm for IMRT and IMPT treatment planning". doi: 10.48550/arXiv.2501.05818. url:http://arxiv.org/abs/2501.05818, Accepted for publication in Medical Physics (May 8, 2025), currently in final typesetting with prereprint available on arXiv.

Unpublished Journal Articles

Hardt, J. J., A. A. Pryanichnikov, O. Jäkel, J. Seco, and N. Wahl (May 2, 2025). "Helium Range Viability for Online Range Probing in Mixed Carbon-Helium Beams". doi: 10.48550/arXiv.2505.01165. url: http://arxiv.org/abs/2505.01165, Presented in this thesis, under review in Medical Physics,

Conference Contributions

Hardt, J. J., T. Ortkamp, and N. Wahl (Feb. 14, 2023b). "P 088 - Towards a generalized (N)TCP optimization framework across modalities using classical and machine learning models". In: *International Journal of Particle Therapy*. Proceedings to the 60th Annual Conference of the Particle Therapy Cooperative Group (PTCOG).

doi: 10.14338/IJPT-23-PTCOG60-9.4. url: http://pmc.ncbi.nlm.nih.gov/articles/PMC10166013//, Poster presentation, this poster was awarded with a poster prize.

Hardt, J. J., N. Homolka, and N. Wahl (2023a). "Bewegungsüberwachung mit einem gemischten Kohlenstoff-Helium Strahl – eine erste Simulationsstudie". In: *54. Jahrestagung der Deutschen Gesellschaft für Medizinische Physik*, Oral presentation

Hardt, J. J., A. Pryanichnikov, N. Homolka, E. Dejongh, D. F. Dejongh, R. Cristoforetti, O. Jäkel, J. Seco, and N. Wahl (June 1, 2024a). "P113 /#136 - Development of a Treatment Planning and Simulation Framework for adaptive mixed Carbon-Helium Ion Therapy". In: *International Journal of Particle Therapy*. Proceedings to the 62nd Annual Conference of the Particle Therapy Cooperative Group (PTCOG) 12, p. 100498. doi: 10.1016/j.ijpt.2024.100498. url: http://www.sciencedirect.com/science/article/pii/S233151802400564X, Poster presentation

Hardt, J. J., A. Pryanichnikov, O. Jäkel, J. Seco, and N. Wahl (2025a). "Investigation of the residual helium range and lung patient use cases in online range probing with mixed Carbon-Helium beams". In: *International Journal of Particle Therapy*. Proceedings to the 63nd Annual Conference of the Particle Therapy Cooperative Group (PTCOG), Oral presentation

Cristoforetti, R., P. Süss, **J. J. Hardt**, and N. Wahl (2025b). "Trading Robustness: 4D Proton Planning with Scneario-Free Mulit-Criteria Optimization Approaches". In: *International Journal of Particle Therapy*. Proceedings to the 63nd Annual Conference of the Particle Therapy Cooperative Group (PTCOG), Oral presentation,

Pryanichnikov, A., **J. J. Hardt**, L. Martin, C. Stengl, A. Bakhtiari Moghaddam, E. A.DeJongh, O. Jäkel, N. Wahl, and J. Seco (2025a). "Experimental Single Plane Position Tracking Proton an Helium Pencil Beam Radiographs: Feasibility Study". In: *International Journal of Particle Therapy*. Proceedings to the 63nd Annual Conference of the Particle Therapy Cooperative Group (PTCOG), Oral presentation

Pryanichnikov, A., **J. J. Hardt**, L. Martin, C. Stengl, A. Bakhtiari Moghaddam, E. A.DeJongh, D. F. DeJongh, O. Jäkel, N. Wahl, and J. Seco (2025b). "Single Plane Positioning Tracking Proton and Helium Pencil Beam Radiographs: Phantom Study". In: *67th Annual Meeting, American Association of Physicists in Medicine*, Poster presentation

Pryanichnikov, A. A., **J. J. Hardt**, L. Martin, C. Stengl, E. A. DeJongh, D. F. DeJongh, S.Brons, O. Jäkel, N. Wahl, and J. Seco (2025d). "Experimental proton and

helium pencil beam radiographs with clinical scanner prototype for range-guidance in ion therapy". In: *European Society for Radiotherapy and Oncology*, Poster presentation

Miscellaneous

During my doctoral thesis I contributed to the development of the open-source treatment planning software matRad (`https://github.com/e0404/matRad`[2], Abbani et al. (2024)).

[2] visited on 05/10/25

Acknowledgments

First and foremost, I would like to express my sincere gratitude to my supervisor Dr. Niklas Wahl for giving me the opportunity to conduct this research within his group. His guidance and support have been invaluable throughout this journey. His expertise and insightful feedback have greatly contributed to the development of this work, helping me refine my research approach and broaden my scientific perspective. I would also like to extend my gratitude to the additional members of my Thesis Advisory Committee, Prof. Dr Oliver Jäkel and Prof. Dr. Joao Seco as well as Prof. Dr. Christian Graeff and Dr. Lennart Volz for their vital feedback, direction and advice. I would like to express my thanks to Prof. Dr. Joao Seco and Prof. Dr. Christian Karger for reading and evaluating this thesis as well as being the examiners in the final defense.

A special thanks also goes to Alexander for showing me how to operate the beam during the long and late night shifts, for his insights and for accompanying me on the HELIOS ride.

I would like to thank the Deutsche Forschungsgemeinschaft (DFG) who funded this thesis (Project No. 457509854). Additionally I would like to thank the HGSFP (Heidelberg Graduate School For Physics) for always replying quickly to any questions i had and especially to the Equal Opportunity Funding for their support, which made participation in the PTCOG62 and PTCOG63 conference possible.

I am also grateful for the friendships I built here within the DKFZ. Especially our "NoBoardgame" group, while unfortunately we never played boardgames we always had a fun evening. A special thanks to Tobias for proufreading part of this thesis.

Ich möchte meine tiefsten Dank meinen Freunden und meiner Familie ausprechen. Meine Familie, die immer für mich da ist und mich bedingungslos in allem unterstützt, was ich tue. Meinen Freunden danke ich auch dafür, dass ihr immer für mich da wart, für eure Gastfreundschaft, für unsere langen Dungeons-and-Dragons-Abende und natürlich für rotation→translation→boooooooost.